Quantitative Analysis of Alpine Skis Using Distributed Sensing and Modal Analysis

by

Joshua L. Priest

B.S., University of Colorado at Boulder, 2023

A thesis submitted to the

Faculty of the Graduate School of the

University of Colorado in partial fulfillment

of the requirements for the degree of

Masters of Science

Department of Mechanical Engineering

2025

Committee Members:

Dr. J. Sean Humbert, Chair

Dr. Leopold Beuken

Dr. Robert MacCurdy

Priest, Joshua L. (M.S., Mechanical Engineering)

Quantitative Analysis of Alpine Skis Using Distributed Sensing and Modal Analysis

Thesis directed by Prof. Dr. J. Sean Humbert

In the alpine skiing industry, product development and product evaluation are typically conducted using qualitative evaluation; this leads to a relatively inefficient, time-consuming, and imprecise design and testing cycle. A multitude of studies have collected quantitatively relevant data for alpine skis, but most captured singular components in isolation, and there have not been many attempts to marry them all together into a comprehensive qualitative analysis framework.

The grail for qualitative analysis in alpine skiing is the formation of relevant in-situ loading scenarios. Many attempts to create an accurate finite element model (FEM) have been made; most have proven their validity in laboratory settings, but none have proven their validity across a wide range of in-field skiing scenarios due to the lack of available in-situ loading scenarios. The main issue limiting in-situ force estimation is the extreme difficulty of accurately depicting boundary conditions for all phenomena experienced in skiing, making it an ill-posed problem.

This study proposes the use of laboratory modal analysis, in-field modal analysis, and stiffness profile measurements to capture natural frequencies, damping ratios, mode shapes, energy storage and release behaviors, and stiffness distribution profiles to create a complete mechanical and dynamic property profile of an alpine ski for use in quantitative analysis without the need for in-situ loading scenarios. This study will also present an attempt at in-situ displacement and force estimation using a low-cost, portable/lightweight, noninvasive, and robust IMU-based sensing system but has come to the conclusion that IMUs in isolation are not capable of estimating in-situ force accurately. Force estimation validation testing has uncovered the need for more focused testing to accurately depict the relationship between the displacement and acceleration an alpine ski experiences when forces of varying loading rates and durations are applied. This testing can further refine the assumptions made for future in-situ force estimation frameworks.

Dedication

This thesis is dedicated to all of the members of my family that have made this a reality, my parents Tom and Frances Priest, my Grandmothers Kathy and Pat, and my late Grandfather Don. All of whom have contributed to the growth of me as a human and have made me who I am today. I thank each and every one of you for pushing me to be the best version of myself and am looking forward to taking advantage future endeavors with the skills and character each of you has imparted upon me.

Acknowledgements

I would like to express my gratitude toward my colleagues for making this thesis a reality. First I would like to thank Dr. Leo Beuken for building the backbone of this entire project, providing insightful feedback, and joining my gradate committee to see it through. I would like to thank Alec, Quinn, Grace, and Ian for lending me an ear when I needed to vent about this whole process and for providing feedback when asked. I would also like to thank the remainder of the Bio-Inspired Robotics and Perception laboratory for the feedback and support provided along the process of this thesis project. I would like to thank Blister Review for the support they have provided in equipment, test days, feedback, and a platform to share my findings along the way. I would like to thank Dr. Jeni Blacklock for giving me the opportunity to even pursue a Masters in the first place, as well as the rest of the team at Western Colorado University.

I would like to thank my family once again for providing me with the support and guidance to even get to the point of beginning my graduate journey.

Finally, I would like to thank my graduate committee for taking the time to facilitate this research and to further my pursuit of knowledge in the mechanical engineering field. I would like to thank my committee chair and advisor Sean Humbert for providing me this opportunity and all of the awesome experiences I've had along the way. I could not have asked for a better advisor to guide me along the path of higher education, thank you.

Contents

Chapter

1 Introduction **1**

1.1 Motivation 1

1.2 Existing Work 5

2 Methodology **9**

2.1 Laboratory Modal Analysis 10

2.1.1 Roving Hammer vs Roving Accelerometer Impact Testing 12

2.1.2 Accelerometer vs. MOCAP 14

2.1.3 Frequency Response Function 18

2.2 In-Field Modal Analysis 25

2.2.1 Filtering Techniques 26

2.2.2 Fast Fourier Transforms and Power Spectral Density Analysis 26

2.2.3 In-Field vs. Laboratory 27

2.3 Stiffness, Displacement, and Force Estimation 27

2.3.1 Bending and Torsional Stiffness Measurements 28

2.3.2 Filtering and Limiting Factors 31

2.3.3 Displacement Estimation 32

2.3.4 Force Estimation 34

3 Results **42**

3.1 Laboratory Modal Analysis . . . 42

3.1.1 Accelerometer vs. MOCAP . . . 42

3.1.2 Modal Characteristics of Skis . . . 46

3.2 In-Field Modal Analysis . . . 55

3.2.1 In-Field vs. Laboratory . . . 55

3.2.2 Modal Coupling . . . 61

3.3 Stiffness, Displacement, and Force Estimation . . . 63

3.3.1 Bending and Torsional Stiffness Measurements . . . 63

3.3.2 Displacement Estimation . . . 64

3.3.3 Force Estimation . . . 70

4 Discussion **74**

4.1 Modal Analysis . . . 74

4.1.1 MOCAP Advantages and Disadvantages . . . 74

4.1.2 Modal Characteristics and Mechanical Characteristics . . . 76

4.2 Displacement and Force Estimation . . . 77

4.2.1 Displacement Estimation Shortcomings . . . 78

4.2.2 Force Estimation Complications . . . 79

5 Conclusion **81**

5.1 Future Work . . . 81

5.1.1 Improvements to Laboratory Modal Testing . . . 81

5.1.2 Expanded In-field Modal Testing . . . 82

5.1.3 Correlation Between Qualitative and Quantitative . . . 82

5.1.4 Changes to Displacement and Force Estimation . . . 83

5.2 Concluding Thoughts . . . 83

Bibliography **85**

Appendix

A Additional Figures and Equations **89**

Tables

Table

3.1 Accel. vs. MOCAP Bonafide 46

3.2 Accel. vs. MOCAP Rustler 46

3.3 Bonafide vs. Rustler Natural Frequencies in Bending 54

3.4 Bonafide vs. Rustler Damping Ratios in Bending 54

3.5 Bonafide vs. Rustler Natural Frequencies in Torsion 54

3.6 Bonafide vs. Rustler Damping Ratios in Torsion 55

Figures

Figure

1.1 Campaniform Sensilla Diagram 2

1.2 DPS Testing 3

1.3 X-56A Sensor Layout 4

2.1 Bending vs. Torsion 12

2.2 Roving Hammer/Input 13

2.3 Roving Accelerometer/Output 14

2.4 Suspended Roving Output Impact Test Accel. 15

2.5 Ski Accelerometer Positions 15

2.6 Ski Roving Output Impact Test MOCAP 16

2.7 Marker Pattern 17

2.8 MOCAP Interpolation 18

2.9 Impact Test Data 19

2.10 Example Stability Diagram 22

2.11 FRF and OFRF Magnitude vs. Real vs. Imaginary 23

2.12 Dylan on The Bonafide 25

2.13 Flexrig at Western Colorado University 29

2.14 Low Pass Filter 32

3.1 Accelerometer Stability Analysis 44

3.2 MOCAP Stability Analysis . . . 45
3.3 FRF Magnitude vs. Real Acceleration . . . 47
3.4 FRF Magnitude vs. Real Displacement . . . 48
3.5 Accelerometer FRF Imaginary Component . . . 49
3.6 MOCAP FRF Imaginary Component . . . 50
3.7 Unity Bending Mode Shapes . . . 51
3.8 Bending Mode Shapes in Acceleration . . . 52
3.9 Bending Mode Shapes in Displacement . . . 53
3.10 FFT for Bonafide in Bending and Torsion . . . 57
3.11 FFT for Rustler in Bending and Torsion . . . 58
3.12 PSD for Bonafide in Bending and Torsion . . . 59
3.13 PSD for Rustler in Bending and Torsion . . . 60
3.14 Modal Coupling . . . 61
3.15 Bonafide FRF Magnitude for Coupling . . . 62
3.16 Rustler FRF Magnitude for Coupling . . . 62
3.17 Bending and Torsional Stiffness Profiles . . . 64
3.18 In-Field Displacement Estimates . . . 66
3.19 Ground-Truth vs. Estimated Displacement . . . 68
3.20 Estimated Displacement With RMSE Bounds . . . 69
3.21 Frequency Domain Second-Order Force Estimates . . . 71
3.22 Second-Order Force Estimates . . . 72
3.23 Laboratory Direct Sensor Mapping Force Estimates . . . 73

A.1 Slope Fit . . . 90
A.2 Magnitude of OFRF . . . 91
A.3 Real Component of OFRF . . . 92
A.4 Imaginary Component of OFRF . . . 93

A.5 Accelerometer Stability Analysis Larger 94
A.6 MOCAP Stability Analysis Larger 95
A.7 MOCAP Torsional Stability Analysis 96
A.8 Magnitude of Acceleration-Based FRF for the Bonafide Larger 97
A.9 Magnitude of Acceleration-Based FRF for the Rustler Larger 98
A.10 Real Component of Acceleration-Based FRF for the Bonafide Larger 99
A.11 Real Component of Acceleration-Based FRF for the Rustler Larger 100
A.12 Imaginary Component of Acceleration-Based FRF for the Bonafide Larger 101
A.13 Imaginary Component of Acceleration-Based FRF for the Rustler Larger 102
A.14 Real Component of Displacement-Based FRF for the Bonafide Larger 103
A.15 Real Component of Displacement-Based FRF for the Rustler Larger 104
A.16 Imaginary Component of Displacement-Based FRF for the Bonafide Larger 105
A.17 Imaginary Component of Displacement-Based FRF for the Rustler Larger 106
A.18 Unity Bending Mode Shapes Larger 107
A.19 Bending Mode Shapes in Acceleration Larger 108
A.20 Bending Mode Shapes in Displacement Larger 109
A.21 Bending Stiffness Profile Larger 110
A.22 Torsional Stiffness Profile Larger 111

Chapter 1

Introduction

1.1 Motivation

In the world of outdoor recreation gear, both manufacturers and review companies primarily rely on qualitative evaluation to test products; wether that be for product development, performance characterization, or consumer-focused recommendations. Many companies have started to show interest in the use of engineering tools to supplement qualitative evaluations with quantitative analysis. Industries outside of outdoor recreation have leveraged sensor fusion, data analysis,and simulation-based evaluation to improve safety and performance while reducing costs. Alpine skiing is one of the largest sectors of outdoor recreation, producing significant financial value for both resorts and gear manufacturers (4.6 billion USD per year [23]) while also requiring safe and high performance gear. Many alpine ski gear manufacturers have significant R&D costs due to inefficient design cycles and the inconsistent nature of qualitative analysis, as tangible and desired performance improvements require extensive prototyping and iterative testing [11, 47, 6, 14]. This is not due to lack of interest in data-driven simulation-based testing, but rather a byproduct of the lack of relevant, accurate, and accessible data; as it stands, ski companies primarily use Finite Element Analysis (FEA) for safety and failure analysis but they lack the information to leverage FEA for performance evaluation and improvement.

Alpine skiing and more so the interaction between the skier, ski, and snow is a highly dynamic and complex system; the snow is a material that has characteristics fluctuating between a liquid and a solid, skis themselves are a structure consisting of laminated layers (primarily wood, poly-

mers, carbon fiber, and various metals [6]) resulting in quasi-linear characteristics, and the skier varies their inputs wildly depending on conditions, experience, and gear. All of these factors result in a system that is difficult to instrument (high temperature ranges, water incursion possibilities, high impact forces, and small areas for sensor fusion), consistently collect data when instrumented, and characterize. Similarly difficult systems have utilized distributed sensing systems to increase the amount of relevant data available, reduce noise produced from highly dynamic phenomena via spatial averaging, and provide the ability to characterize the entire system. The idea of distributed sensing is taken from biology, as many beings in nature use a form of distributed sensing to perform complex tasks; a great example is the common fly and many other insects have distributed campaniform sensilla [1] (i.e. strain sensors) in their wings to collect strain information to react to perturbations in their environment while flying.

Figure 1.1: Visual of the distribution of campaniform sensilla in the wing of an insect, visual inspired by information provided in [1].

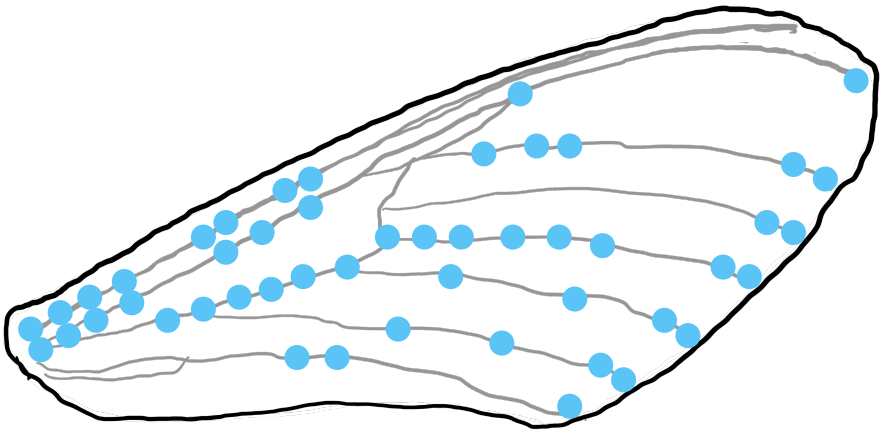

Taking inspiration from biology, Dr. Leopold Beuken [5] developed a sensor system using spatially distributed suite of inertial measurement units (IMU's) to instrument an alpine ski for in-situ data collection. This system consisted of ten distributed IMU's along the center line or

chord of the ski; each IMU records linear acceleration and rotational velocity at a 710 Hz capture rate. This provides a dense and comprehensive dataset that can be used in multiple contexts, including performance characterization, skier evaluation, modal analysis, and possible uses in force estimation. It has been tested both in-field and in-lab to prove the validity of measurements and pose estimations [5]. Preliminary testing was focused on making sure the data pulled from the sensor array was realistic and usable; efforts were made to fine-tune post processing techniques and a special type of filter called an Indirect Complementary Kalman filter was selected to provide accurate pose estimates.

Figure 1.2: Picture of the sensor system [5] in use with DPS Skis for a product development study I conducted with them [32]. Data and conclusions from this study will not be included due to contract based agreements, but images of the system in use will be shown.

In this study, it will discuss modal analysis of the in-situ data for possible use in performance characterization and cross-validation of laboratory modal analysis, using both Fast Fourier Transforms (FFT) and Power Spectrum Decomposition (PSD). Laboratory modal analysis for possible use in performance characterization, correlation with stiffness profiles, correlation with in-field data, and use in frequency domain-based force estimation techniques; where industry standard testing,

such as the roving hammer and roving output were performed; each test was conducted using both a displacement- and acceleration-based response. An attempt at in-situ force estimation using second-order system approximations and frequency domain-based models using the assumed modes method, primarily focused on the component of force that causes the ski to deform. All tests were carried out on two skis, the 2018/2019 Blizzard Bonafide (180cm) and the 2023/2024 Blizzard Rustler 11 (180cm).

In recent years, the use of highly flexible aircraft wings has become more popular due to the increase in overall aerodynamic efficiency [20], but they pose a large issue in that it is extremely difficult to acquire accurate estimates for the force applied to these wings in flight [20]. The use of distributed sensing and frequency domain-based analysis have allowed for accurate force estimation. Many of these techniques have used various sensor types and locations for in-situ measurements; including accelerometers, gyroscopes, strain gauges, Global Positioning Systems (GPS), and flight data (pitot tubes, altimeters, barometers, etc.); they are generally combined in a complex least squares and Kalman filtering algorithm to produce force estimates [20, 17, 19, 18].

Figure 1.3: The X-56A proposed sensor configuration used in one of the force estimation tests conducted at NASA [20]

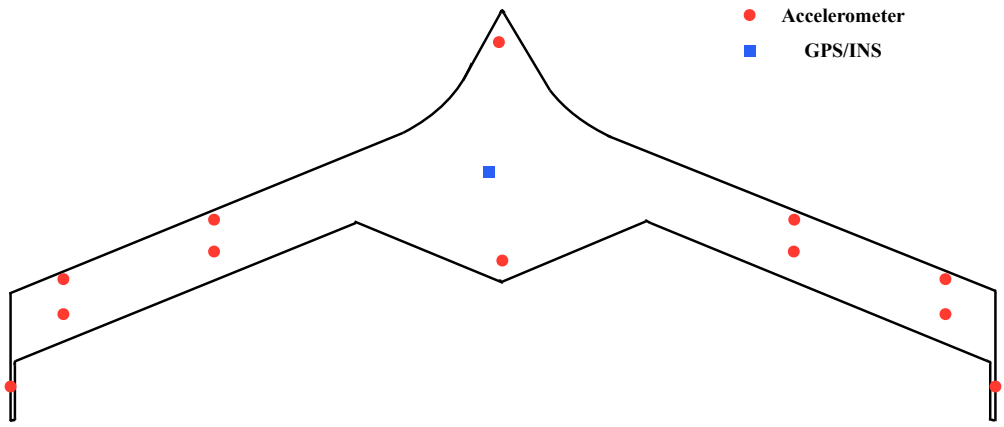

In this study I only have access to accelerometers and gyroscopes [5] for in-situ measure-

ments, making use of similar techniques found in [20, 17, 19, 18] and developing modifications to those techniques, I attempt to estimate the forces a ski experiences in-situ with a low cost, portable/lightweight, noninvasive, and robust sensing system. Laboratory and in-field modal analysis and the measurement of stiffness profiles for both skis featured in this study; provide additional data points to create a mechanical and dynamic property profile for use in the qualitative analysis of alpine ski, while also providing a basis to develop and use techniques in force estimation.

1.2 Existing Work

Staring with modal or frequency analysis of alpine skis, [3] conducted a study primarily to find resonant frequencies and damping using multiple fixturing techniques. This study compared four different fixture setups measuring displacement of the ski via a ruler and strobe light while subjecting the ski to a sweep of frequencies ranging from 10-18Hz. They primarily focused on finding the natural frequency and damping of the first three natural modes; it was determined that both the natural frequencies and damping ratios varied substantially depending on the fixturing setup. [33] conducted a modal analysis for the first four natural modes only utilizing FFT analysis, the studies primary purpose was for pair matching and not performance characterization. [35] is a continuation of the study [33] providing a more detailed background to the process for modal matching mentioned in both studies. [14] conducted both in-field and in-lab tests focused on finding what modes of vibration affected the skier's experience most; they instrumented skis with strain gauges in-field and compared various ski constructions and snow conditions via frequency analysis. Predominant frequencies found in [14] agree with all studies mentioned in this section as well as findings in this thesis. They conducted laboratory test using a matrix of accelerometers to measure the frequency response of the tip of various skis, they fixtured the ski rigidly using a boot jig and applied a consistent static preload to simulate the weight of a skier. After conducting FRF analysis, they mostly compared the torsional and bending characteristics of various skis to pinpoint what modes and frequencies correlated with in-field tests and expert reports; they concluded that a highly active torsional mode related to ski performance more than any other, and the more prominent that

mode is, the more it adversely affects ski performance. [16] expands on both [3, 14] specifically on a ski's response to skidding and the correlation between in-field and in-lab frequency analysis tests. They used IMUs for data capture similar to this thesis and the major finding was that the first three bending and torsion modes are highly coupled, which could explain deviations found between in-field and in-lab testing presented in this thesis. [36] conducted a study on the transmission of vibrations from the ski to the skier using accelerometers on the boot, body and head of the skier; it was determined that transmitted frequencies topped out at 25Hz primarily found in the skiers knees. Differences between prior work and this thesis primarily consist of variations in the torsional resonances found, fixturing of in-lab testing, sensing systems for in-field and in-lab testing, overall focus of the study, and variations in analysis techniques.

Other studies have tried to use different sensor types to estimate the deflection and the load a ski experiences in-situ. [34] uses pressure sensors to measure the pressure distribution along the length of the ski while making a carving turn; they collected and compared data using the same skier in the most consistent conditions possible. [34] found a convenient assumption parameter via cross-corelation of pressure signals, allowing them to treat snow as a "featureless homogeneous medium", but they had experienced a high amount of noise and were limited to a 30Hz sample rate, limiting the amount of data available per turn. [48] continued and improved the work of [34], where they used a combination of pressure sensors, strain gauges, and load cells to measure deflection, pressure, and force simultaneously to allow correlations between measurements to be made. They compared two different skis in both firm and soft snow conditions to acquire a more diverse dataset and to allow comparative conclusions. They were able to prove that the stiffness profiles of skis affect the pressure distribution and displacement a ski experiences in a multitude of snow conditions. [43] had developed a prototype PyzoFlex® based ski instrumentation system, they proved the validity of this curvature-based sensing system and is capable of accurately measuring deflections in-situ; it does require a bulky DAQ and, as this thesis will mention later, deflection did not show to have a linear relationship to force in the displacement/force estimation validation tests conducted for this thesis; making deflection estimates limited in current FEA applications and or for qualitative

evaluations when used in isolation. [28] used a strain-based sensor system not to analyze skis but to see if they could classify snow conditions based on in-situ data; as mentioned in other studies, there is a tangible difference in measured frequency content depending on snow conditions making condition classification possible. [28] does not relate to the focus of this thesis, but it did use a distributed sensing system to success similar to the studies mentioned prior and in this thesis.

Other studies focused on the mechanics and interaction between ski and snow, [29] compared elastic and hypoplastic force penetration models of ski snow interaction and found both to have merits, but deemed the hypoplastic method to be superior for future ski-snow modeling efforts. This was due to the fact that snow does not react in an entirely elastic manner and the hypoplastic model would account for deformation caused by the shovel of the ski, which is a key characteristic to account for when modeling a carved turn. [22] was a precursor to [29], as they tried to calculate the pressure a ski experiences during a carved turn using the hypoplastic interaction assumption. [37] took a more experimental-based approach by measuring the response of various snow samples to repeated applied forces with the goal of determining the deformation characteristics of snow, specifically to better understand the interaction between ski and snow. [37] found that snow has four different types of deformation; brittle failure that occurs on first contact but does not affect future applications of force, plastic flow or micro cracking in localized sections of ice near the surface, extremely small elastic deformation at the base, and delayed elastic deformation in the center of the snow pack. This study supports the conclusions from [29] that a model that includes both elastic and plastic deformation behavior is the ideal method for ski-snow interaction modeling. This thesis will not include any ski-snow interaction as the focus is to provide a framework for quantitative evaluation of alpine skis; the inclusion of snow conditions and the ski-snow interaction could be included in future work to improve the force estimation techniques presented in this thesis.

Efforts have been made to create accurate representations of alpine skis for FEM/FEA-based analysis, [47, 6] were able to create an accurate model of two different alpine skis that aligned with laboratory-based testing results. The laboratory tests only used continuous low loading rate (quasi-static) force applications, and they did not have access to in-situ based simulations, limiting

the ability to correlate FEM results to in-situ ski performance. [11, 12] conducted an extensive study on modeling a ski in a carving turn, combining ski-snow interaction, in-field measurements, and FEA-based simulations. This study was able to create an accurate model of a ski during a carving turn with one major assumption and limited application; the model was designed with the absence of vibrations and the model does not include the response during phenomena outside of a carving turn (ex. a skidding turn).

[10] relates to the focus of this thesis closest of all the previous work presented. They conducted a study of how mechanical properties, specifically bending and torsional stiffness of skis, relate to skier experiences and overall on-snow performance. [10] tested five different skis with five different experienced ski testers on consistent snow conditions. They were able to determine a correlation between mechanical properties and on-snow performance, but more concrete conclusions would require more testing of skis, conditions, and skiers. Upon review of their results and other studies mentioned previously, I've determined that bending and torsional stiffness are not the only significant mechanical properties that effect on-snow performance. This thesis will present a more comprehensive framework for capturing most of the necessary mechanical characteristics of a ski, allowing future work to begin making correlation between what particular mechanical and dynamic properties result in specific performance characteristics on-snow.

Chapter 2

Methodology

All of the studies mentioned in 1 proved the validity of various ski-focused quantitative analysis techniques, but most of them mentioned a "missing puzzle piece"; the goal of this study is to marry and improve many of the techniques mentioned in previous studies, in order to provide a more comprehensive qualitative analysis framework for alpine skis. Most studies found merit in collecting data on mechanical and dynamic properties, whether that be stiffness profiles [10, 34, 48] or modal characteristics [3, 33, 35, 14, 16] to relate to in-field measurements [12, 37], influence simulations [12, 29], or relate to qualitative analysis. Upon review, I have determined that combining stiffness profiles, modal characteristics, and (after future improvements are made) in-field force estimations can provide a cumulative dataset that can allow engineers, reviewers, and consumers to better understand what mechanical traits result in certain on-snow performance characteristics. This study will not try to correlate which specific mechanical traits relate to what performance characteristics due to time constraints and limited skis, skiers, and conditions; instead, it will introduce a theoretical framework that future work can leverage for a more efficient process in relating mechanical traits with performance characteristics or capturing relevant on-snow loading scenarios for FEA analysis. This section will provide the justification and theory behind each qualitative analysis techniques performed in this study.

2.1 Laboratory Modal Analysis

The first step of quantitative analysis begins with a laboratory test that is easily repeatable and controlled that allows for an easy relationship between measured characteristics and simulated characteristics, that being modal analysis, where we can find natural frequencies, damping, energy absorption/release behavior, and mode shapes [38, 24, 2, 20, 17, 19, 18]. Due to the inability to acquire accurate or create our own (only have access to one pair of each ski so dissection was not an option) computer aided design (CAD) models for the two test skis, I chose an experimental method for deriving modal characteristics. Industry has used modal testing for model verification, failure analysis, and identification of structural behavior to prevent resonance-based failure [38, 24, 2, 7]. The test types typically include shaker tests and impact tests [38, 24, 7]. Shaker tests involve electrohydraulic or electromagnetic shakers attached to a structure that can vibrate at specific frequencies. This test is typically used on large structures where the added mass/fixture point from the shaker has a minimal impact on the measured dynamics of the system; in the case of skis, it could massively impact the measured vibrational characteristics of the ski and would no longer classify as a free-free beam condition, as the ski would now have a fixed point, preventing motion in multiple directions. The impact test involves an impact hammer with a load cell at the tip to measure the input force and accelerometers to measure the response/output. I decided that impact tests were the best method for capturing modal characteristics from a ski, as it allows for a free-free beam condition (ski is allowed to move in all directions) and the minimal added mass affecting captured data. The impact test has limitations, it is less accurate than a shaker test and is difficult to collect consistent data [24] due to the way the test is conducted. A free-free beam condition was chosen due to the desire to mitigate the influence of the fixturing system on results, as mentioned in [3], as well as the inability to accurately simulate a real-world load situation as [14] tried to replicate but was unable to replicate the affects of snow contact on a ski. On top of the inability to replicate snow contact, snow properties change with conditions, different skiers have different size and material boots, and the way a skier shifts their weight varies from skier to skier;

so trying to replicate a real-world fixturing scenario was deemed unnecessary for the purposes of this study. Each ski was tested with the bindings on, as that is one variable that would remain constant throughout all field tests, and, as I will mention in 3, the binding affects the mechanical and dynamic properties of the ski [14, 10, 12].

Using the impact test, you can map an input signal or force to a response or output signal, essentially creating a frequency domain-based transfer function for a desired system [38], this is known as a frequency response function (FRF). An FRF can provide information on modal characteristics ranging from natural frequencies, damping ratios, energy storage/release, to mode shapes, all of which can be used to identify the mechanical behavior of a system. Generally speaking, most systems have bending and torsional modes as seen in Figure 2.1, and in an ideal scenario these modes types are independent, a phenomenon know as low coupling. Skis are not what I would consider an ideal system due to the byproducts of the particular materials skis are made of; most have a continuous wood core that is anisotropic (mechanical properties vary based on direction), quasi-linear (there is a possibility that stiffness and damping can vary depending on loading rates or severity of load), and a heterogeneous material (the same piece of wood can have variations in the structure, chemical makeup, moisture content, etc.); carbon is more consistent but can also have anisotropic and quasi-linear material properties; this is dependent on the weave, bonding agents, and general layup; skis can contain other materials like metals and polymers only adding to the complexity of the laminate structure [12, 47, 4].

Figure 2.1: Graphic depicting the difference between isolated bending and torsional modes.

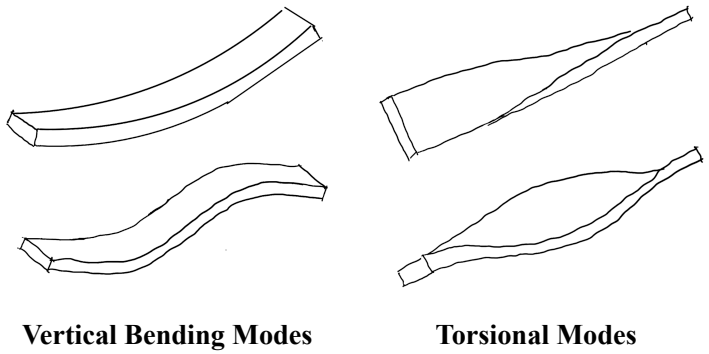

This section will introduce the theory behind the impact test, FRFs, and mode-shape derivation. The same general theoretical framework can be used to find both the bending and torsional characteristics; only varying in output sensor location and the data imputed into FRF analysis [38].

2.1.1 Roving Hammer vs Roving Accelerometer Impact Testing

There are two versions of the industry standard impact test, the roving input/hammer and the roving output/accelerometer [38, 24, 7]. A roving input/hammer test requires only one sensor location, but requires impacts on the structure at multiple nodes; see Figure 2.2 for a representation of a roving input test. A roving output/accelerometer requires an accelerometer at all measurement nodes and only one impact location; see Figure 2.3 for a representation of a roving output test. The main advantages of the roving input test is the requirement for only one output sensor and that you only need to move the hammer impact location in most cases. The roving input test requires more time to conduct, and it struggles to capture the modal characteristics of complex structures [38, 24, 7]. A roving output test requires more output sensors, but it takes less time to conduct and does a better job of capturing the modal characteristics of complex structures [38, 24, 7]. Both tests were carried out in the testing phase of this study, but ultimately the roving output/accelerometer test was chosen as the preferred method. After preliminary results of the

roving input test, I came to the conclusion that the complex structure of the ski and the fixturing method caused the results of the roving input test to be inconsistent and not worth the extra time to conduct. The roving output test ensured that all excitation signals could occur at an antinode, improving the quality of data for for use in FRF analysis [38, 24, 7], as well as collecting data that provides a more comprehensive understanding of the ski's response to excitation. All impact tests were conducted using the NI LabVIEW Sound and Vibration Toolkit [30], the hammer used was the PCB Piezotronics 086C02 modal impact hammer, the output sensors were either accelerometers (the PCB Piezotronics 356A02 triaxial accelerometers) or motion capture markers (Optitrack Prime x 13 and Motive motion capture system (MOCAP).

Figure 2.2: Visual depicting a generalized example of a roving hammer/input test.

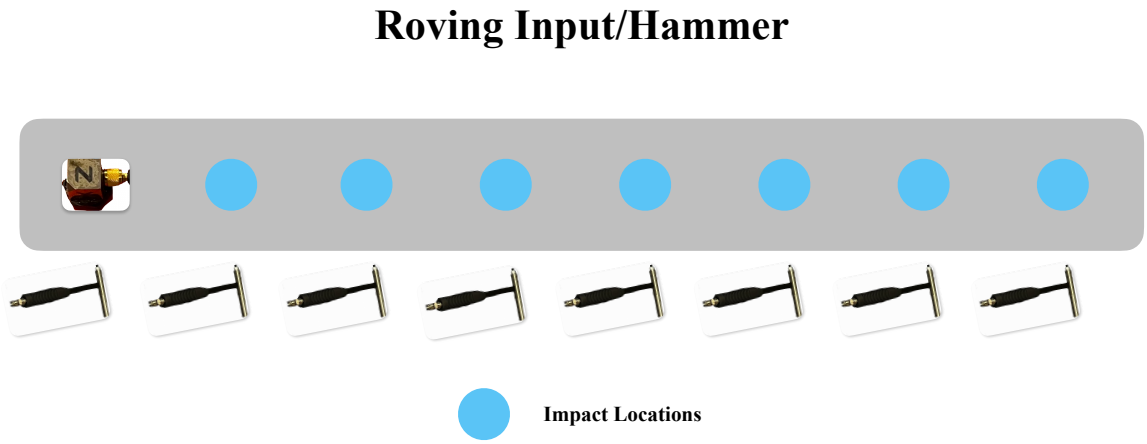

Figure 2.3: Visual depicting a generalized example of a roving accelerometer/output test.

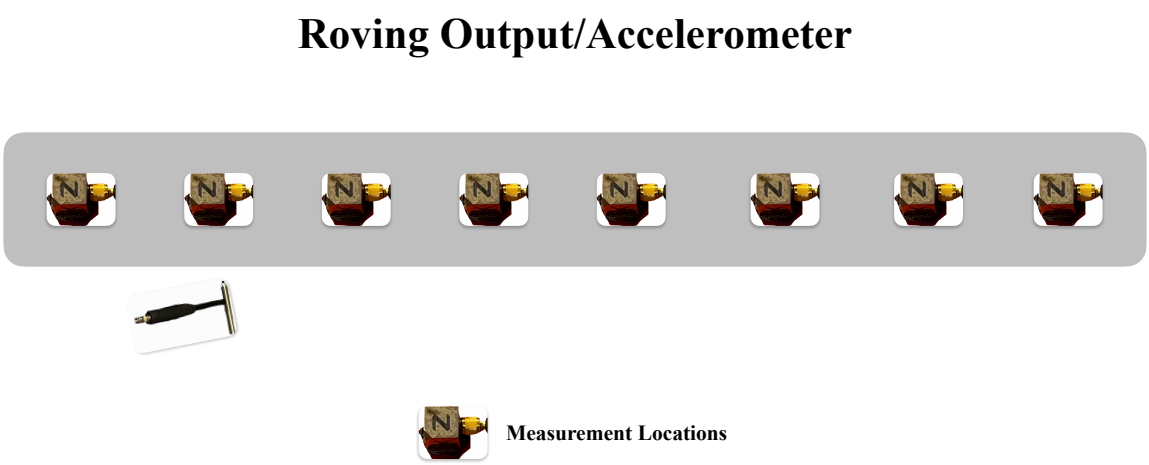

2.1.2 Accelerometer vs. MOCAP

I only had access to two accelerometers, which required the movement of the output sensors to capture a full roving output dataset. See Figures 2.4,2.5 for all the accelerometer positions. The final test procedure required five impacts at an antinode, then shifting the output sensors to new positions and repeating until all ten output measurement nodes (the same ten locations of the IMUs on the in-field test ski as shown in [5]) were captured. The antinodes were determined by capturing a complete roving output dataset for multiple excitation nodes and checking for high coherence (checked during tests in the LabVIEW VI [30]), and consistent FRF results (checked in post-processing with MATLAB [40]) across all output nodes [38, 24, 7]. The same test procedure was used on both test skis, Bonafide and Rustler. All accelerometer-based tests were captured at a sample rate of 1000 Hz.

Figure 2.4: Roving output using accelerometers set up, showing the free-free suspension, the impact hammer, and accelerometers.

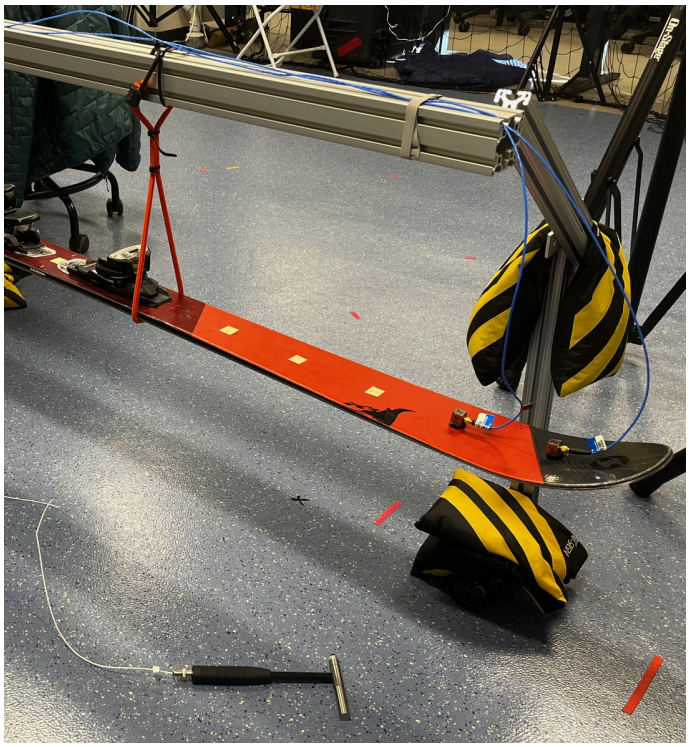

Figure 2.5: Shows the pattern of accelerometers used for one instance of impact testing, also shows the in-field test ski set-up

Due to the limited number of available accelerometers, only bending mode analysis was carried out using accelerometer-based data. In an effort to reduce test time and increase the number of output measurement locations, MOCAP was used to collect both vertical bending and torsional data. The MOCAP system has the ability to capture data at 240 Hz in large capture area, making it a theoretically ideal system for low-frequency focused displacement-based modal analysis

data capture. Modal analysis using MOCAP has not been done to my knowledge, validation via comparison to the industry standard accelerometer-based impact test was carried out to ensure accuracy of the MOCAP system. MOCAP has been used to prove the validity of the in-field measurement system [5] and many other systems that require 3D position measurements [45], as with proper calibration one can achieve a mean ray error close to 0.1-0.2 mm.

MOCAP tests followed a similar procedure to the acceleration-based test, only varying in the fact that I no longer needed to move the output sensors (marker) to capture enough of the ski to find relevant modal characteristics. An example of the marker pattern used and the entire MOCAP setup can be seen in Figures 2.7 and 2.6 respectively. Due to time constraints I could not capture as many points along the chord of the ski as the acceleration-based testing, so any remaining points in vertical bending mode shape formation used the MOCAP measured points in combination with scaled and phase-corrected values from acceleration-based testing. Time synchronization was achieved by instrumenting the impact hammer with its own marker and finding the point/frame of highest position prior to impact and visual confirmation in Motive/Optitrack software.

Figure 2.6: Shows overall set up for MOCAP-based roving output impact test; MOCAP, markers, and the same impact hammer from the accelerometer-based tests.

Figure 2.7: Example of one instance of MOCAP marker pattern for roving output impact test.

To account for the variation in sample rates between the hammer and MOCAP interpolation on the MOCAP data was performed, all interpolation was performed after filtering the hammer data at a cut-off on 240 Hz. Interpolated data was compared to the raw data to ensure the data was unaffected as seen in Figure 2.8. To mitigate the impact of swaying from the free-free beam condition all position data was converted into a relative displacement by subtracting the initial position prior to impact from all positions. As well as calculating the change in vertical position due to sway. This was achieved by finding the horizontal displacement of the central marker and calculating the relative change in vertical position, caused by sway, via Pythagorean theorem, since the distance from the pivot point was known and vibration on the horizontal axis is negligible due to the geometry of the ski. This process removed all frequency content below 1 Hz, essentially acting as a high-pass filter. It removed the negative impact of the free-free beam condition, which allowed the ski to swing around post-impact, introducing a large amount of sub-1 Hz frequency content, negatively affecting the FRF analysis. This process was not applied to accelerometer-based testing as the affect of sway was deemed negligible, as it was found to be negligible after filtering for the displacement-based test.

Figure 2.8: Plot of interpolated and sway compensated MOCAP data in dashed red and raw MOCAP displacement data in solid blue. This shows one impact at one marker position. Position (m) vs. Time (s)

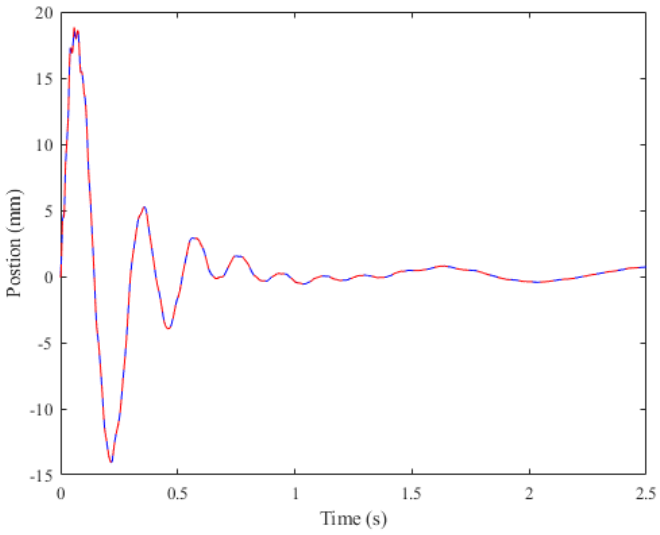

2.1.3 Frequency Response Function

A frequency response function (FRF) is essentially a transfer function mapping an input to an output, specifically in the frequency domain. To find an FRF for a system, divide the power spectral density (PSD) of the output by the PSD of the input; which a PSD is just a signal converted into the frequency domain and then converted into power via normalization [38, 46]. In practice, once an FRF is found, "curve fits in the Laplace domain infer the location of poles in the s-plane, and an FRF is simply the transfer function measured along the jω axis" [38], refer to Figure. 1.19 in [38] for a clear visual representation of the Laplace domain.

An example of the input and output signals included in this study's FRF analysis can be seen in Figure 2.9. Each of these signal sets are passed through a zero-phase Butterworth low-pass filter with a cut-off frequency at 240 Hz to follow the Nyquist criteria, as most of the frequencies of interest are below 120 Hz [14, 3, 16].

Figure 2.9: Shows the five consecutive hammer strikes and response from accelerometer, hammer strikes (N) are in blue and accelerometer (m/s^2) in red.

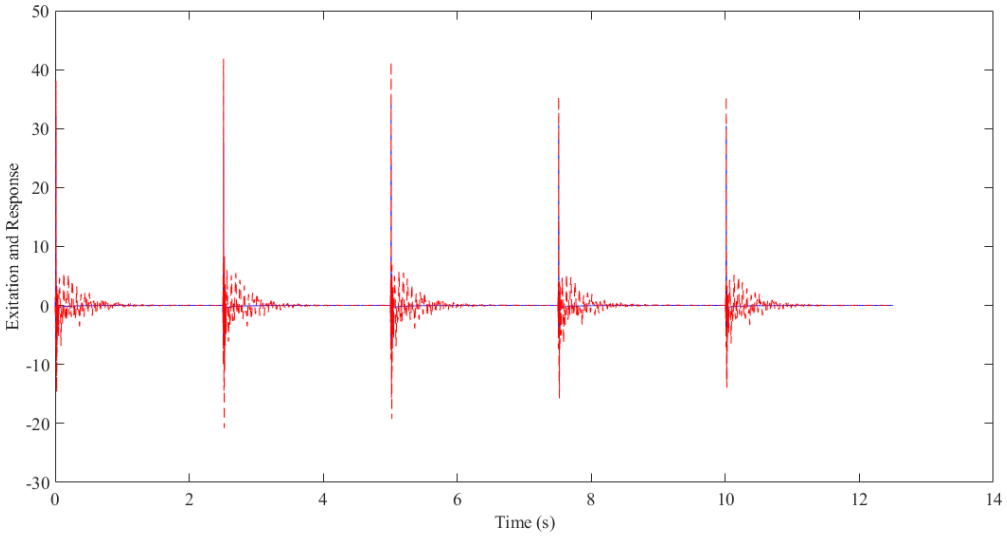

Once the data was post-processed it is fed into a function to calculate an FRF for every output node for all five impacts, each individual impact and all ten output locations are analyzed via a version of the (modalfit()) [42] function catering to a roving output; this function is further customized by specifying the measurement type and estimator type. Estimators are a way of optimizing the FRF fitting process to the particular system of interest [24]. An H_1 estimator assumes that there is only noise on the input signal, as seen in Eq.2.1 P_{yx} is the cross power spectral density of the input and output and P_{xx} is the power spectral density of the input. An H_2 estimator is when you assume that only the output signal has noise, as seen in Eq.2.2 P_{yy} is the power spectral density of the output and P_{xy} is the complex conjugate of the cross power spectral density of the input and output. The H_v estimator is when you cannot assume that either the input or output is noiseless, as seen in Eq.2.3 it is the geometric mean of the H_1 and H_2 estimators [42]. The H_v estimator minimizes the impact of noise by assuming that both the input and output have the same signal to noise ratio [24]. I used the H_v estimator for all FRF analysis in this study because of the variation in output signals types and the input signal noise was unknown.

$$H_1(\omega) = \frac{P_{yx}(\omega)}{P_{xx}(\omega)} \tag{2.1}$$

$$H_2(\omega) = \frac{P_{yy}(\omega)}{P_{xy}(\omega)} \tag{2.2}$$

$$H_v(\omega) = \sqrt{H_1(\omega)H_2(\omega)} \tag{2.3}$$

Here is an example of a transfer function for an undamped harmonic oscillator Eqs.2.4,2.5,2.6 where the numerator varies based on the outputs being measured [42]. This matters, as the response signal is proportional to the particular type of measurement [42], in this case either acceleration or displacement; as acceleration is just the second time derivative of displacement. In the FRF analysis, I specify acceleration or displacement in order to account for that change in proportion.

$$H(z) = \frac{N_{\text{Sensor}}\ (z)}{1 - 2z^{-1}\cos\Delta t + z^{-2}} \tag{2.4}$$

$$N_{\text{acc}}(z) = \left(1 - z^{-1}\right) - \left(z^{-1} - z^{-2}\right)\cos\Delta t \tag{2.5}$$

$$N_{\text{dis}}\ (z) = \left(z^{-1} + z^{-2}\right)(1 - \cos\Delta t) \tag{2.6}$$

Once an FRF is obtained, one can begin fitting modal parameters, such as natural frequencies, damping, and mode shapes; the first step to this in a multi-input multi-output (MIMO) system is to create a stability diagram (Figure 2.10) using a least-squares complex exponential fit method (LSCE) [42]. This fit method finds an impulse response function (IRF) in the time domain that correlates to the imputed FRFs, then using Prony's method fits that IRF with complex damped sinusoid functions [42]. In Eqs.2.7,2.8,2.9 all from [42], is a process for finding the amplitudes a_i and the poles x_i, where you take the superimposed set of N/2 modes (makes it so one can find N number of poles and amplitudes), seen as the h(n) functions below, to solve for the poles and

amplitudes. The poles are found via a roots solving algorithm after finding the coefficients c_n in Eq.2.8 using an autoregressive model where L=2N [42]. Once the poles are solved, both the damping and natural frequencies can be found [42], and every time a natural frequency and/or damping ratio is found within a certain range of a previous h(n) function, it is deemed stable in either frequency or frequency and damping, as seen in Figure2.10. Finally, the amplitudes are solved to facilitate the reconstruction of the IRF.

$$\begin{aligned} s_i(n) &= A_i e^{-\zeta_i n/\omega_\mathrm{s}} \cos\left(2\pi\omega_i n/\omega_\mathrm{s} + \phi_i\right) \\ &= \frac{1}{2} A_i e^{j\phi_i} \exp\left(-\left(\zeta_i/\omega_\mathrm{s} - j2\pi\omega_i/\omega_\mathrm{s}\right) n\right) + \frac{1}{2} A_i e^{-j\phi_i} \exp\left(-\left(\zeta_i/\omega_\mathrm{s} + j2\pi\omega_i/\omega_\mathrm{s}\right) n\right) \\ &\equiv a_i x_i^n + a_{i+} x_{i+}^n, \end{aligned} \tag{2.7}$$

$$h(0) = a_1 x_1^0 + a_2 x_2^0 \cdots + a_N x_N^0$$

$$h(1) = a_1 x_1^1 + a_2 x_2^1 + \cdots + a_N x_N^1$$

$$\vdots$$

$$h(N-1) = a_1 x_1^{N-1} + a_2 x_2^{N-1} + \cdots + a_N x_N^{N-1}$$

$$x_i^N + c_{N-1} x_i^{N-1} + \cdots + c_1 x_i^1 + c_0 x_i^0 = 0$$

$$\begin{bmatrix} h(0) & h(1) & \cdots & h(N-1) \\ h(1) & h(2) & \cdots & h(N) \\ \vdots & \vdots & \ddots & \vdots \\ h(L-N-1) & h(L-N) & \cdots & h(L-2) \end{bmatrix} \begin{bmatrix} c_0 \\ c_1 \\ \vdots \\ c_{N-1} \end{bmatrix} = - \begin{bmatrix} h(N) \\ h(N+1) \\ \vdots \\ h(L-1) \end{bmatrix} \tag{2.8}$$

$$\begin{bmatrix} h(0) \\ \vdots \\ h(N-1) \end{bmatrix} = \begin{bmatrix} x_1^0 & \cdots & x_N^0 \\ \vdots & \ddots & \vdots \\ x_1^{N-1} & \cdots & x_N^{N-1} \end{bmatrix} \begin{bmatrix} a_1 \\ \vdots \\ a_N \end{bmatrix} \tag{2.9}$$

Figure 2.10: Example stability diagram from preliminary testing.

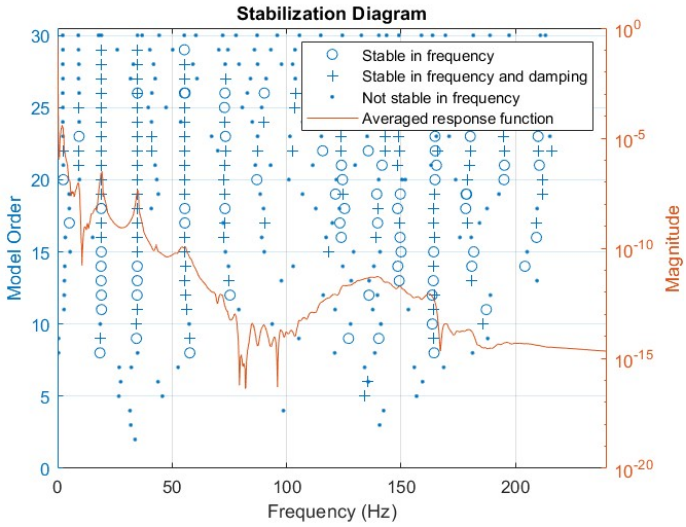

Once a stability diagram is formed, you can take the frequencies that are stable in both damping and frequency (physical frequencies) as guides for the final modal fit process. Using physical frequencies optimizes the final fit process by pinpointing a range of specific frequencies, i.e. the fit algorithm remains within a specific range rather than spanning the entire frequency range originally used when constructing the FRF [42]. The fit algorithm provides the final estimates for natural frequencies and damping ratios, as well as a reconstructed FRF (OFRF) to confirm the validity of the fit, can be seen in Figure 2.11.

Figure 2.11: The reconstructed FRFs in blue and the original FRFs in red, showing the differences in the three major components of an FRF. X: Frequency (Hz), Y: Distance Relative to Boot Center (cm), Z:a) Magnitude (dB), b) Real, c) Imaginary

(a) Magnitude

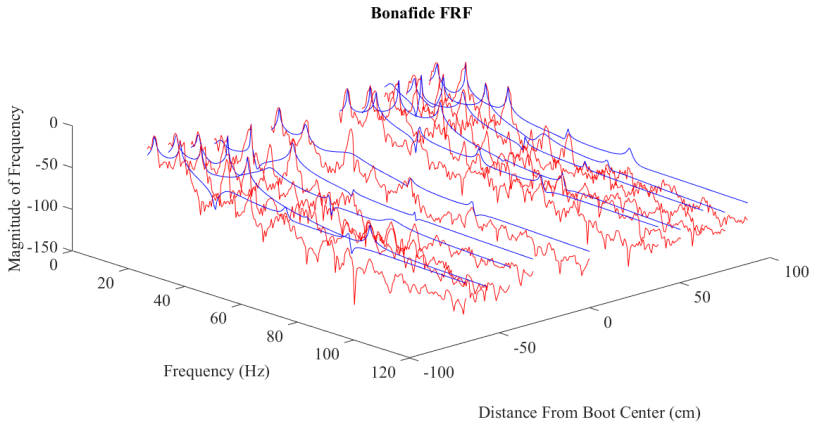

(b) Real

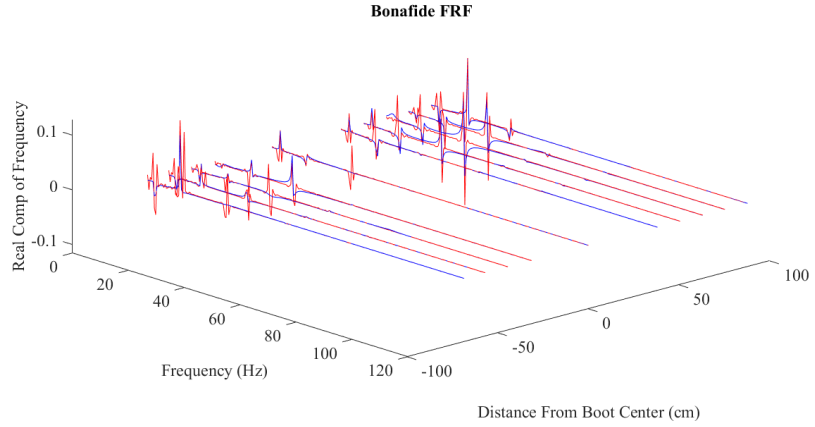

(c) Imaginary

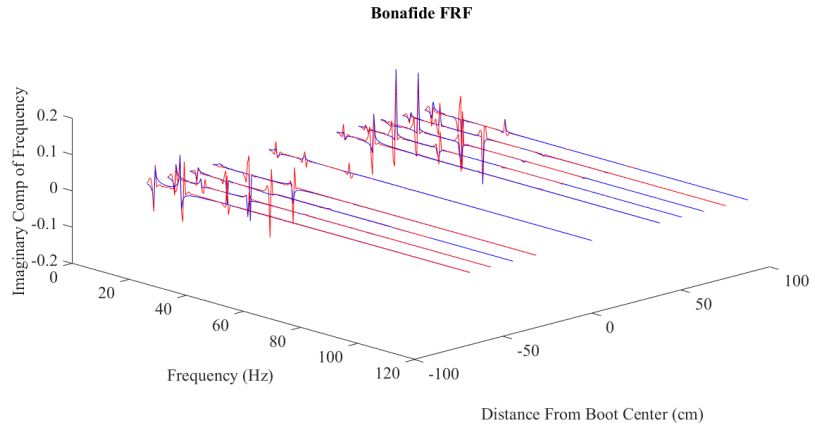

The components of an FRF have separate meanings, the magnitude of an FRF, i.e. converting the complex values into dB with the formula $20log_{10}(|H(\omega)|)$, indicates the amplitude of a specific frequency that exists in a signal. The real component of a FRF will be zero at resonant/natural frequencies and is the simultaneous response to the excitation signal, is the inversion of the imaginary component at natural frequencies, and indicates how a system absorbs energy [38, 24, 2]. The imaginary component will have a peak at resonant frequencies and represents the phase, indicates how a system dissipates energy, and the lagging response to the excitation signal [38, 24, 2].

The generalized equation for an FRF is given as Eq.2.10 and is a typical method for fitting a FRF after it's formation using estimators, specifically for modal parameters [38]. This is not the method used for modal parameter fitting in this study, but it is included because it makes more intuitive sense as to how natural frequencies, damping, and phase are connected to an FRF.

$$H(\omega) = \sum_{r=1}^{n} \frac{\phi_i \phi_j / m}{\sqrt{\left(\omega_n^2 - \omega^2\right)^2 + \left(2\xi\omega\omega_n\right)^2}} \tag{2.10}$$

2.1.3.1 Mode Shape Formation

One of the major modal characteristics you can pull out of FRF analysis is the mode shape associated with each natural frequency, a mode shape is the shape an object forms when vibrating at a natural frequency, and is how an object disperses energy. The imaginary component of an FRF can be used to derive mode shapes from an FRF as it signifies both the phase and how a system dissipates energy after a system is excited or perturbed. Look at Figures. 3.5,3.6 for a visual representation of how imaginary components can be connected in a spatially relevant fashion to derive mode shapes. The imaginary component of each mode at each IMU measurement location is either normalized relative to each other for easier viewing of the individual components or is directly taken to form the z-components of the vibration mode shape (ψ_z,ϕ_z) used in the force estimation section.

2.2 In-Field Modal Analysis

The most prevalent modal analysis technique presented in 1 was the time series/modal analysis of in-field data, whether for performance characterization [14] or in-field to laboratory correlation [16]. This technique proved to show relevance in both applications and was considered an important component of the quantitative analysis of alpine skis. Given that I had access to IMU data containing linear acceleration and gyroscopic measurements, it only made sense that in-field modal analysis should be performed for laboratory correlation of both the in-lab modal analysis and in-lab stiffness measurements. Analysis will be done using both Fast Fourier Transforms (FFT) and power spectral density analysis (PSD). All data for the in-field modal analysis used data collected during a three-day test period (03/25/2024-03/27/2024) at Crested Butte Mountain Resort in Crested Butte, CO; three expert skiers and reviewers from Blister Review skied both skis in rotation all three days in conditions ranging from freshly groomed to chopped out groomed slopes. There was one test day with fresh snow, but data from that day was not included in this analysis.

Figure 2.12: Image of test skier Dylan from Blister Reviews on the Blizzard Bonafide test ski

2.2.1 Filtering Techniques

Prior to any FFT/PSD analysis all data was filtered to remove the impact of high frequency noise, in-field data was sampled at 710 Hz [5]. The highest frequency of interest was below 90 Hz and above 6 Hz, in order to follow Nyquist criteria, a band-pass zero-phase filter was applied ranging from 1 Hz to 180 Hz. A band-pass filter was used instead of a low-pass in order to remove any frequency content caused by the ski turning, as this study is only interested in ski related characteristics, not skier.

2.2.2 Fast Fourier Transforms and Power Spectral Density Analysis

FFT and PSD analysis was performed on vertical acceleration and rotational velocity about the roll axis to capture the frequency content associated with vertical bending and torsion. An FFT is the process of converting a time-based signal into the frequency domain using Eq.2.11 below [41]. In this study I only perform a single-sided FFT using only the positive side of the symmetric function. An FFT calculates the proportion that a specific frequency exists within a signal.

$$Y(k) = \sum_{m=0}^{n-1} x_m e^{-i2km\pi/n} \tag{2.11}$$

A PSD takes the FFT one step further and calculates the power (dB) of frequency content within a signal. The PSD performed used Welch's method to perform a windowed average estimate; specifically using a Hamming window one-tenth the length of the signal; the window size was chosen for better frequency resolution [41]. It then takes the mean-square value of the FFT in each window and divides it by the sample rate for normalization, allowing comparison between data with different bandwidths [46].

The reason both types of analysis are performed is that each type caters to different forms of comparison, the FFT makes it easier to compare what particular frequencies are most prominent in a signal; which is better for comparing to the natural frequencies and damping found in laboratory analysis. While the PSD makes it easier for comparison between test skis, the in-field relationship

to dominant mode shapes, and stiffness profiles.

2.2.3 In-Field vs. Laboratory

The goal of the comparison between in-field and laboratory tests is to see if modal characteristic found in lab emerges while on-snow. Many previous studies have found correlations between laboratory-based measurements and in-field measurements 1; vibrational behavior of a ski has been directly correlated to on-snow performance [14]. If correlations are found between resonant frequencies, then the comparison to the prominence of certain mode shapes and their relationship to stiffness profiles will be explored. Given that there are relationships between measured characteristics and trends in in-field data, further correlation to a more comprehensive laboratory-based measurement framework could provide manufacturers, reviewers, and consumers with a more concrete quantitative analysis framework that allows for the connection of measured mechanical and dynamic properties with performance characteristics on-snow. Making the process of R&D or ski selection much more streamlined.

2.3 Stiffness, Displacement, and Force Estimation

The final part of analysis stems from the need to produce relevant on-snow loading scenarios for FEA simulations as attempted in multiple studies mentioned in 1. Most of the studies were successful in producing ski models that aligned with laboratory-based testing but would typically include a major assumption (ex. exclusion of vibration) [12, 47, 6]; all of them lacked real-world loading scenarios with a ski in a much less controlled environment; many of them mentioned that future work should include the creation and implementation of real-world loading scenarios (i.e. completely removing any convenient assumptions or lab-based loading scenarios that are not capable of replicating variances in ski-snow interaction, high velocities, and vibration.). In this thesis I present a framework for estimating in-situ force using three separate methods, a standard second-order system approach, a frequency domain second-order system approach, and finally an attempt at directly mapping sensor outputs to non-dimensionalized forces using known modal parameters.

A major consideration that most studies did not take into account is the possibility that skis could behave in a nonlinear fashion when vibrations and impulse loading are included, and as will be discussed in 3, the displacement or acceleration of a measurement point on a ski did not have a linear relationship with the force imputed in the limited testing presented in this study; most papers assumed a quasi-static loading scenario. When a ski is loaded in a quasi-static manner, it exhibits linear properties, but when the ski is subject to impulses of varying durations and allowed to vibrate, it is possible that it no longer behaves in a perfectly linear manner making conventional methods difficult to implement. This section will present the theoretical framework for displacement and force estimation with the inclusion of vibrations, but has maintained the assumption that there was a linear relationship between displacement and the force applied [12, 47, 6, 34, 48]. The following chapters 3,4 will discuss it's shortcomings and possible improvements or suggestions for redirection to account for the fact that the major assumption that there is a linear relationship between displacement and the force applied did not prove to be accurate in my testing.

2.3.1 Bending and Torsional Stiffness Measurements

Bending and torsional stiffness have two purposes in this study, correlation with modal characteristics and implementation of a standard second-order force estimation approach. multiple studies have measured stiffness profiles with similar end goals 1. The approach to measuring stiffness closely resembles the approach represented in [12] as it is the most similar to real-world loading. Many other methods required flexing the ski with half the ski clamped down, placing the ski in a typical cantilever loading scenario [34, 48], which, as I will discuss in the following section, is an assumption I had to make for in-situ displacement estimates due to unknown boundary conditions; but, if there is an option to load the ski where both the tip and tail are included, that is the most realistic option. The approach taken in this thesis differs from [12] in that they measure displacement, but I measure the change in slope along a ski when subjected to a force. Stiffness measurements were performed using the ski stiffness flexrig at Western Colorado University that was developed by Blister Labs and the CU/Western Engineering partnership program, as seen in

Figure 2.13. The flexrig is an automated measurement system that can measure both the bending and torsional stiffness of a ski. Each stiffness profile is an average of two measurement profiles from the flex rig.

Figure 2.13: Fully automated bending and torsional stiffness measurement rig, designed and manufactured as part of Blister Labs at Western Colorado University.

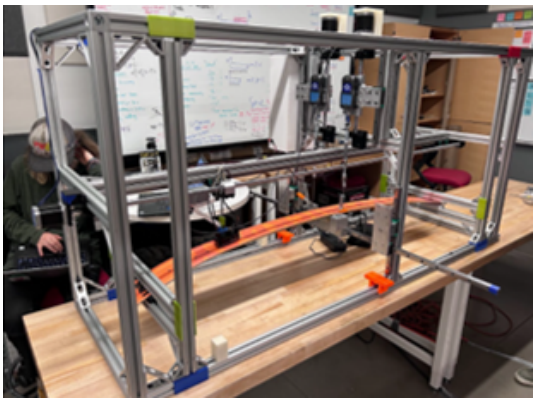

Bending stiffness, EI(x), was calculated using the derivative of the curvature of the ski under load rather than change in slope due to the extremely small differences in slope between the measurement points, causing singularities. A typical approach to calculate EI(x) can be seen in Eq.2.12. The approach taken in this study can be seen in Eqs.2.13,2.14,2.15 where using a substitution of the radius of curvature R for its inverse K, the derivative of curvature, mitigates the impact of small changes in slope along the loaded ski completely removing singularities. This was made possible by taking the slope of the ski at twenty-seven points and deriving a function representing the shape of the ski under load; this function is then subject to the methods presented.

$$EI(x) = \frac{M_z(x)}{\frac{d\theta}{dx}(x)} \tag{2.12}$$

$$EI(x) = \frac{M_z(x)}{K(x)} \tag{2.13}$$

$$K(x) = \frac{1}{R(x)} \tag{2.14}$$

$$R(x) = |\frac{(1 + \frac{dz}{dx}(x)^2)^{3/2}}{\frac{d^2z}{dx^2}(x)}| \tag{2.15}$$

Torsional stiffness was calculated using a much simpler approach due to the fact that the change in angle of twist was almost an order of magnitude higher than the change in slope in bending, allowing the use of the simplified Eq.2.16 without singularities.

$$GJ(x) = \frac{M_x(x)}{\frac{d\phi}{dx}(x)} \tag{2.16}$$

GJ(x) will not be used in the force estimation, as only the force component that contributes to vertical bending was estimated, EI(x) was further processed into a stiffness matrix following the lumped parameter model. This global stiffness matrix was simplified to one degree of freedom only accounting for motion in the z-direction, vertical displacement, so only the adjacent nodes affect each other. The ski was discretized into 10 nodes, the same number of IMU stations, and the assumed boundary condition that the IMU under the boot (x = 0) always has zero displacement, essentially treating the two half's as cantilever beams. The stiffness matrix for the second-order approximation can be seen in Eq.2.17 and the formula for each component is given in 2.18 [31], where L changes depending on if it is the front or back half of the ski and x_i is the location of the current node.

$$K = \begin{bmatrix} k_1 & -k_1 & 0 & \cdots & \cdots & 0 \\ -k_1 & k_1 + k_2 & -k_2 & 0 & \cdots & \vdots \\ 0 & -k_2 & k_2 + k_3 & \ddots & & \vdots \\ \vdots & 0 & \ddots & \ddots & & 0 \\ \vdots & \vdots & & & k_8 + k_9 & -k_9 \\ 0 & \cdots & \cdots & 0 & -k_9 & k_9 \end{bmatrix} \tag{2.17}$$

$$k_i = \frac{6(EI_i)_{avg}}{x_i^2(3L - x_i)} \tag{2.18}$$

2.3.2 Filtering and Limiting Factors

Due to in-field data acquisition system sampling at 710 Hz the raw data contains large amounts of high-frequency content that has little affect on the relative pose or deformation of the ski, in order to remove most of this content all IMU data was passed through a zero-phase low-pass filter with a cut-off frequency at 10 Hz. 10 Hz is the theoretical maximum for any rigid body motion relevant to displacement and force estimation [5]. The affect of the filter can be seen in Figure. 2.14. After filtering, all data was rotated into the North, East, Down (NED) frame to prepare it for the Kalman filter (KF) [5].

The largest limiting factor in both displacement and force estimation is the fact that this is an ill-posed problem, as boundary conditions are constantly changing and very difficult to predict and there are no unique solutions. [12] was able to create a framework to estimate boundary conditions, but this requires measurements of the mechanical properties of the snow during each data capture, the assumption that vibrations are absent, knowing when each section of the ski is actually making contact with the snow, and each set of boundary conditions will be specific to each ski/turning scenario. I think an implementation of FEA similar to [12] could allow a much easier implementation of boundary conditions, specifically for a carving turn; but for any other phenomenon experienced in skiing, it would prove extremely difficult to derive boundary conditions for. Making the problem of solving relevant on-snow loading scenarios an ill-posed problem. Another major consideration is the fact that the only sensors used in this study are IMUs, typically for any highly dynamic system, multiple sensor types are used in a larger filtering algorithm to acquire displacement/force estimates [48, 20, 17, 19, 18]. An attempt is made to derive a framework for using IMUs in place of strain gauges by estimating the relative pose change between IMU stations, but there is no way to estimate the force inputted by the skier at the binding due to the lack of load cells/pressure sensors as used in [12, 48]. At best, this particular sensor system is only capable of estimating the component of force that causes the ski to bend. This issue affects each of the three force estimation techniques in different ways and will be further discussed in each of their respective sections.

Figure 2.14: Visualization of low pass filter applied to data prior to Kalman filter pose estimation [5].

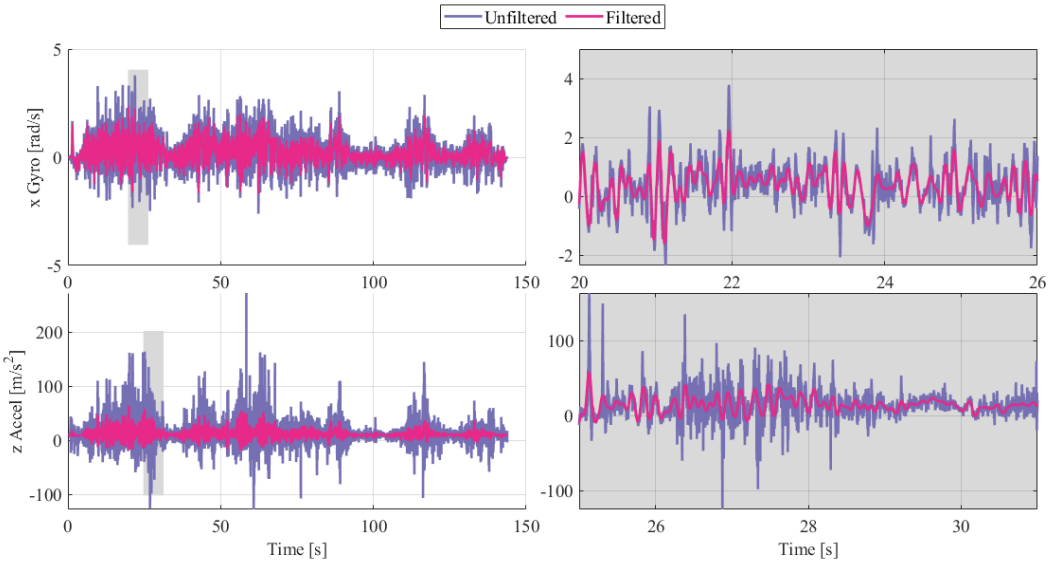

2.3.3 Displacement Estimation

As mentioned previously, the sensor system used in this study consists only of IMUs, which are not typically used to estimate displacement in isolation. Typically, this is the job of strain gauges, as it is much simpler and more accurate to convert strain to deformation to relative displacement [48, 20, 17, 19, 18]; especially in a system exposed to high relative accelerations or experiencing highly dynamic phenomena. With that said, an IMU and, more specifically, a system of IMUs do a good job of estimating the local pose using a KF [5]. Leveraging the fact that a ski is essentially a beam and typically deforms in a way that most second-order systems do. I can relate the relative pose of each IMU station making the assumption that the general shape of the ski at any point in time will not deviate from a shape resembling the first or second mode of vibration (displacements that contribute to the majority of force applied would typically occur at frequencies below 10 Hz [5]).

The KF used in this study is the Indirect Complementary KF which uses an error state vector, rather than an absolute state vector, and fuses the accelerometer and gyroscope readings to

form a pose estimate [5, 39]. For more information on the inner workings of this KF please refer to [5, 39]. The outputs of the KF are quaternions that are then converted to Euler angles using the Z-Y-X/3-2-1 rotation sequence. This sequence was specifically chosen because all calculations are in reference to the body frame, singularities/gimbal lock was not a concern, as both the pitch and roll estimates should never exceed ± 90 degrees, yaw estimates are not used in follow-on calculations.

Using the estimate for pitch (θ_i) from the KF you can estimate the relative slope of the IMU station using Eq.2.19, after estimating the slope of each IMU station using the known spacing between each station, one can fit a second-degree polynomial function to the front and rear estimates separately (essentially treating each half of the ski like a cantilever beam). A second-degree polynomial was chosen to represent the previously mentioned fact that the shape of the ski should resemble the first or second mode of vibration, since a ski can typically be modeled as a second-order beam [12, 34, 48]. Now that a function representing the slope of the ski along the x-axis has been derived, the overall orientation of the ski needs to be accounted for (i.e. the pitch of the ski slope) in order for the slope to be local to the ski's body frame. This is done by driving the slope function estimate for the center IMU to zero and removing that slope estimate from the remaining IMU stations, see Figure A.1. With the pitch-corrected slope function the integral of that function, as shown in Eq. 2.20, is taken to form a polynomial function that represents the z-position of the ski along the x-axis, this function is evaluated at each of the IMU stations to provide an estimated z-position relative to the center IMU. The average of the first second (710 instances) of z-position estimates is considered z_0 and is subtracted from all z-position estimates to provide an estimate of displacement for all time steps in a data capture. Estimate error is calculated by comparison to ground-truth data captured by MOCAP, the process is discussed further in the following sections.

$$\frac{dz_i}{dx_i} = tan(\theta_i) \tag{2.19}$$

$$z(x) = \int \frac{dz_i}{dx_i}(x)dx \tag{2.20}$$

2.3.4 Force Estimation

All of the supplementary information has been compiled over the whole of this chapter in order to attempt in-situ force estimation; due to the issue mentioned previously, three different techniques were tested to see if there was a best option. The first is to utilize a standard second-order approach using the derived stiffness matrix and a derived mass matrix (found via the lumped parameter method), damping is not accounted for in this technique due to the fact that it is negligible in vertical bending, as will be discussed in 3. The second and third methods are related in the inclusion of modal parameters such as mode shapes, modal displacement, modal velocity, and modal acceleration; one approach uses the frequency domain version of a second-order function, the other uses a direct sensor mapping method closely related to the method presented in [20, 17, 19, 18].

An additional step is taken during the KF pose estimation process in order to keep track of the direction of gravity and it's magnitude in the local z-direction, this is done by taking the average of the first second (710 instances) the z-component of each IMU's z-acceleration component and treating that as the initial gravity vector , as seen in Eq.2.21, and finding the rotation of that vector for every time step in the KF algorithm. This is done using the technique in Eq.2.21 which is the process of converting a quaternion to a rotation matrix. This process is performed for all ten IMU stations at each time step. This process was done in order to remove the component of gravity contributing to the z-acceleration prior to force estimation. As mentioned previously, the goal is to find the component of force that contributes to bending the ski; the force caused by the mass of the ski itself is negligible when compared to the component imparted by stiffness, and it is not possible to know the exact contact scenario/boundary condition at each time step, making the inclusion of gravity difficult to accurately implement.

$$\hat{g}(i) = \begin{bmatrix} 1-2s\left(q_3^2+q_4^2\right) & 2s\left(q_2q_3-q_4q_1\right) & 2s\left(q_2q_4+q_3q_1\right) \\ 2s\left(q_2q_3+q_4q_1\right) & 1-2s\left(q_2^2+q_4^2\right) & 2s\left(q_3q_4-q_2q_1\right) \\ 2s\left(q_2q_4-q_3q_1\right) & 2s\left(q_3q_4+q_2q_1\right) & 1-2s\left(q_2^2+q_3^2\right) \end{bmatrix} \begin{bmatrix} 0 \\ 0 \\ a_{zavg(i)} \end{bmatrix} \tag{2.21}$$

2.3.4.1 Standard Second Order Estimation

This is a technique derived from the knowledge that using typical beam theory would prove extremely difficult due to the lack of known boundary conditions and knowing that the ski does not react like a typical linear homogeneous beam would. The thought of approaching this problem as if it were just a big spring mass damper system was more out of an internist in seeing if the technique was viable, rather than it being something that had been previously attempted for skis. It was inspired by the fact that in [20, 17, 19, 18] a similar method was used to success, the difference being the frequency domain version of a typical second-order system with a basis in the assumed mode method. Given the fact that I already had access to the stiffness matrix, mass matrix, accelerations, and displacement estimates, why not test it's viability. This method uses Eq.2.22, where M and K are the mass and stiffness matrix, respectively, both are ten-by-ten matrices, z" (as mentioned before gravity is removed, i.e. $\hat{g}$) and z are the acceleration and displacement, respectively, for each IMU station, each are a ten-by-one vector. This results in a ten-by-one vector representing the force applied at each of the ten IMU stations. The force due to damping is excluded due to a ski being such an under-damped system in bending that it makes its impact negligible.

$$F = M(\hat{z}'' - \hat{g}) + K\hat{z} \tag{2.22}$$

One of the issues with the next two force estimation methods is that they are both non-dimensional, meaning that they both require some sort of fitting or post processing to dimensionalize the estimate. This standard second-order approach provides an estimate that does not require further processing to relate it to ground-truth data/measurements. The major thing to note is that the accuracy of this estimate is extremely reliant on accurate deflection estimates and that the ski reacts in a linear/quasi-linear manner when subjected to various loads at different loading rates. which, as mentioned previously, did not end up being the case in my limited testing. These force estimates will be compared to ground truth collected with a load cell that will be further explored in 3.

2.3.4.2 Frequency Domain Second-Order Estimation and Sensor Output Mapping

A similar problem to estimating the forces and general states of alpine skis is that of flexible wings as both present issues with creating accurate boundary conditions, have high amounts of vibration, difficulty in measuring in-situ loading scenarios, and the changes in form cause inconsistencies in model to real-world correlations [20]. [20, 17, 19, 18] has developed a framework for estimating aerodynamic and generalized forces using direct sensor mapping, based on the assumed modes method. Here, I will modify the framework presented in [20, 17, 19, 18] for use with alpine skis, where instead of aerodynamic forces, it will be hydrodynamic forces from snow contact that cause the ski to bend. The estimation of generalized forces will remain mostly unchanged except for the contact surface area and pressure distribution is unknown, and is based on the assumption that all deformations fall in the linear elastic range as mentioned in [20]. Generalized forces are the contribution of force that each vibrational mode produces when a structure deforms and can be represented as a second-order system, as seen in Eq.2.23.

$$C_Q = \ddot{\eta}_i + 2\zeta_i\omega_i\dot{n}_i + \omega_i\eta_i \tag{2.23}$$

In order to estimate the nondimensional generalized forces, η and its derivatives (modal displacement, modal velocity, and modal acceleration) have to be estimated for all time steps, this process involves the main characteristic of the assumed modes methods using Eqs.2.24,2.26 that can be simplified using Einstein notation [20] into Eqs.2.25,2.27 for future use in other calculations. ψ_k,ϕ_k are the components of a mode shape vector at the location described by the vector r for displacement and acceleration, respectively, in my use case r only consists of x and z components given that all IMU stations are along the y-axis and only vertical bending forces are estimated.

$$d(r,t) = \sum_{M}^{k=1} \psi_k(r)\eta_k(t) \tag{2.24}$$

$$d(r,t) = \psi_k\eta_k \tag{2.25}$$

$$a(r,t) = \sum_{M}^{k=1} \phi_k(r)\ddot{\eta}_k(t) \tag{2.26}$$

$$a(r,t) = \phi_k \ddot{\eta}_k \tag{2.27}$$

η and its derivatives have to be calculated for every time step in order to find the contribution of each mode to displacement/force experienced by a beam. The process for this is a least-squares fit using the mode shape matrices derived from the laboratory modal testing as seen in Eqs.2.28,2.29, where Δz_i is the displacement estimate at a specific IMU location, and a_z^i is the acceleration component in the z-direction from the IMU data post filtering. Only five mode shapes were considered due to the minimal to negligible impact the fifth mode had on each skis dynamics; any higher modes were deemed unnecessary. A problem that arises from using five modes for ten measurement stations is that the mode shape matrices are not square; I made use of Eqs.2.30,2.31 as presented in [17] to allow for efficient and accurate least-squares estimation; Ψ and Φ are the mode shape matrices for displacement and acceleration respectively . To calculate modal velocity, I had to take the numerical derivative of modal displacement, similar to the standard second-order method, damping/velocity has a negligible impact on the overall (extremely under-damped in bending) estimate that not having a direct measurement is not significant in this use case.

$$\begin{bmatrix} \Delta z_1 \\ \Delta z_2 \\ \vdots \\ \vdots \\ \Delta z_{10} \end{bmatrix} = \begin{bmatrix} \psi_1^1 & \psi_2^1 & \psi_3^1 & \psi_4^1 & \psi_5^1 \\ \psi_1^2 & \psi_2^2 & \psi_3^2 & \psi_4^2 & \psi_5^2 \\ \vdots & \vdots & \vdots & \vdots & \vdots \\ \vdots & \vdots & \vdots & \vdots & \vdots \\ \psi_1^{10} & \psi_2^{10} & \psi_3^{10} & \psi_4^{10} & \psi_5^{10} \end{bmatrix} \begin{bmatrix} \eta_1 \\ \eta_2 \\ \eta_3 \\ \eta_4 \\ \eta_5 \end{bmatrix} \tag{2.28}$$

$$\begin{bmatrix} a_z^1 \\ a_z^2 \\ \vdots \\ \vdots \\ a_z^{10} \end{bmatrix} = \begin{bmatrix} \phi_1^1 & \phi_2^1 & \phi_3^1 & \phi_4^1 & \phi_5^1 \\ \phi_1^2 & \phi_2^2 & \phi_3^2 & \phi_4^2 & \phi_5^2 \\ \vdots & \vdots & \vdots & \vdots & \vdots \\ \vdots & \vdots & \vdots & \vdots & \vdots \\ \phi_1^{10} & \phi_2^{10} & \phi_3^{10} & \phi_4^{10} & \phi_5^{10} \end{bmatrix} \begin{bmatrix} \ddot{\eta}_1 \\ \ddot{\eta}_2 \\ \ddot{\eta}_3 \\ \ddot{\eta}_4 \\ \ddot{\eta}_5 \end{bmatrix} \tag{2.29}$$

$$\hat{\eta} = (\Psi^T \Psi)^{-1} \Psi^T \Delta \hat{z} \tag{2.30}$$

$$\hat{\ddot{\eta}} = (\Phi^T \Phi)^{-1} \Phi^T \hat{a}_z \tag{2.31}$$

All components necessary have been solved for allowing for the estimation of nondimensional generalized forces at every time step, but those same values can be repurposed in a direct sensor output mapping equation that takes the combination of assumed modes and pose-corrected acceleration to estimate nondimensional hydrodynamic forces at each sensor station. First, I will present the vector definitions of the sensor location to output. Then I will present the equation that results from that vector-based mapping. For reference, N is the Newtonian inertial reference frame [19], O is the origin, and B is the ski body. To begin, $\mathbf{r}^{OD}$ is the vector from the origin to a new point after displacement, it is the sum of the vectors presented in Eq.2.32 where C is the initial point and D is the end point [19].

$$\mathbf{r}^{OD} = \mathbf{r}^{OB*} + \mathbf{r}^{B*C} + \mathbf{r}^{CD} \tag{2.32}$$

Once the definition for $\mathbf{r}^{OD}$ has been formed you can take the time derivative with respect to N to get Eq.2.33 [19].

$$\begin{aligned} {}^N\mathbf{v}^D &= \frac{{}^N d}{dt}\left(\mathbf{r}^{OD}\right) \\ &= \frac{{}^N d}{dt}\left(\mathbf{r}^{OB^\star}\right) + \frac{{}^N d}{dt}\left(\mathbf{r}^{B^\star C} + \mathbf{r}^{CD}\right) \\ &= {}^N\mathbf{v}^{B^\star} + \omega \times \left(\mathbf{r}^{B^\star C} + \mathbf{r}^{CD}\right) + {}^B\mathbf{v}^D \end{aligned} \tag{2.33}$$

Once again, you can take the timed derivative of the velocity vector with respect to N to get a vector definition for the acceleration vector Eq.2.34, all of the equations presented use the two identities 2.35 and 2.36 [19]. One thing to note is that all of these equations assume that the sensor is located at the ski's center of mass.

$$\begin{aligned} {}^N\mathbf{a}^D &= \frac{{}^N d}{dt}\left({}^N\mathbf{v}^D\right) \\ &= \frac{{}^N d}{dt}\left({}^N\mathbf{v}^{B^\star}\right) + \frac{{}^N d}{dt}\left(\boldsymbol{\omega} \times \left(\mathbf{r}^{B^\star C} + \mathbf{r}^{CD}\right)\right) + \frac{{}^N d}{dt}\left({}^B\mathbf{v}^D\right) \\ &= {}^N\mathbf{a}^{B^\star} + 2\boldsymbol{\omega} \times {}^B\mathbf{v}^D + \boldsymbol{\alpha} \times \left(\mathbf{r}^{B^\star C} + \mathbf{r}^{CD}\right) + \boldsymbol{\omega} \times \left[\boldsymbol{\omega} \times \left(\mathbf{r}^{B^\star C} + \mathbf{r}^{CD}\right)\right] + {}^B\mathbf{a}^D \end{aligned} \tag{2.34}$$

$$\alpha = \frac{^N d\omega}{dt} \tag{2.35}$$

$$\frac{^N d}{dt}(\mathbf{r}^{B*C}) = \omega \times \mathbf{r}^{B*C} \tag{2.36}$$

When the accelerometer is no longer at the ski's center of mass, the vector equation for that accelerometer's output becomes 2.37 [19].

$$\mathbf{a}^D = \mathbf{a}^{B^\star} + 2\boldsymbol{\omega} \times {}^B\mathbf{v}^D + \boldsymbol{\alpha} \times \left(\mathbf{r}^{B^\star C} + \mathbf{r}^{CD}\right) + \boldsymbol{\omega} \times \left[\boldsymbol{\omega} \times \left(\mathbf{r}^{B^\star C} + \mathbf{r}^{CD}\right)\right] + {}^B\mathbf{a}^D \tag{2.37}$$

To further explain the meaning of each term in Eq.2.37, the furthest left is the local acceleration due to structural deformation, the furthest right is the acceleration of the skis center of mass, and the three terms in the middle are the centripetal, tangential, and Coriolis accelerations, respectively [19]. Substituting the left most term in Eq.2.37 with Eq.2.38 and expanding each vector into its scalar definition Eqs.2.39,2.40,2.41,2.42,2.43 ($\mathbf{b_1}, \mathbf{b_2}, \mathbf{b_3}$ are the body frame axes) gives Eq.2.44.

$$\mathbf{a}^{B^\star} = \frac{^{B^*} d}{dt}\left({}^N\mathbf{v}^{B*}\right) + \omega \times \left({}^N\mathbf{v}^{B*}\right) \tag{2.38}$$

$$\omega = p\mathbf{b_1} + q\mathbf{b_2} + r\mathbf{b_3} \tag{2.39}$$

$$\alpha = \dot{p}\mathbf{b_1} + \dot{q}\mathbf{b_2} + \dot{r}\mathbf{b_3} \tag{2.40}$$

$$\mathbf{r}^{CD} = \sum_{k=1}^{M}\left(\phi_{k_x}\eta_k\mathbf{b}_1 + \phi_{k_y}\eta_k\mathbf{b}_2 + \phi_{k_z}\eta_k\mathbf{b}_3\right) \tag{2.41}$$

$${}^B\mathbf{v}^D = \frac{^B d}{dt}\left(\mathbf{r}^{CD}\right) = \sum_{k=1}^{M}\left(\phi_{k_x}\dot{\eta}_k\mathbf{b}_1 + \phi_{k_y}\dot{\eta}_k\mathbf{b}_2 + \phi_{k_z}\dot{\eta}_k\mathbf{b}_3\right) \tag{2.42}$$

$${}^B\mathbf{a}^D = \frac{^B d}{dt}\left({}^B\mathbf{v}^D\right) = \sum_{k=1}^{M}\left(\phi_{k_x}\ddot{\eta}_k\mathbf{b}_1 + \phi_{k_y}\ddot{\eta}_k\mathbf{b}_2 + \phi_{k_z}\ddot{\eta}_k\mathbf{b}_3\right) \tag{2.43}$$

$$\begin{aligned} a_{z_D} - g_{z_D} =& \frac{C_Z}{M} + (pr - \dot{q})\left(x_s + \phi_{k_x}\eta_k\right) + (qr + \dot{p})\left(y_s + \phi_{k_y}\eta_k\right) \\ & - \left(p^2 + q^2\right)\left(z_s + \phi_{k_z}\eta_k\right) + 2\left(\phi_{k_y}p - \phi_{k_x}q\right)\dot{\eta}_k + \phi_{k_z}\ddot{\eta}_k \end{aligned} \tag{2.44}$$

Due to the fact that y_s is zero for all IMU stations and $\ddot{\eta}_k$ is multiple orders of magnitude larger than $\dot{\eta}_k$ and η_k you can remove those terms from Eq. 2.44 to get a simplified version in Eq.2.45 [19]. This stems from their theoretical definition where $\ddot{\eta}_k$, η_k, and η_k are sin functions multiplied by ω_i^2, ω_i, and 1 respectively [19], equations will be in Appendix A A.1. This lines up in my own implementation, and they do have a negligible impact on the estimate. This framework can provide estimates in all three directions, but as mentioned previously, this study is only interested in estimating the force that results in vertical bending (i.e. z). M is the mass matrix of the ski.

$$a_{z_D} - g_{z_D} = \frac{C_Z}{M} + (pr - \dot{q})x_s - \left(p^2 + q^2\right)z_s + \phi_{k_z}\ddot{\eta}_k \tag{2.45}$$

Once an estimate for C_Q and C_z (nondimensional generalized and hydrodynamic force) is found for all IMU stations for all time steps, a scaling factor must be derived from ground-truth data. Ground-truth data was collected via a Forsentek FSSM (0-1000N) compression load cell, thirty instances of quasi-static or close to quasi-static loading per ski; the ski is placed in a cantilever loading scenario with MOCAP capturing ground truth data for displacement. MOCAP was time-synced to the skis data capture system using a marker on the switch and visual of the LED turning on for record. A scaling factor was calculated between the maximum value of the sum of C_z and the sum of C_Q and the corresponding ground-truth data point. All thirty scaling factors are averaged and a standard deviation is found to provide an error estimate based off the scaling factor; a root mean-squared-error is also found for each scaled instance of C_z/C_Q and the corresponding ground truth data point. The same root-mean-squared error calculation process is applied to the standard second-order technique. All three technique's error are then compared and a "best" is selected for boot camera video time synchronization, further comparisons with the displacement estimate, and correlation with the roll of the ski. As will be discussed in 3 and 4 all three have issues, generally associated with the fact that either the assumption that a ski maintains a quasi-linear relationship

with the force applied and the displacement experienced is not entirely correct, or the force-focused ground-truth collection process is not as accurate as it needs to be.

Chapter 3

Results

3.1 Laboratory Modal Analysis

Accelerometer-based modal analysis was collected to capture modal characteristics in vertical bending and for validation data to prove the viability of MOCAP-based modal testing. Once MOCAP was proven as a viable system for modal data capture, it was used to capture torsional modal characteristics, as MOCAP allows for much more efficient data capture when there are multiple points of interest. After measurement systems are compared, measured modal characteristics will be discussed.

3.1.1 Accelerometer vs. MOCAP

One of the important steps to fitting FRFs as discussed in 2, is the formation of stability diagrams. Stability diagrams can provide insight as to which particular frequencies and damping ratios emerge consistently throughout the LSCE fit process; peaks that emerge as both stable in frequency and damping are what are considered the physical frequencies and are considered to be the natural frequencies and damping ratios associated with the structure of interest. Comparison between the stability diagrams produced from accelerometer-based impact testing and ones produced by MOCAP-based impact testing can show if MOCAP-based testing is finding similar natural frequencies and damping ratios, as regardless of whether the test is acceleration- or displacement-based the resonant frequencies and damping ratios should theoretically remain consistent. Variations between the two types of test should theoretically arise only in the phase and

magnitude of the FRF.

In Figures 3.1,3.2 stability diagrams for acceleration and MOCAP-based, respectively, can be seen. Each of these are pulled from the same measurement location on the ski for comparisons sake, the orange is the magnitude of the FRF in each location, and we can see a few traits that are inherent to the different types of testing. First, the response at higher frequencies is more pronounced in acceleration-based testing due to the theoretical scaling factor ω_i^2 as mentioned by [19], this relationship also surfaces as broader less pronounced peaks. Aside from the differences that align with theory, the peaks that are stable in both frequency and damping align, this is further reinforced by the natural frequencies and damping ratios that were found via the physical frequencies found in these stabilization diagrams. This can be seen in Tables.3.1,3.2, where the average percent error (based on the standard deviation (STD) of the mean between test types) for the estimated natural frequencies across both skis is 1.5204%. There is a much larger average percent error for the damping ratios, 54.5288%, across both skis. This is not indicative of the relative accuracy between measurement types, as in reality the MOCAP-based testing actually produced much more consistent results when estimating damping ratios than the accelerometer-based testing, 51.0697% and 118.8618% average percent errors (based on the STD of the mean between locations in each respective test separately, not the mean between test types if there was any confusion), respectively. This large variance in damping ratio estimates can be the result of multiple factors, one that is known and has been observed in skis by prior work [16] is the presence of modal coupling (will be discussed further in the following sections), one can stem from either measurement errors, the FRF fitting process was not optimized, another is variable stiffness and geometry, and the last is the assumption that the system behaves linearly to perturbations but in reality exhibits nonlinear behavior. Based on the high accuracy of the natural frequency fit across all tests and the fact that all other measured modal parameters align with theory [38, 24], I would deem the FRF fitting method not being optimized to not be the primary source of error (can still contribute to the error, but it is more likely a combination of all the issues mentioned). With the data provided, I cannot speak about which factor contributes the most to the high variance, but

other studies have reported damping ratios that vary wildly depending on fixturing [3], or did not report an error but provided a wide range [14].

Figure 3.1: Accelerometer-based stability diagrams from FRF analysis, there are larger versions in Appendix A

(a) Bonafide

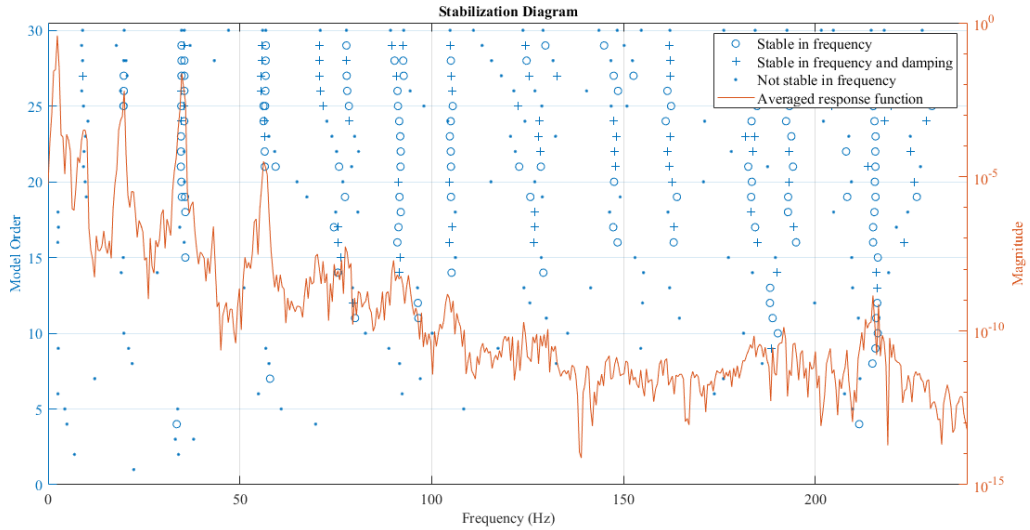

(b) Rustler

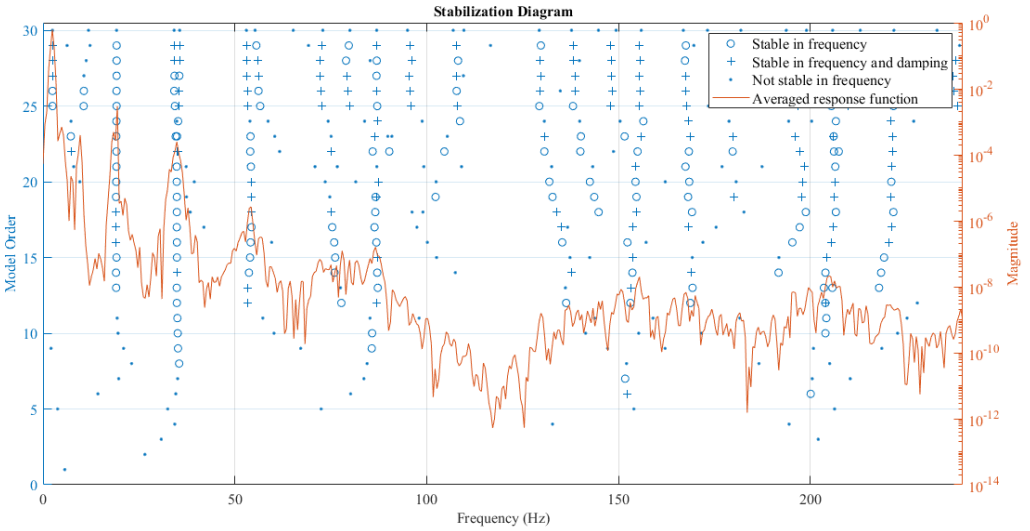

Figure 3.2: MOCAP-based stability diagrams from FRF analysis, there are larger versions in Appendix A

(a) Bonafide

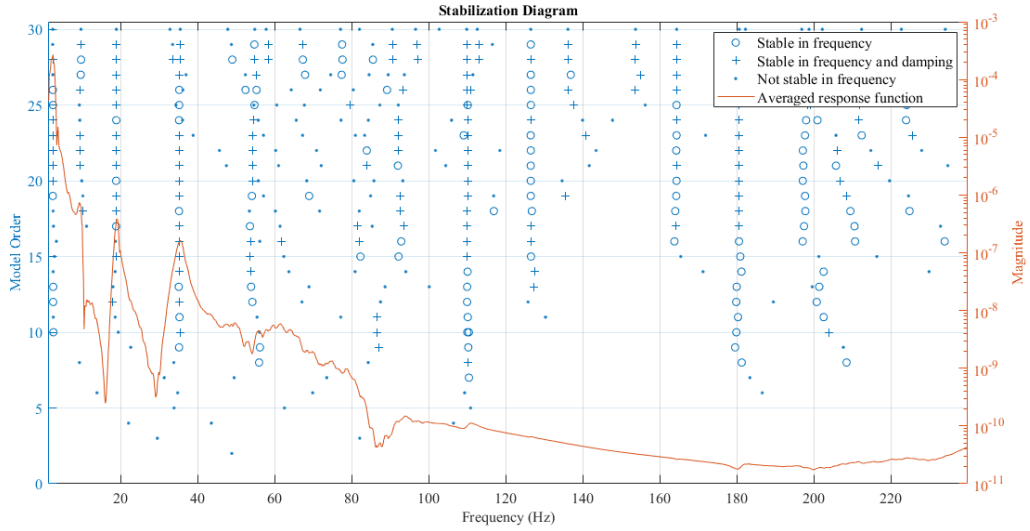

(b) Rustler

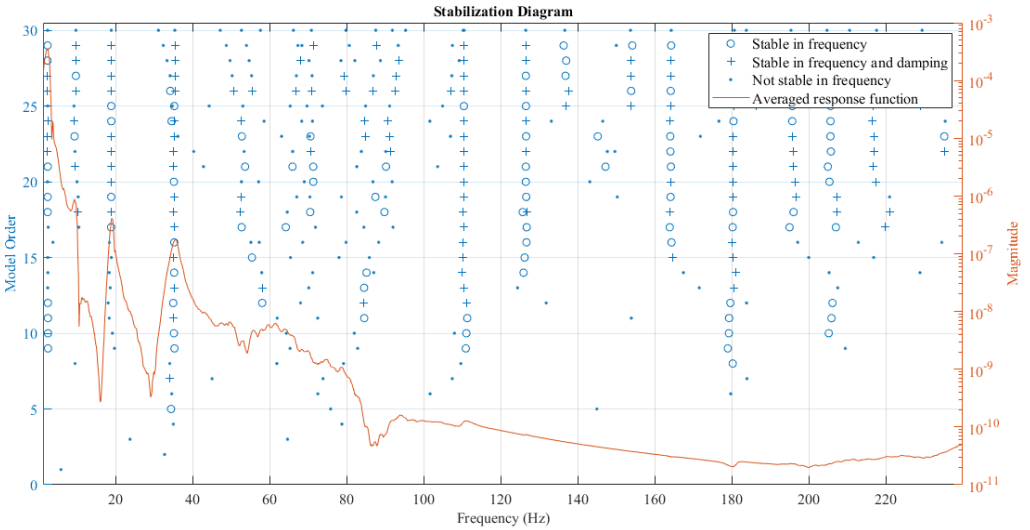

After comparing results for vertical bending modal analysis between the two systems, I do think that MOCAP is a viable system for use in modal analysis, as long as the modes of interest remain below 120 Hz to maintain adherence to Nyquist Criterion. With that conclusion, I will proceed with the use of MOCAP for the capture of torsional modal characteristics and the capture

of the mode shape matrices for displacement in vertical bending. Any points not captured along the chord of the ski by MOCAP (just three points, the remaining seven were captured via MOCAP) were acquired by scaling and phase correcting the corresponding points from the acceleration-based testing.

Table 3.1: Comparison of the natural frequencies (Fn) and damping ratios (Dr) found for the Bonafide test ski using two different measurement systems, the STD presented is that of the mean between the two measurement types.

Mode	Fn Accel. (Hz)	Fn MOCAP (Hz)	STD (Hz)	Dr Accel	Dr MOCAP	STD
1^{st}	9.455	9.7192	0.187	0.0342	0.0487	0.0102
2^{nd}	19.600	18.687	0.646	0.0038	0.0366	0.0232
3^{rd}	34.876	35.362	0.344	0.0215	0.0443	0.0161
4^{th}	56.165	55.101	0.753	0.0085	0.0304	0.0155
5^{th}	78.161	78.588	0.302	0.0072	0.0262	0.0134

Table 3.2: Comparison of the natural frequencies (Fn) and damping ratios (Dr) found for the Rustler test ski two different measurement systems, the STD presented is that of the mean between the two measurement types.

Mode	Fn Accel. (Hz)	Fn MOCAP (Hz)	STD (Hz)	Dr Accel	Dr MOCAP	STD
1^{st}	9.253	9.653	0.283	0.0543	0.0483	0.0043
2^{nd}	19.109	18.778	0.234	0.0136	0.0269	0.0094
3^{rd}	34.903	35.306	0.286	0.0211	0.0460	0.0176
4^{th}	53.957	54.860	0.638	0.0239	0.0182	0.0041
5^{th}	86.765	85.623	0.807	0.0082	0.0246	0.0116

3.1.2 Modal Characteristics of Skis

Now that MOCAP has been proven to be a viable measurement system, the collection and analysis of both acceleration- and displacement-based modal data can be discussed. To begin, separation and spatial plotting of the three components of the FRF to allow for easy comparison between measurement locations and use in mode shape formation. In Figure.3.3 the magnitude and real component of the FRFs from both test skis are plotted in accordance with their respective measurement locations. The magnitude plot can be used to see the effect of modal coupling, reso-

nances, and anti-resonances [24]. The real component is used to identify the resonant frequencies and how the ski stores energy when subject to an impact [24]. In that same figure, we can see that both skis store the most acceleration-based energy in the first and second modes. The Bonafide has higher overall magnitudes of the real components of the FRF meaning, it stores more total energy in the first two modes than the Rustler. In Figure.3.4, it is interesting to see that when considering displacement the Bonafide maintains that most of the excitation energy is stored in the first two modes, while the Rustler stores most of its energy in the second mode alone, and much less energy when compared to the Bonafide. As will be discussed in the next section, these traits align with the expectations acquired from the stiffness profiles. After finding the resonant frequencies, finding the associated imaginary component is the only remaining process to find all modal characteristics possible, via an impact test.

Figure 3.3: Results from acceleration-based FRF analysis on the two test skis, the top plots are the FRF magnitude and the bottom are the real components of the FRFs; there are larger versions in Appendix A. X:Frequency (Hz), Y:Distance Relative to Boot Center (cm), Z:a,b) Magnitude (dB), c,d) Imaginary

(a) Bonafide

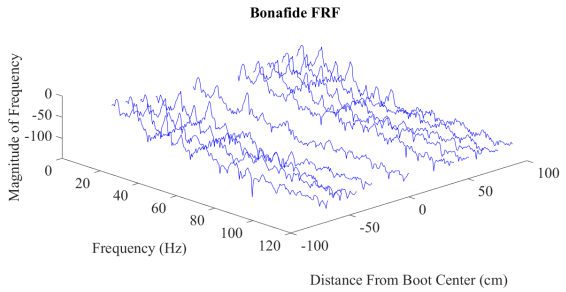

(b) Rustler

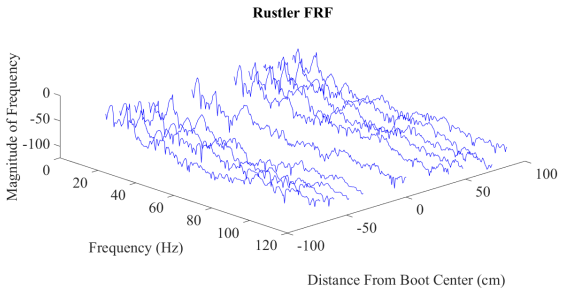

(c) Bonafide

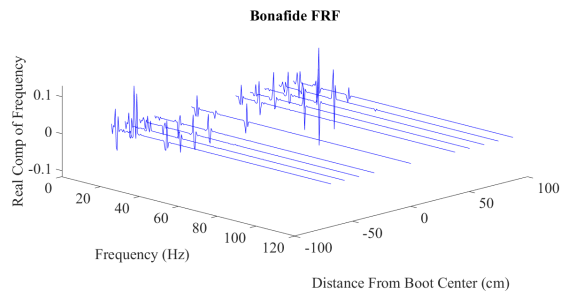

(d) Rustler

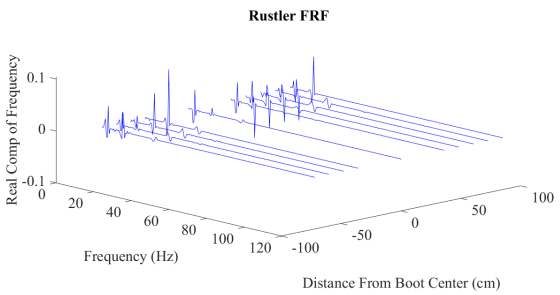

Figure 3.4: Results from displacement-based FRF analysis on the two test skis, the plots show the real components of the FRFs; there are larger versions in Appendix A. X: Frequency (Hz), Y: Distance Relative to Boot Center (cm), Z: Real

(a) Bonafide

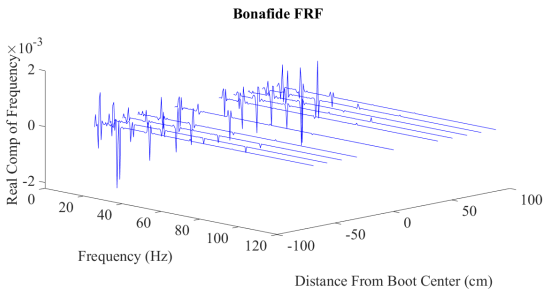

(b) Rustler

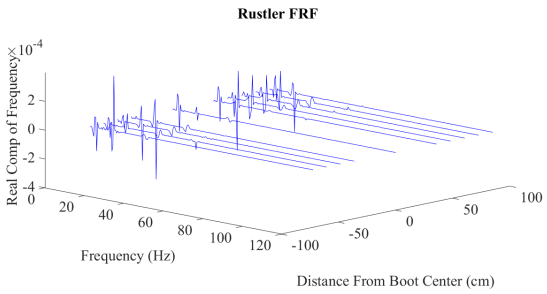

After finding the imaginary components of both the acceleration- and displacement- based testing we can derive mode shapes and make comparative conclusions about each ski's ability to dissipate/release energy, the imaginary component shows the phase and its magnitude provides insight on how a system releases energy. Looking at Figures.3.5,3.6 we can see the acceleration- and displacement-based response, respectively. Once again both skis show the most active mode in acceleration and the mode that releases the most energy is the second mode, they differ in that the Bonafide also releases a similar amount of energy in both the first and third modes. Similarly to the conclusions made about energy storage in acceleration, the Bonafide releases the most amount of energy in both the first and second modes, while the Rustler releases almost all of its energy via the second mode.

Figure 3.5: Accelerometer-based imaginary component of FRF analysis, this is how mode shape vectors are derived via experimental data; there are larger versions in Appendix A. X: Frequency (Hz), Y: Distance Relative to Boot Center (cm), Z: Imaginary

(a) Bonafide

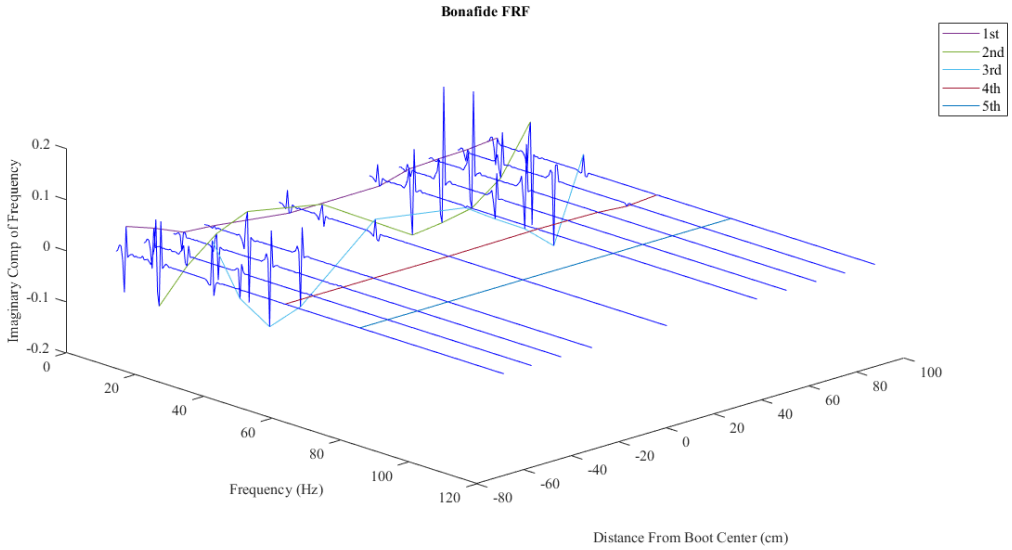

(b) Rustler

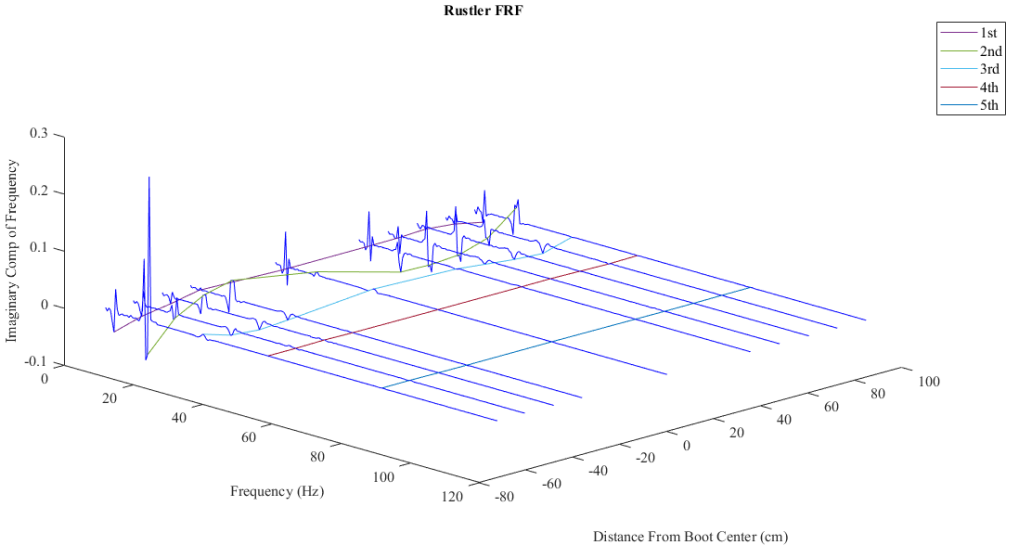

Figure 3.6: MOCAP-based imaginary component of FRF analysis, this is how mode shape vectors are derived via experimental data; there are larger versions in Appendix A. X:Frequency (Hz), Y:Distance Relative to Boot Center (cm), Z:Imaginary

(a) Bonafide

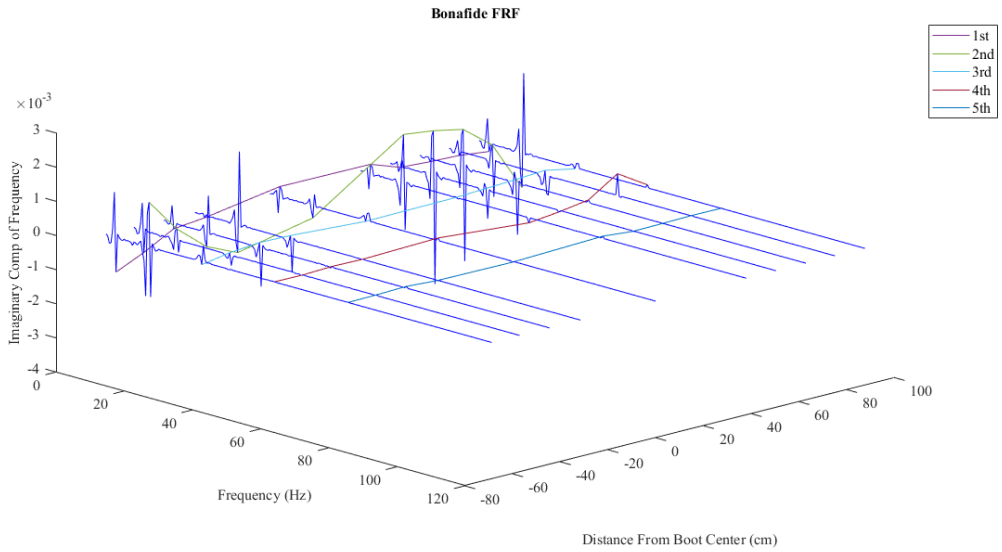

(b) Rustler

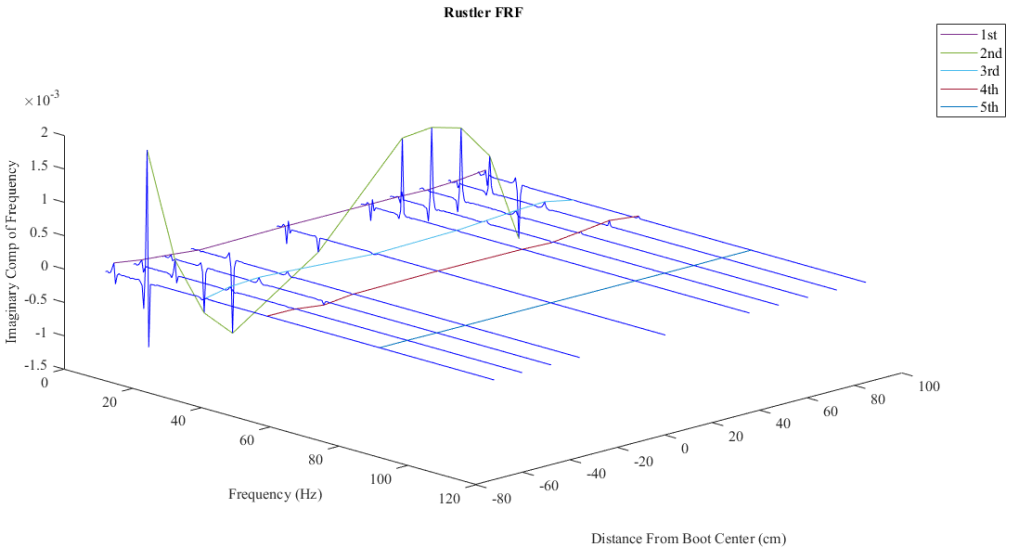

3.1.2.1 Mode Shapes

Here, I split up the post-processing of the imaginary components for two purposes, the first being a 3D visual of the measured mode shapes and the second for use in the force estimation

section. When processing the imaginary components for visuals, I normalized each mode from a range of zero to one with the purpose of making relatively small changes in magnitude much easier to see. The visual was made for cross-corelation to general modal theory presented in [38, 24], as the ski is essentially a slender beam and one should expect the mode shapes to follow the general shapes presented in theory. In Figure.3.7 it can be seen that the first three modes align with expectations of a free-free beam condition, the first mode has two nodes and every mode following that has one more node [9]. This visual can also provide insight to the slight presence of torsional motion in vertical bending modes, as mentioned in [16].

Figure 3.7: Normalized imaginary components for easier visual analysis. X: Distance Relative to Boot Center (cm), Y: Distance Relative to Center Cord (cm), Z: Unity Modal Mass

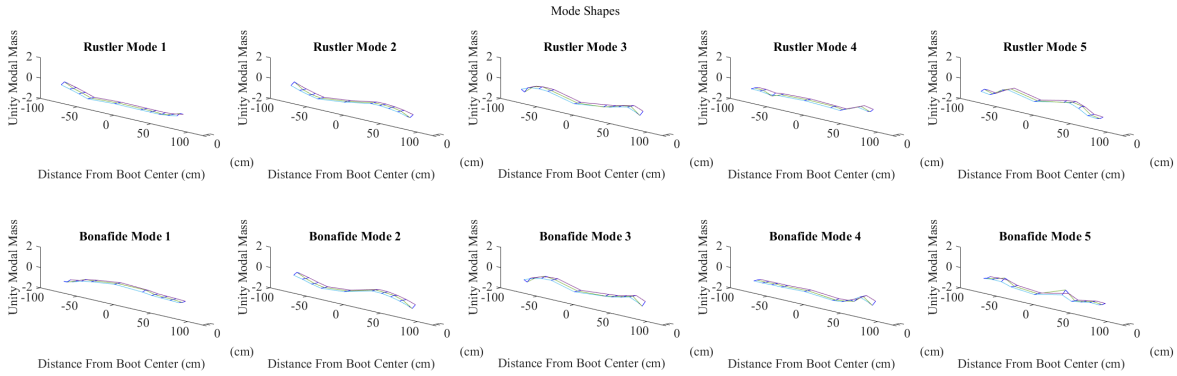

Preparing the imaginary components for use in force estimation requires finding the sign and magnitude of each imaginary component associated with each natural frequency and saving that value in a five-by-ten matrix, where the columns are the mode and the rows are the relative position. This process has to be completed for both acceleration and displacement; the resulting mode shapes can be seen in Figures.3.8,3.9, respectively.

Figure 3.8: Bending mode shape derived from the imaginary components of accelerometer-based FRF analysis. Contains a polynomial fit for visual correlation against Figure.3.7. Imaginary Component vs. Distance Relative to Boot Center (cm)

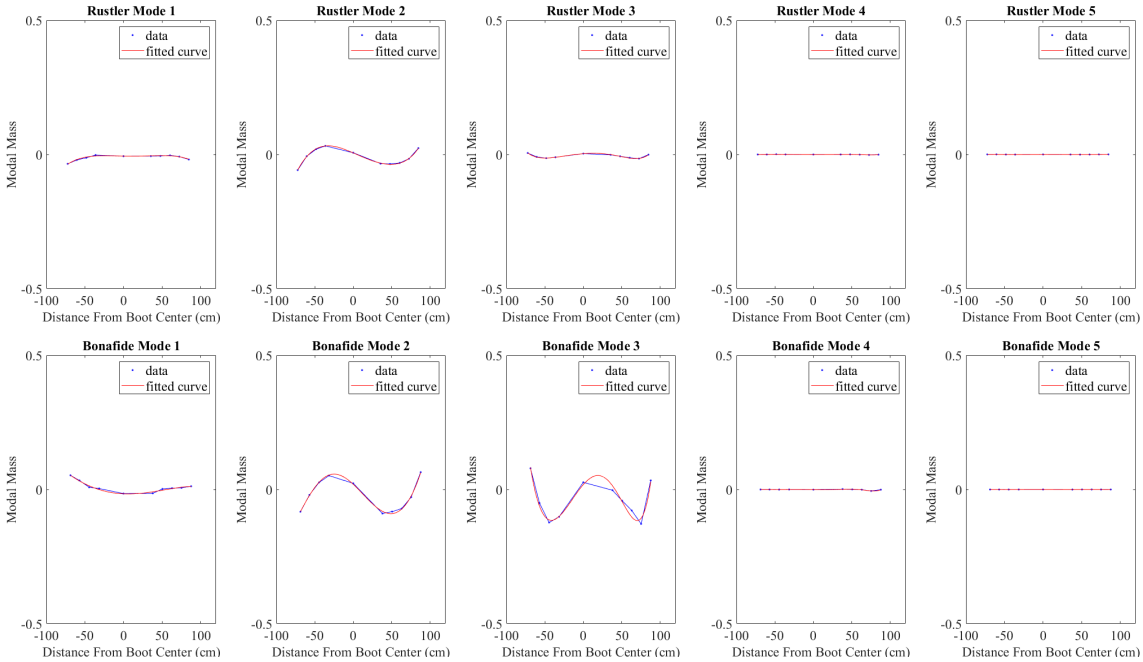

Figure 3.9: Bending mode shape derived from the imaginary components of displacement-based FRF analysis. Imaginary Component vs. Distance Relative to Boot Center (cm)

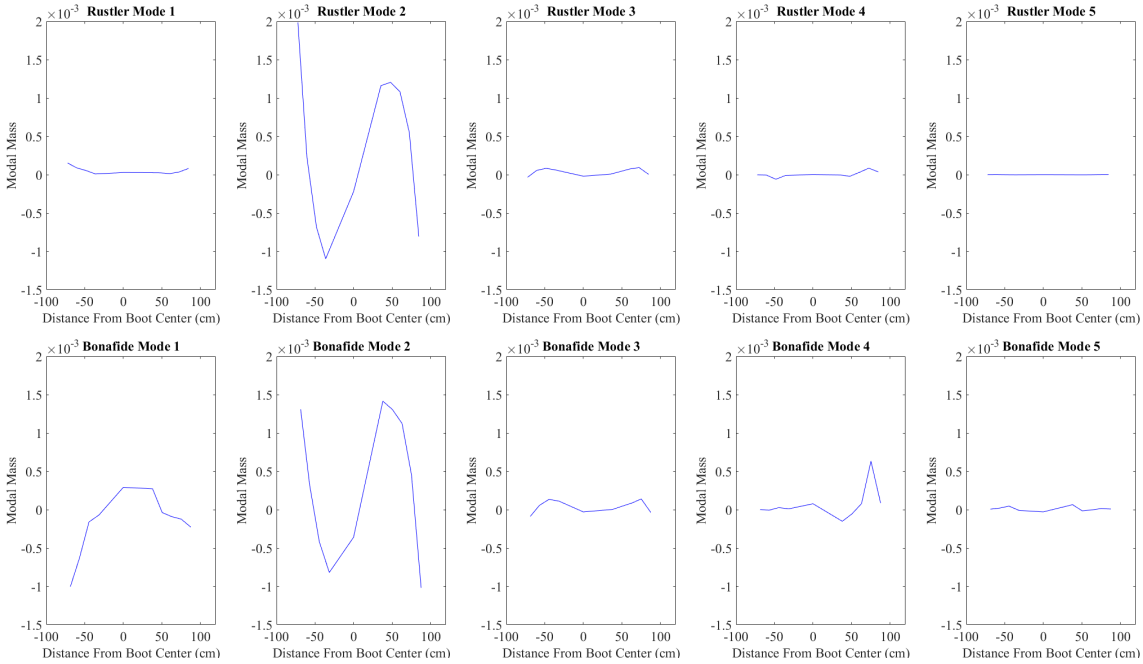

3.1.2.2 Natural Frequencies and Damping Ratios

Using the physical frequencies found in the stability diagram formation FRFs for both acceleration and displacement, the associated natural frequencies and damping ratios can be fitted. The natural frequencies and damping ratios for vertical bending from both the accelerometer-based and MOCAP-based are averaged to report the findings in Table.3.3,3.4, respectively. The reported STD is the combined error of the separate measurement methods for each mode. The results of the two types of measurement were combined because both natural frequencies and damping ratios should not change regardless of the measurement method [38, 24], and providing an average based on more measurements reduces the impact of errors.

Table 3.3: Comparison between natural frequencies (Hz) of the first 5 modes in vertical bending, including the standard deviation.

Ski	1st	2nd	3rd	4th	5th
Bonafide	9.587±0.251	19.143±0.649	35.119±0.351	55.633±1.437	78.375±1.978
Rustler 11	9.453±0.867	18.944±0.590	35.104±0.745	54.408±1.616	86.194±2.838

Table 3.4: Damping ratio (unit-less, multiply by 100 for percent of critical) of the first 5 modes in vertical bending, including the standard deviation.

Ski	1st	2nd	3rd	4th	5th
Bonafide	0.042±0.061	0.020±0.034	0.033±0.040	0.020±0.026	0.017±0.012
Rustler 11	0.051±0.075	0.020±0.026	0.034±0.021	0.021±0.028	0.016±0.018

Using the data captured with the MOCAP system and the same process presented for vertical bending, one is able to find the natural frequencies and damping ratios of the torsional modes of each ski. The primary difference between the vertical bending and torsional analysis is the data fed into the FRF fit, using Eq.3.1 the conversion of relative vertical position is converted into a change in rotational position in radians. z_1, z_3 is the vertical position of the two outer markers as seen in Figure.2.7, each marker is 0.09 meters apart, ϕ_i is the roll about the center axis.

$$\phi_i = tan^{-1}(\frac{z_1 - z_3}{0.09}) \tag{3.1}$$

Table 3.5: Comparison between natural frequencies (Hz) of the first 5 modes in torsion, including the standard deviation.

Ski	1st	2nd	3rd	4th	5th
Bonafide	5.144±0.136	17.586±0.485	28.118±0.207	40.196±0.412	49.101±0.252
Rustler 11	5.220±0.065	18.123±0.727	34.836±0.453	40.356±0.536	55.116±0.793

Table 3.6: Damping ratio (unit-less, multiply by 100 for percent of critical) of the first 5 modes in torsion, including the standard deviation.

Ski	1st	2nd	3rd	4th	5th
Bonafide	0.129±0.004	0.090±0.078	0.036±0.010	0.040±0.013	0.036±0.013
Rustler 11	0.156±0.010	0.045±0.013	0.025±0.004	0.044±0.017	0.019±0.003

Further discussion will be held in 4 on the differences in results between test skis, more so on the relationship between measured natural frequencies and the measured stiffness profiles. These results will be compared to frequency content measured during field tests in the next section.

3.2 In-Field Modal Analysis

This section will present the comparison of in-field frequency analysis data and measured modal characteristics of each ski. Something to note is that laboratory testing was done with the bindings on, but all field tests included ski boot, skier, and snow contact which can cause variances in the results between laboratory and in-field testing results.

3.2.1 In-Field vs. Laboratory

In Figure.3.10 the FFT for both vertical bending and torsion are compared to the natural frequencies and their respective STD for the Bonafide, it can be seen in both cases that the most prominent frequency content typically aligns with either the first mode, second mode, or somewhere in-between which perfectly aligns with the conclusions from the laboratory modal analysis. In vertical bending there is a large amount of frequency content at multiple IMU stations near the third and fourth mode; the third mode was a major point of energy release in the laboratory tests, but the fourth mode was nearly insignificant. This misalignment could be explained by the phenomena like a skidding turn, as [16] mentioned large amounts of frequency content occurring near 60 Hz (close to the fourth mode in my testing) in their testing; as a skidding turn is not something replicated during impact testing where an impulse hammer causes a single impulse at the center chord and another impulse does not occur until the ski is completely settled, where a

skidding turn is a rapid onset of multiple impulses applied at the edge of the ski.

In Figure.3.11 the FFT for both vertical bending and torsion are compared to the natural frequencies and their respective STD for the Rustler, where the mode that stored and released the most energy was the second mode; it can be seen that the in-field data reinforces the conclusion that most of the frequency content occurs near the second mode of vibration. As mentioned previously, any higher frequency content near the fourth or fifth mode could be explained by phenomena like a skidding turn. Another consideration for misalignments lie in the existence of modal coupling as mentioned by [16], where torsional and bending modes are highly coupled, causing an offset in measured frequency content. Modal coupling will be discussed further in the next section.

Figures.3.12,3.13 show the results of the PSD analysis, which was extremely similar to the FFT results. The main difference was the relative increase in high-frequency content. I think the PSD is better suited for comparative analysis between skis. For correlation to laboratory analysis, I think an FFT is the superior method; but, I do think it is absolutely necessary to perform PSD analysis for comparative analysis between skis as it will be the preferred method for analysis in the future. The reasoning behind continuing PSD analysis will be presented in the 4.

Figure 3.10: a) Compares an FFT of the vertical acceleration component of the Bonafide to vertical bending natural frequencies and their STD. b) Compares an FFT of the gyroscope outputs about the x-axis (roll rate)component of the Bonafide to torsional natural frequencies and their STD. Amplitude vs. Frequency (Hz)

(a) Bending

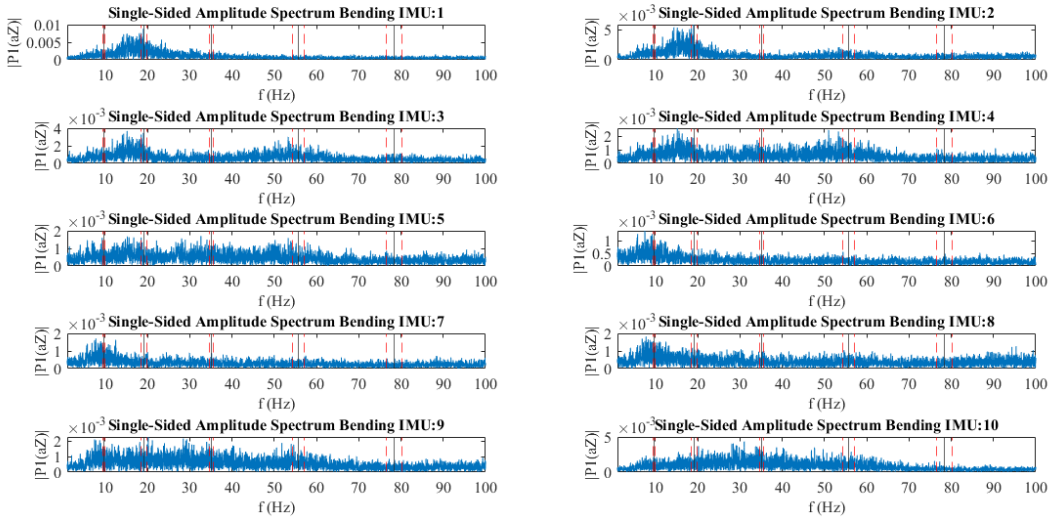

(b) Torsion

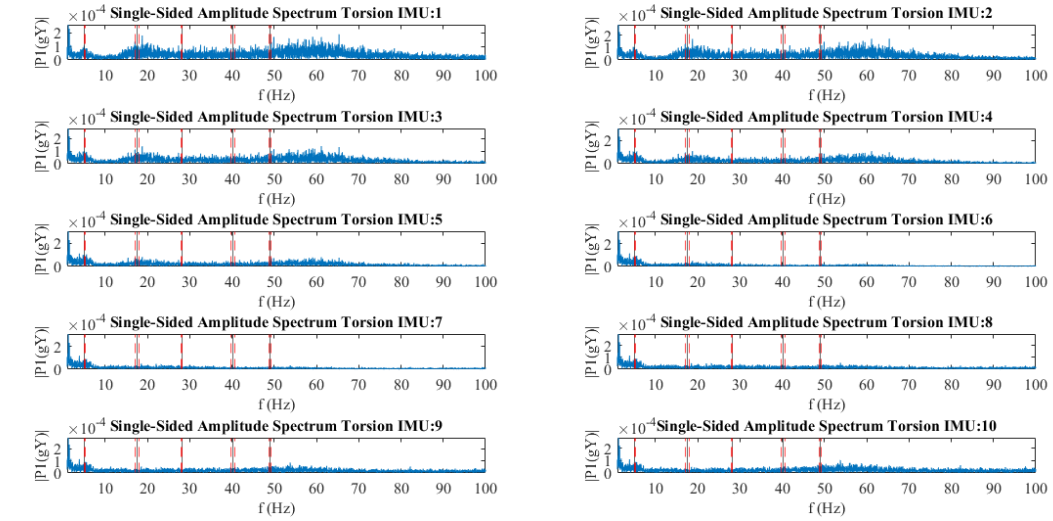

Figure 3.11: a) Compares an FFT of the vertical acceleration component of the Rustler to vertical bending natural frequencies and their STD. b) Compares an FFT of the gyroscope outputs about the x-axis (roll rate)component of the Rustler to torsional natural frequencies and their STD. Amplitude vs. Frequency (Hz)

(a) Bending

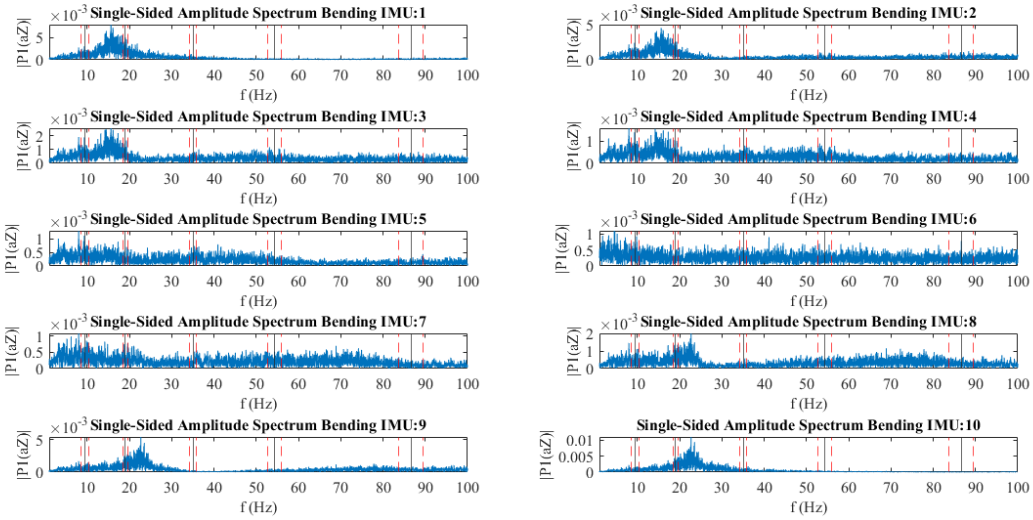

(b) Torsion

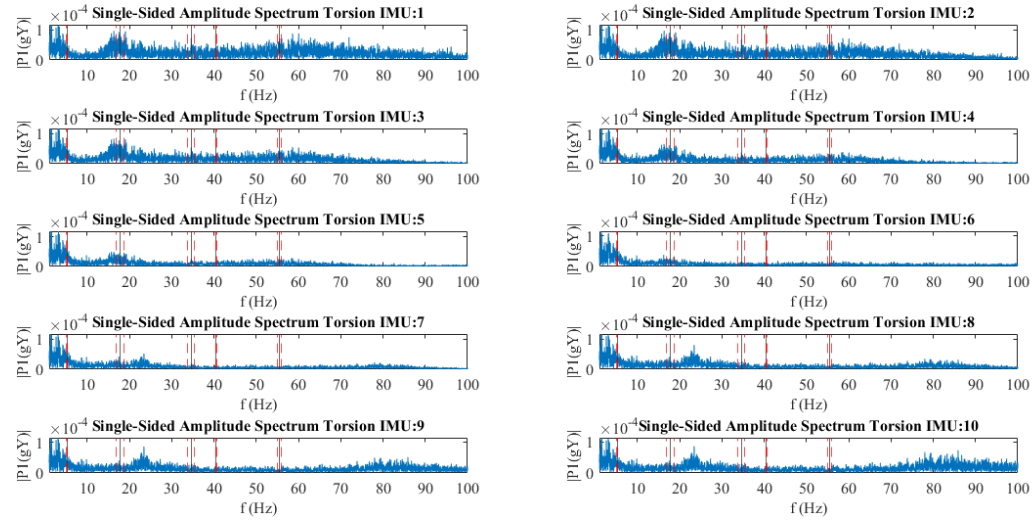

Figure 3.12: a) Compares an PSD of the vertical acceleration component of the Bonafide to vertical bending natural frequencies and their STD. b) Compares an PSD of the gyroscope outputs about the x-axis (roll rate)component of the Bonafide to torsional natural frequencies and their STD. Power (dB) vs. Frequency (Hz)

(a) Bending

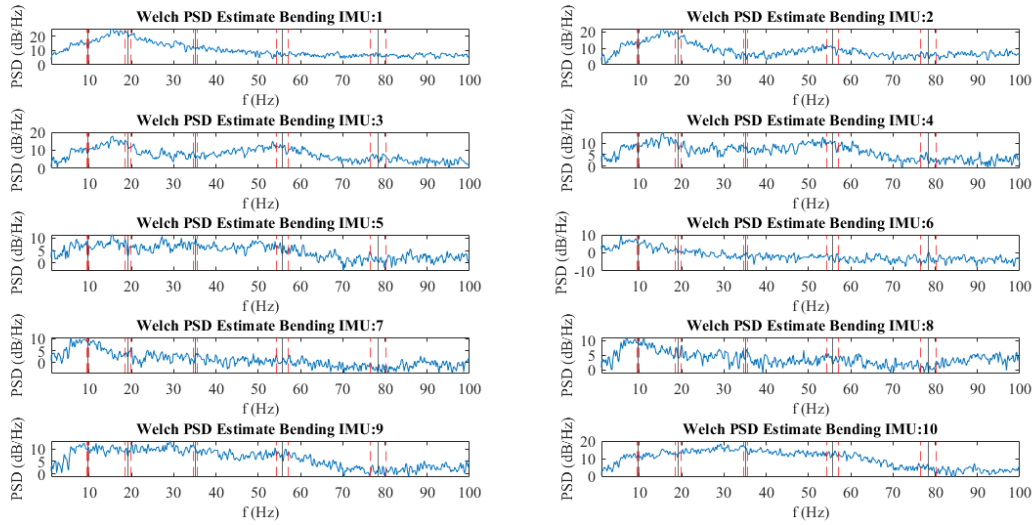

(b) Torsion

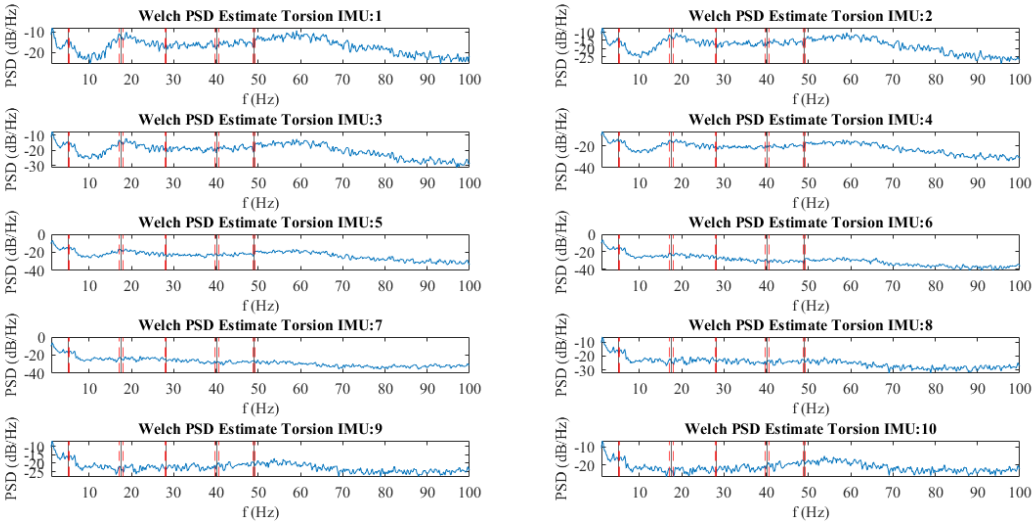

Figure 3.13: a) Compares an PSD of the vertical acceleration component of the Rustler to vertical bending natural frequencies and their STD. b) Compares an PSD of the gyroscope outputs about the x-axis (roll rate)component of the Rustler to torsional natural frequencies and their STD. Power (dB) vs. Frequency (Hz)

(a) Bending

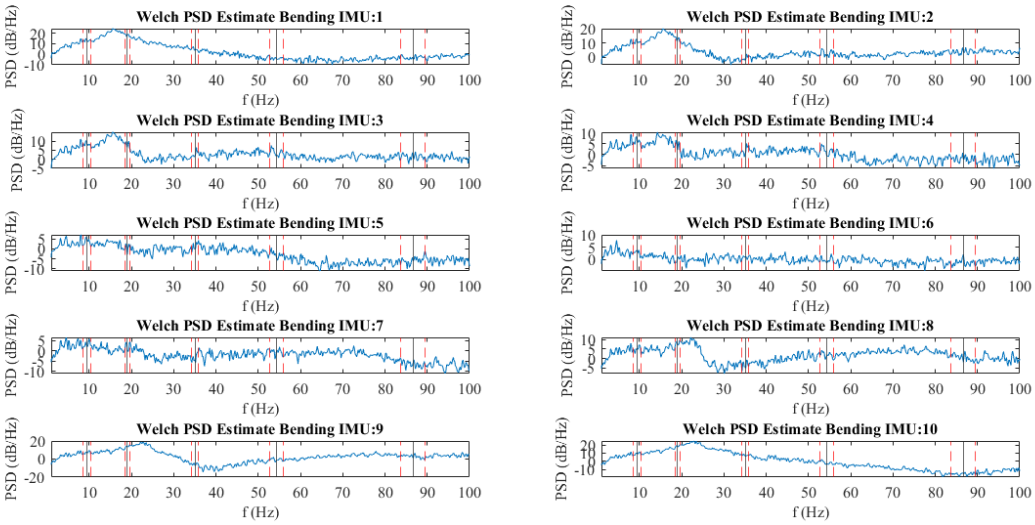

(b) Torsion

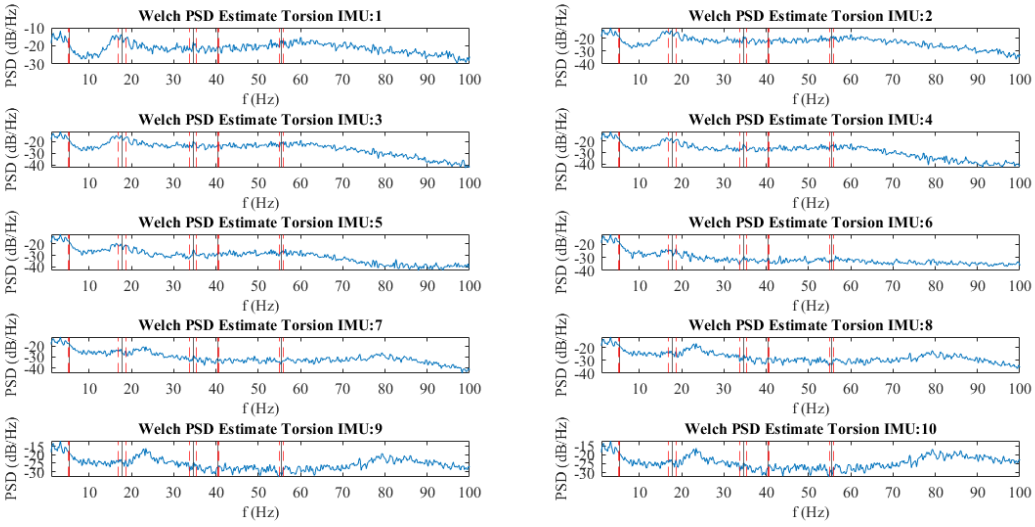

3.2.2 Modal Coupling

As mentioned previously, modal coupling between multiple bending modes, torsional modes, or between bending and torsional modes is a known phenomenon [16]. Looking at Figure.3.14 you can see what high amounts of modal coupling looks like when referencing the magnitude of an FRF. Modal coupling is a phenomenon in which separate modes affect each other (share and dissipate anergy across multiple modes) [38, 16], in an ideal situation, modes are in complete isolation and are not dependent on each other; but in a complex structure similar to an alpine ski, almost all modes are highly likely to be dependent on each other [16]. Looking at Figures.3.15,3.16 and taking into consideration that we measured relatively low damping in vertical bending, most of the peaks associated with the measured natural frequencies show characteristics that would indicate the presence of modal coupling. This is presented as a possible explanation for variances between in-field and laboratory modal testing results, but it is not the only possible explanation. Measurement error, fit error, nonlinearities, and external factors (ski boots, skier, and snow) could also impact results. Further testing would be required to pinpoint the reason behind the variances between field- and laboratory-based results, but modal coupling is something that has been found to impact results, in reference to alpine skis, in other studies before [16].

Figure 3.14: Shows the difference between low and high coupling/damping when looking at the magnitude of FRFs

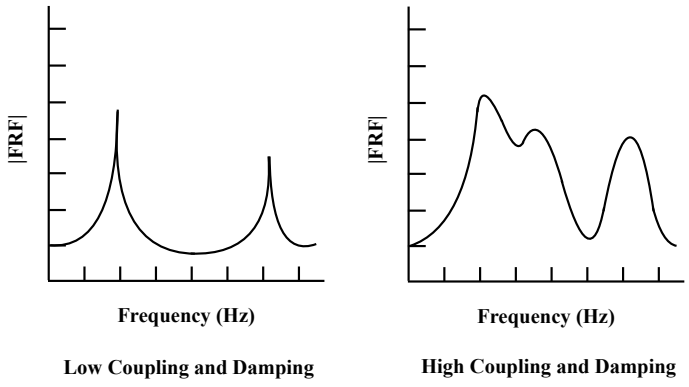

Figure 3.15: The FRF magnitude for the Bonafide of all measurement locations from lab testing. Magnitude (dB) vs. Frequency (Hz)

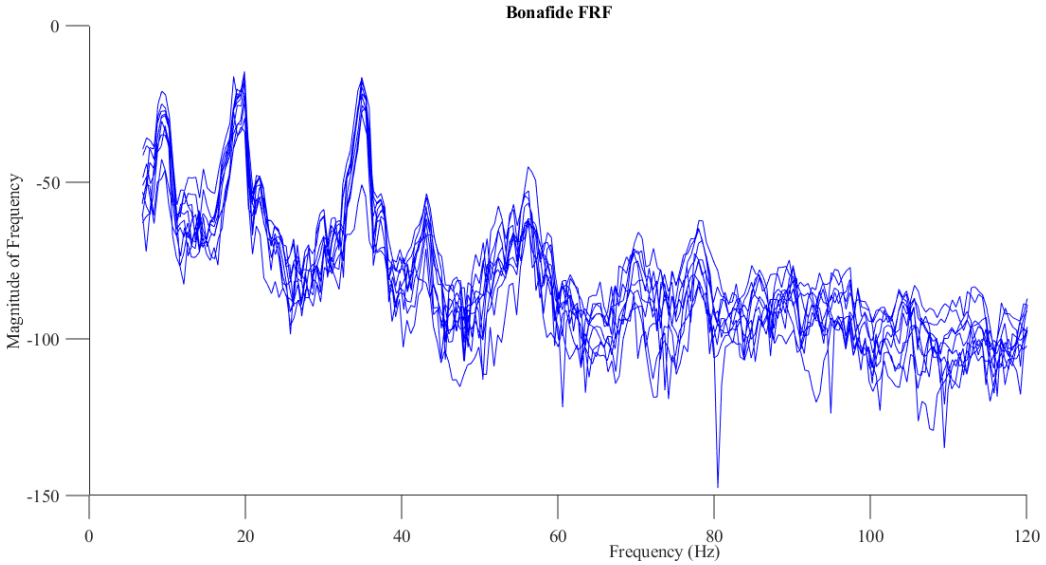

Figure 3.16: The FRF magnitude for the Rustler of all measurement locations from lab testing. Magnitude (dB) vs. Frequency (Hz)

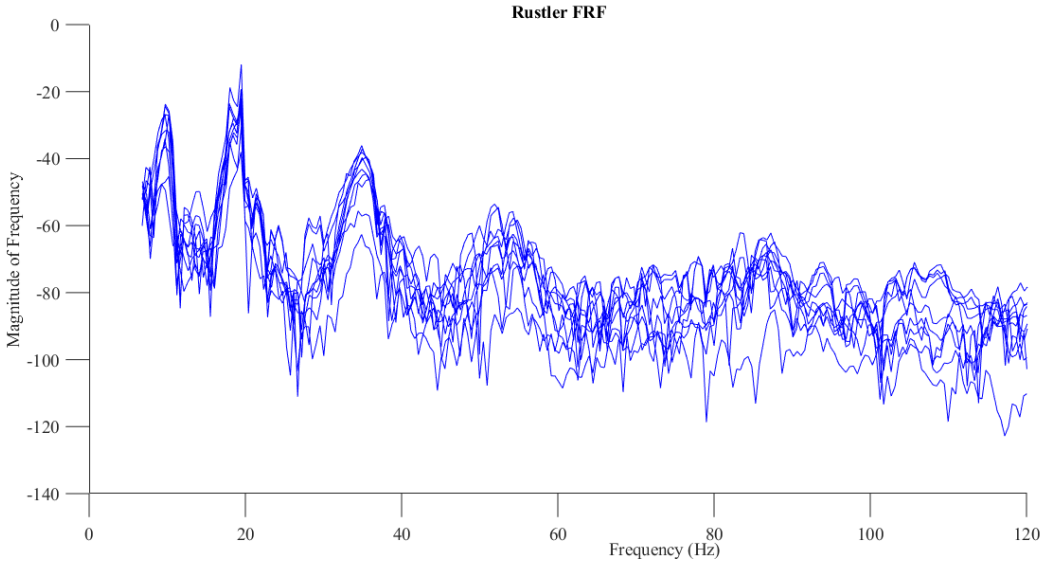

3.3 Stiffness, Displacement, and Force Estimation

This section will present bending and torsional stiffness measurements and how they align with findings in modal analysis, the results from laboratory-based validation testing for displacement estimates, the misalignment with in-field displacement estimates, and the laboratory-based force estimation testing.

3.3.1 Bending and Torsional Stiffness Measurements

In Figure.3.17 the bending and torsional stiffness profiles are presented in reference to the boot center of each ski. The main takeaway is the Rustler is generally stiffer than the Bonafide in vertical bending; this aligns with two main findings in the modal analysis testing. One being that the Rustler stored and released less energy via vibrational modes, this typically means that the ski takes more energy to move or flex [24]. The other being the fact that the fifth mode of the Rustler occurred at a higher frequency than the Bonafide (all other modes occurred within one to two Hz of each other), which would align with the physical phenomenon where a beam will vibrate at a higher frequency if it is stiffer than a beam of comparable length. When referencing the torsional rigidity the Bonafide and Rustler have a comparable average stiffness, but the Bonafide had a higher average damping ratio in torsion than the Rustler. Taking those two things into consideration could explain why peak frequencies found during in-field test occur in similar ranges but the Bonafide exhibits much less prominent peaks and frequency content that was much more distributed. The Rustler did exhibit higher average natural frequencies in torsion than the Bonafide, which could be explained by modal coupling, the stiffer center section when compared to the Bonafide, or possible measurement errors. When referencing other sources for ski stiffness profiling a company known as "Soothski" has published stiffness profiles for skis without bindings present, they found a lower average stiffness for both profiles in bending and torsion, and they found the Rustler to be stiffer than the Bonafide across the board. Variance between their results an mine, specifically for in vertical bending, occur right where the bindings were mounted on the ski in my testing. Bindings

have been found to impact the overall stiffness and dynamics of a ski in other work, [12, 14]. The variance in torsion could also be explained by the presence of bindings, but there are no local indicators similar to the vertical bending profiles; the variance could also be explained by differences in testing methods. Further testing would be required to pinpoint the exact impact bindings have on both the vertical bending and torsional stiffness of skis.

Figure 3.17: a) Bending stiffness profiles; Red: Bonafide, Blue: Rustler b) Torsional stiffness profiles; Red: Bonafide, Blue: Rustler. Stiffness (Nm^2) vs. Position Relative to Boot Center (m)

(a) Bending

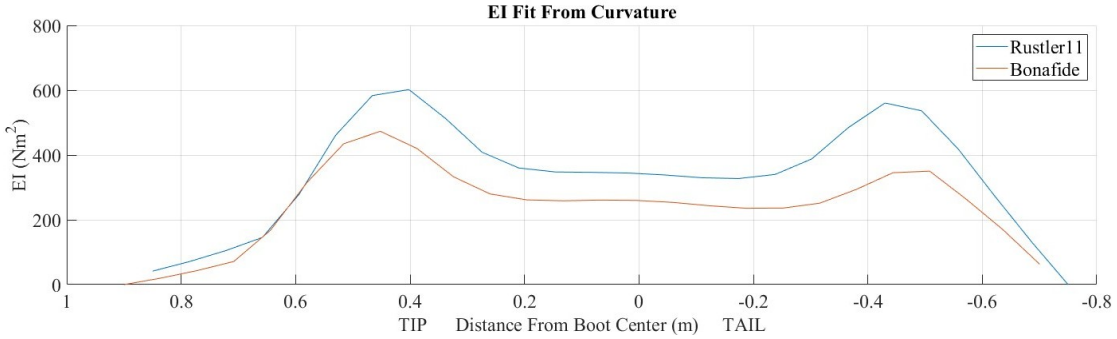

(b) Torsion

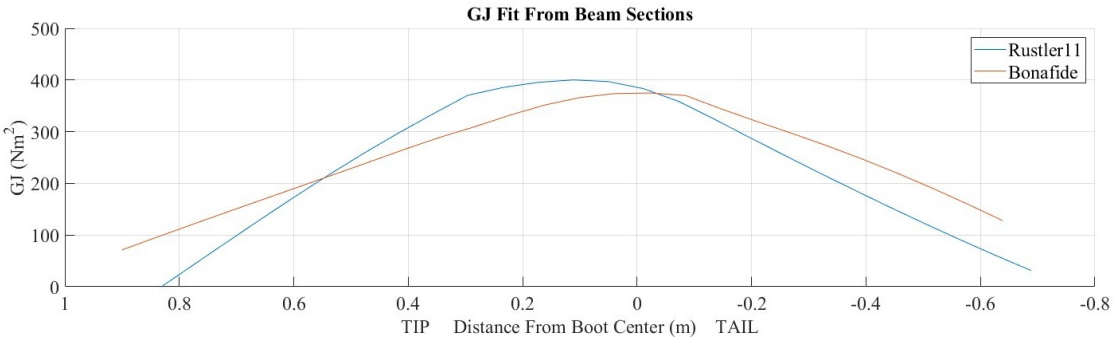

3.3.2 Displacement Estimation

The displacement estimates in lab were very promising, there was a very low error found comparing the estimated displacement and the ground-truth collected via MOCAP. A mean root mean squared error (RMSE) across all trials including both skis of 0.0012 m was found, this error accounts for all four IMU stations measured by ground-truth across 60 instances of perturbation.

A worst-case percent error of 3-4% was found in one of the trials. Looking at Figure.3.19 it shows one total trial with ten perturbations for each test ski, it can be seen that the estimate does a good job estimating the magnitude and maintaining phase with the ground-truth data; it is interesting to see that the displacement estimate was always slightly higher than ground-truth. A major thing to note about laboratory testing was all tests were done with the ski stationary and clamped at the boot center to create a cantilever beam scenario similar to the assumption made to form the math behind the displacement error process.

Figure 3.18: A spinet of displacement estimation from in-field testing. a) Showing an instance of "poor" estimation from a trial with the Bonafide. b) Showing an instance of "good" estimation from a trial with the Rustler.

(a) Bonafide

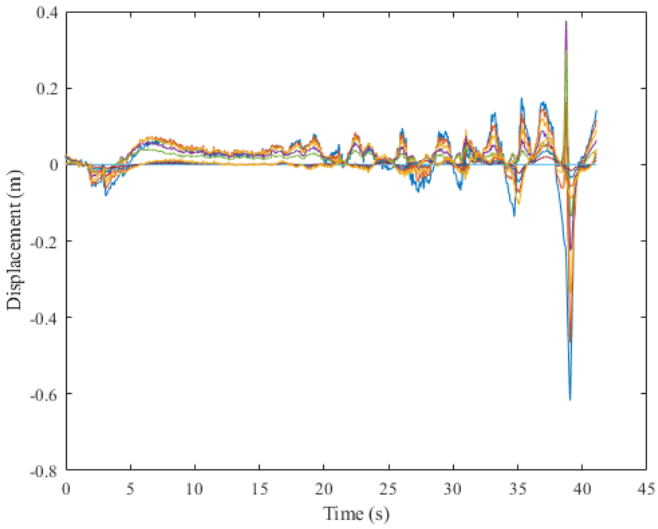

(b) Rustler

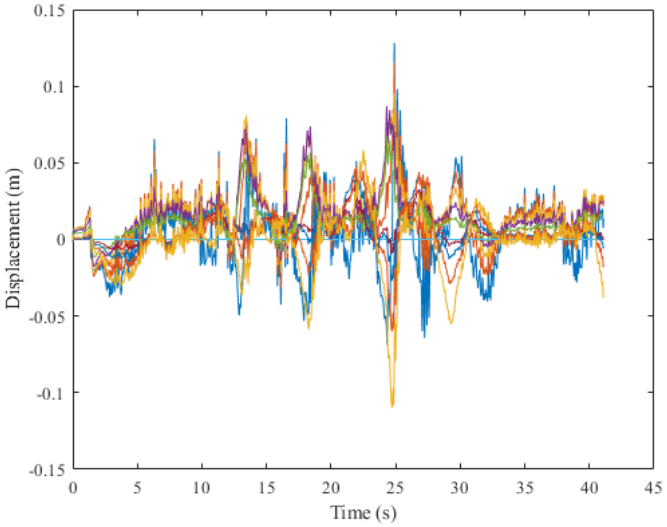

When transitioning to in-field displacement estimation, as seen in Figure.3.18, the estimation process begins to encounter limitations. The estimate is reliant on a couple things to maintain accuracy; one, the estimate for pitch of the center IMU needs to be as accurate as possible to provide a steady basis point for relative pose calculation; two, the majority of IMU estimates need

to be accurate due to the limited number available to create a fit at all time steps (if 1-2 IMUs out of 5 or 6 is off, then the fit method no longer provides an accurate estimate for the local slope of the ski); three, both the assumed deformation shape and the assumed boundary condition of a cantilever beam remains mostly true (i.e. it would be impossible for large negative displacements to occur if the ski is already contacting the snow). If a trial run is collected on a ski slope with a relatively low level of steepness and the skier maintains a less aggressive approach, most of the time these three factors remain true; but as soon as data is collected with a more aggressive skier on steeper slopes, these three factors become increasingly more difficult to maintain. Further discussion on these limitations will be had in 4.

Figure 3.19: a) One of three total trials for the Bonafide comparing ground-truth (red) to estimated displacement (blue). b) One of three total trials for the Rustler comparing ground-truth (red) to estimated displacement (blue). Displacement (m) vs. Time (s)

(a) Bonafide

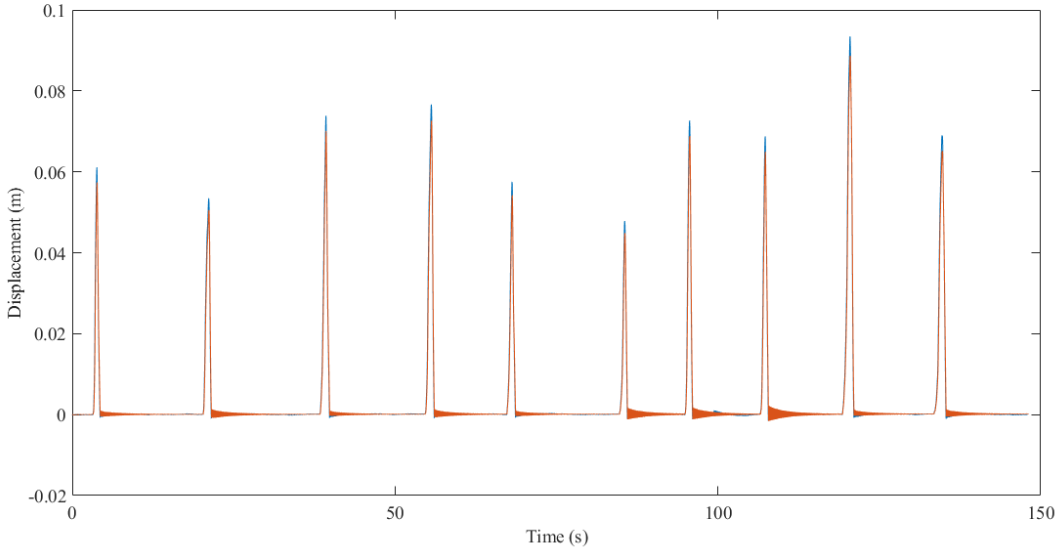

(b) Rustler

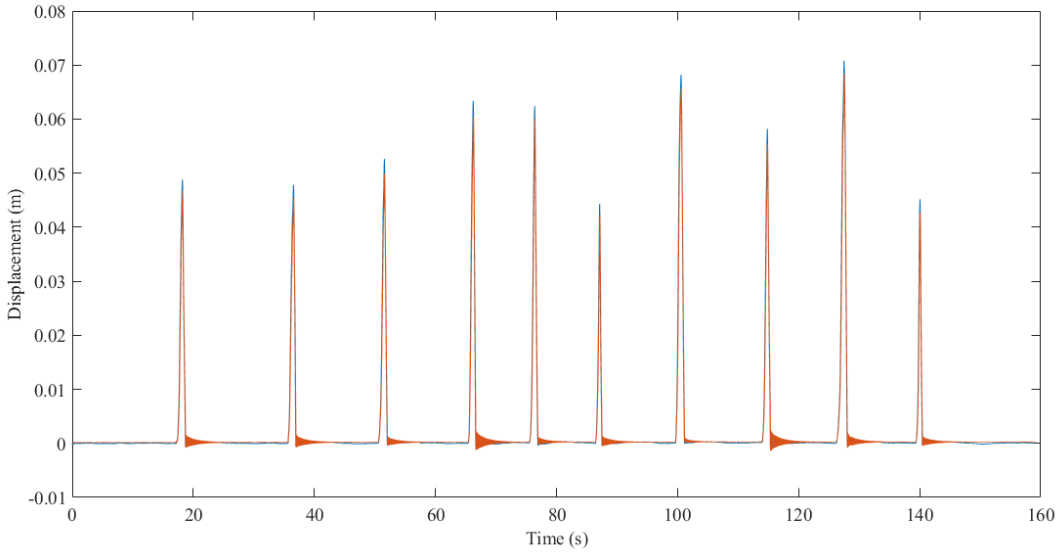

Figure 3.20: a) One of three total trials for the Bonafide estimated displacement (blue) with average RMSE bounds (red). b) One of three total trials for the Rustler estimated displacement (blue) with average RMSE bounds. Displacement (m) vs. Time (s)

(a) Bonafide

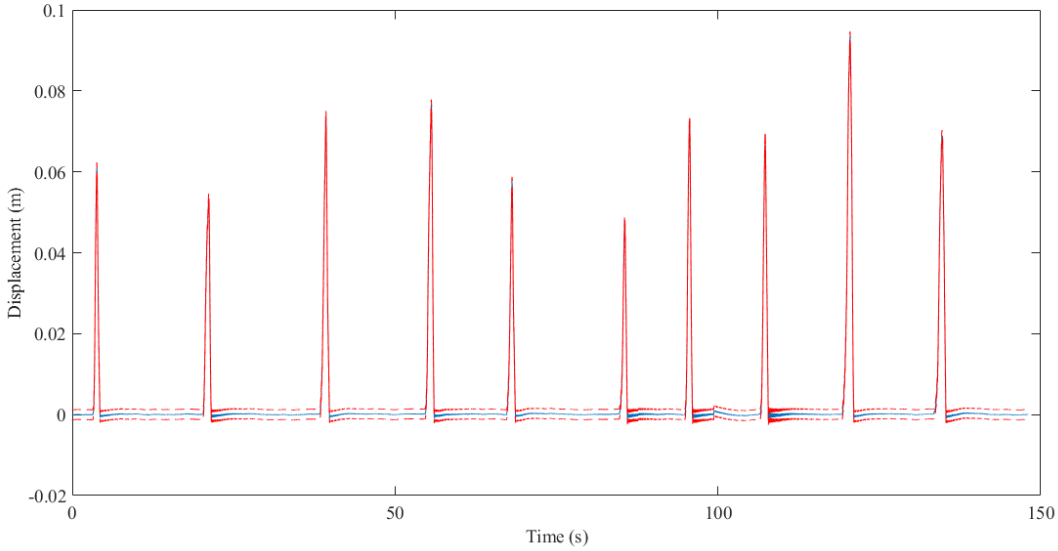

(b) Rustler

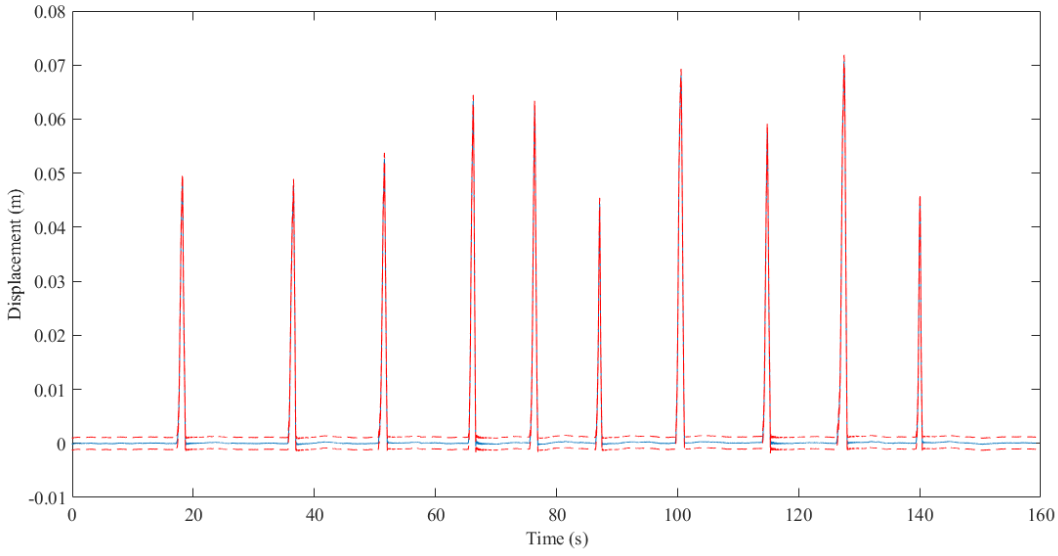

3.3.3 Force Estimation

This section will present mostly laboratory-based force estimation and testing, due to some limitation found through laboratory testing and time limitations, force-focused in-field validation testing was not performed. All three techniques presented in 2 were performed and compared to ground-truth data. The ground-truth data was the same data used in the displacement validation testing, maximum force applied was recorded using a LabVIEW VI and the load cell referenced in 2. Before even comparing force estimates with ground-truth data a trend found when comparing ground-truth displacement and force applied began to raise concerns about either the force measurement system/process or the assumption that their was a linear relationship between force applied and the displacement experienced. It is easily seen when comparing Figure.3.20 and Figure.3.22, as mentioned previously, the predominant component of force is caused by the stiffness of the ski which has been assumed to have a linear relationship to displacement, and it can be seen when comparing figures that with higher displacement comes a higher force estimate and vice versa; but when looking at the force ground truth data in comparison to the estimates, it no longer follows that trend.

The two best methods, resulting in very similar error across all testing, was the standard second-order and the direct sensor mapping method each producing a mean RMSE error of 30 newtons and 25 newtons, respectively, across all 60 perturbations. This error remained extremely consistent regardless of ski or magnitude of force, with a worst case mean RMSE of 35 newtons and 32 newtons (both occurring with the Rustler interestingly), respectively. The direct sensor mapping estimates can be seen in Figure.3.23, where scaling error bars are provided to visualize the struggle that was fitting the nondimensional hydrodynamic force estimates to ground-truth data, where the scaling error ended up being close to 45% averaging across all trials. Acceleration was not expected to have a perfectly linear relationship to force applied, but based on testing it seems to be extremely dependent on loading rate rather than just the force applied. This was not something directly tested and would require a more in-depth study to find the exact correlation between measured

acceleration and force applied. Another interesting trend to note, is that the hydrodynamic/sensor mapping force estimate does not follow the same trend as the standard second-order estimation, it does not have a direct or linear correlation to displacement and could possibly explain the slight improvement over the standard second-order system approach. The frequency domain version of a second-order system did not work consistently enough for further analysis, an example can be seen in Figure.3.21, this will be discussed further in 4.

Figure 3.21: Shows the estimated force through the frequency domain second-order approach in blue and ground-truth in black.

(a) Bonafide

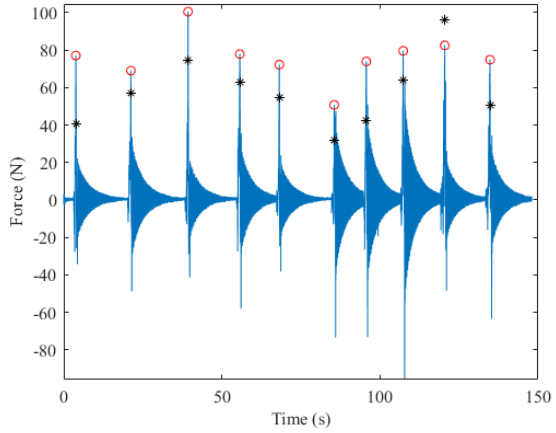

(b) Rustler

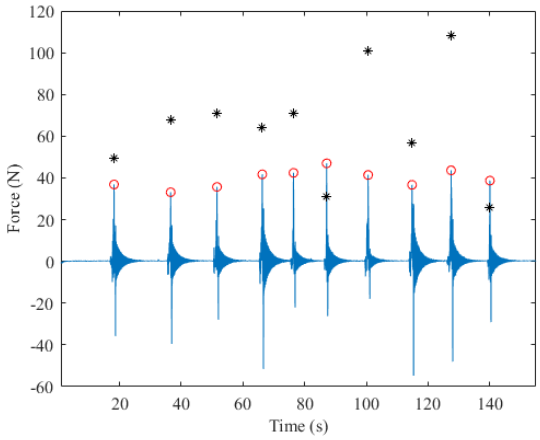

Figure 3.22: Shows the estimated force through the standard second-order approach in blue, the maximum associated with ground-truth in red, and ground-truth in black.

(a) Bonafide

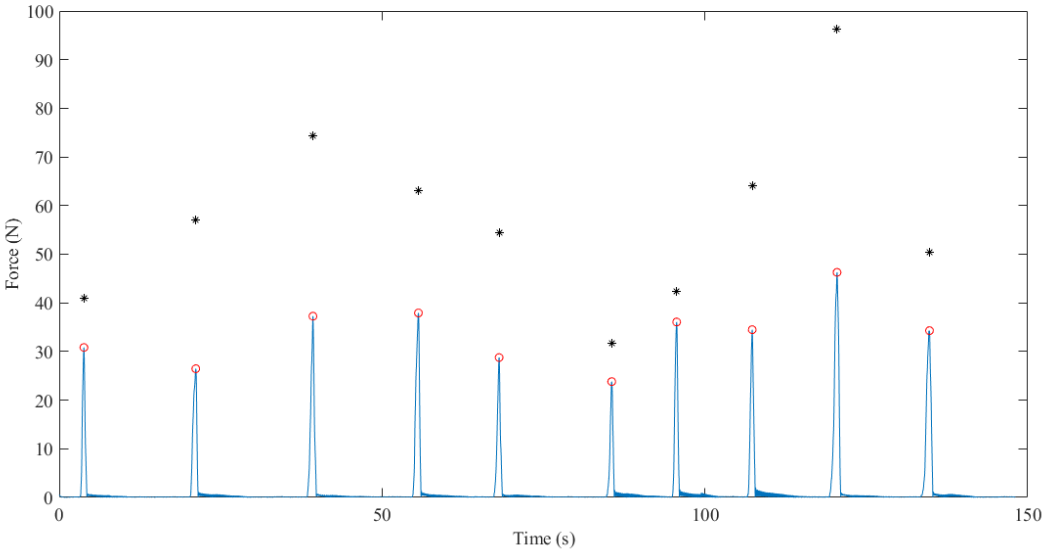

(b) Rustler

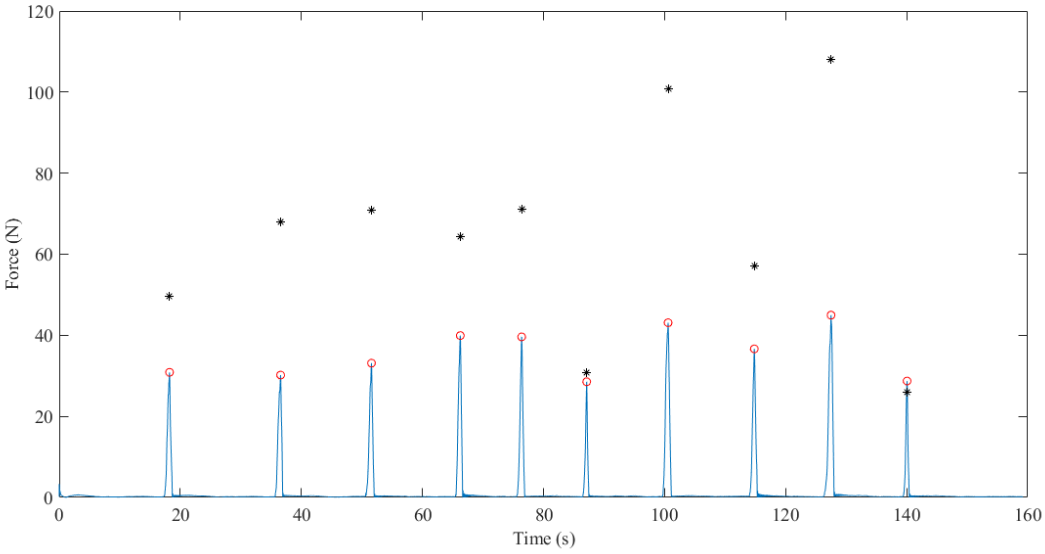

Figure 3.23: Shows the estimated force through the scaled direct sensor mapping approach in blue, the maximum associated with ground-truth and the scaled error in red, and ground-truth in black.

(a) Bonafide

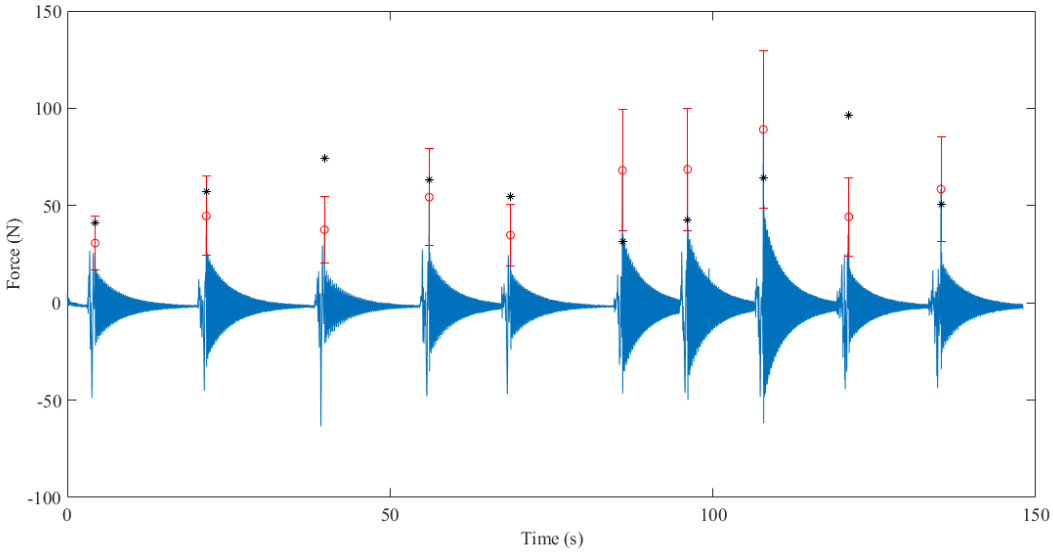

(b) Rustler

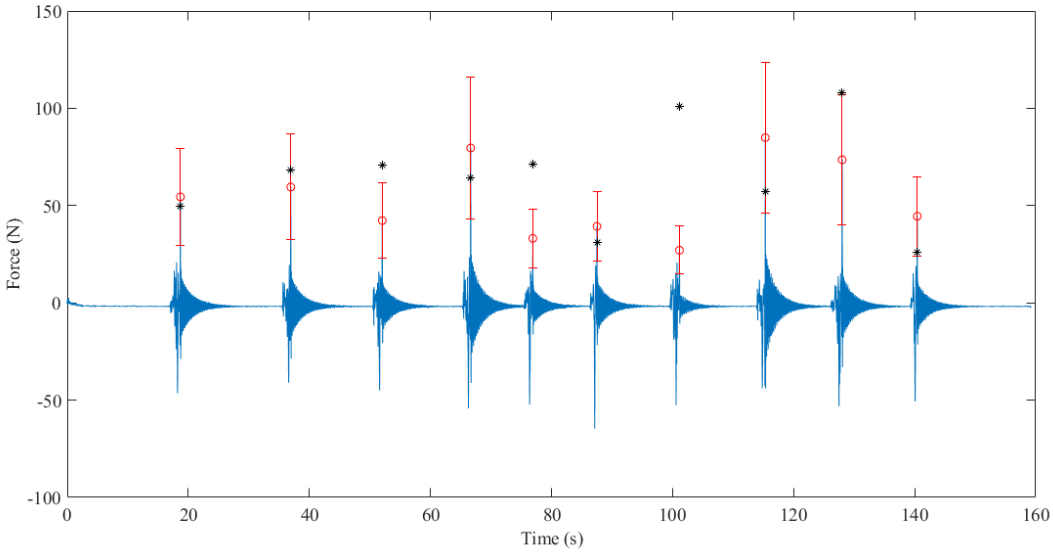

Chapter 4

Discussion

4.1 Modal Analysis

Overall, modal analysis both in the laboratory and in-field have proven to be worthwhile, for relatively low amounts of time and testing complexity one can collect quantitative information of various mechanical and dynamic properties relevant to ski performance. Relating these measured characteristics to qualitative traits will be discussed further in 5. Using the modal analysis techniques presented in this study, natural frequencies, damping ratios, mode shapes, energy storage and release characteristics, and in-lab to in-field correlations can be made. The main novel contributions of this study were the introduction of MOCAP as a viable method for measuring displacements to be used in modal analysis and a viable framework for measuring most of the necessary modal characteristics of a ski for use in future quantitative studies of alpine skis. Missing aspects would include the derivation of torsional mode shapes, a comparison of fixturing methods to find the most realistic/comparable to in-field results, more varied excitation types and magnitudes, and a larger/more diverse set of test skis for a broader dataset for future qualitative to quantitative correlations.

4.1.1 MOCAP Advantages and Disadvantages

MOCAP proved to be a very useful tool in impact modal testing, it allowed for more measurement points across the ski with a minimal increase in equipment and processing, while providing results about as accurate as the industry standard accelerometer-based impact test. It was ex-

tremely useful for the roving output test in-particular, as you can put as many output sensors as necessary virtually anywhere on the ski, allowing for a more streamlined and time-efficient test process. The typical test procedure for finding displacement mode shapes and characteristics would include strain gauges, which are notorious difficult to set up and implement correctly; MOCAP provides a viable alternative to strain gauges for displacement-based modal analysis.

MOCAP is not a perfect system for modal analysis and does include many downsides. MOCAP only allows for frequency-focused data capture of up to 120 Hz to maintain adherence to Nyquist criterion (capture rate is 240 Hz, but there are other MOCAP systems with higher capture rates), and it is limited in the minimum magnitude of displacement, as the best case error is close to 0.2 mm with proper calibration and an ideal test environment. The ski's displacement magnitude is above 1 mm past one second of data capture, making the error close to 20% in the worst case (this is near the point where the ski is near settling and would only impact measurements of higher frequency modes), as seen in 2.8. That measurement error is something that would require further more focused testing to find its exact impact on results. Another thing to note is the possible movement of the markers themselves impacting measurements, in this study the shortest marker stands were chosen to mitigate movement, every marker was checked for tightness prior to every trial, and a heavy duty double-sided tape (the same tape used in [5] for securing the in-field instrumentation system to the ski) was used to secure the markers to the ski. Marker movement magnitude would fall in a range close to the MOCAP's measurement error so the impact is most likely negligible, but it was not something that was tested and verified in this study. MOCAP also needs direct line of sight to all of the markers throughout the duration of a trial making the general test set-up more tedious than an accelerometer-based impact test. Time synchronization with the excitation signal is more difficult than a standard accelerometer-based impact test; in this study makers were placed on the hammer directly to solve this issue, but there are accessories that would allow for direct synchronization between the MOCAP system and a DAQ.

4.1.2 Modal Characteristics and Mechanical Characteristics

As mention in 3 various components of a FRF can provide insight on a systems ability to store and release energy. These components vary depending on if displacement- or acceleration-based modal analysis was performed, but in this study's testing results for both skis most prominent mode was consistent between both test types. When comparing the overall magnitude of these FRF components relates to how easy/how much energy is channeled into a system, typically a higher magnitude means it was easier to impart energy/more energy was absorbed and released. In a physical sense, it is more difficult to impart more energy into a stiffer system, which surfaced when comparing the real and imaginary component magnitude between skis. The Rustler is a stiffer ski in vertical bending; that was represented in modal testing as lower magnitudes for both imaginary and real components of each measurement points FRF. In torsion each ski had very similar average stiffness but the Bonafide had higher average damping in torsion, this surfaced in the imaginary components of the torsional FRF as a lower magnitudes, as the Bonafide released less energy via torsional modes. This can be seen in the in-field frequency analysis as distributed frequency content. In comparison you can see obvious resonant frequencies in the torsional in-field analysis for the Rustler.

After making a few correlations between the various modal and mechanical tests,it is readily apparent how this more comprehensive set of modal/mechanical data could make quantitative to qualitative correlations much easier and concrete. Modal/mechanical characteristics are things that can be represented accurately in FEA/FEM simulations and could mitigate the impact of the lack of in-situ loading scenarios; having access to those loading scenarios is still the optimal path of relating on-snow performance to simulation-based testing, but having access to accurate and comprehensive modal/mechanical characteristic data profiles can be a close second. Direct comparison and validation of correlations between quantitative characteristics and qualitative traits was not conducted extensively enough to be presented in this study, but there is promise for future endeavors.

4.1.2.1 Variations Between In-Field and Laboratory Testing

For the most part, as discussed in 3, the laboratory and in-field modal testing aligned with each other in most cases, there were a few instances where resonant frequencies or frequencies that released the most energy measured in-field did not perfectly align with either bending or torsional frequencies found in lab tests. Possible explanations for these misalignments included phenomenon like a skidding turn as explained in [16], modal coupling [16], in-lab fixturing not representing in-field scenarios accurately, and general measurement errors. Further testing would be required to explain what specific factors caused misalignment between laboratory and in-field modal testing. Suggestions for future testing will be in 5.

4.1.2.2 PSD Analysis

PSD analysis was presented in this study, but was not used as much as FFT analysis for comparison between in-field and laboratory testing as it was more difficult to pin-point resonant frequencies; but it did provide insight as to what frequency ranges released the most amount of energy, which proved useful when correlating to the real and imaginary FRF components. Where PSD testing becomes even more relevant is when comparing skis to each other for quantitative to qualitative correlations, this is due to the inherent benefit of PSD analysis results being independent of bandwidth [46]. This allows in-field tests to be conducted over varied test periods, mitigating the impact of stationary moments/unideal testing procedures. Making PSD analysis the ideal in-field frequency analysis technique for comparative purposes, such as qualitative vs. quantitative or comparing a previous season ski to a new model year ski.

4.2 Displacement and Force Estimation

Displacement estimation showed promise in laboratory testing, it proved to be very accurate when the ski is stationary and subject to isolated loads. With that in mind, I do think that this IMU-based displacement estimation framework does have merit in specific scenarios. I do think it

was novel to attempt displacement estimation with a sensor system that is not necessarily meant to measure displacement, and with some success. Pinpointing it's shortcomings will be covered in the next section. The force estimation was not as fruitful as the displacement estimation, as nothing in-lab really lined up with expectations. Two of the three methods have been used in an aerospace application with success. I do think two of the methods presented, the standard second-order and direct sensor mapping method are not that far away from being viable options, but the frequency domain second-order did not show any consistent results unlike the other two methods.

4.2.1 Displacement Estimation Shortcomings

As mentioned previously, the displacement estimates are reliant on three main factors; one, the pose estimate of the IMU directly under the boot needs to be as accurate as possible to provide a body frame origin point for relative calculations; two, the majority of IMU estimates as a whole need to be as accurate as possible, if 1-2 IMUs out of 5 (rear) or 6 (front) have inaccurate pose estimates, then the fit method using the slope of the ski can no longer provide an accurate displacement estimate; three, both the assumed deformation shape and the assumed boundary condition of a cantilever beam remains mostly true. I think changing the boundary condition constraining the displacement estimate would solve the majority of the problems encountered when shifting to in-field testing; the issue with that change stems from the inherent limitations of this sensor system. With that in mind, if displacement estimation is the main goal, then use of sensor systems specifically designed for it would be a better option, similar to the systems developed in [43, 48]. But if the capture of modally relevant content is a major goal, then the use of a sensor system with IMUs is optimal (inexpensive, robust, and easy to implement) [5, 16]. If one were to keep the current sensor system used in this study and use it for displacement estimation, the major change would have to occur with either a change in boundary conditions, or the number and quality of IMUs would need to be increased. In order to change the boundary conditions and maintain the ability to adapt estimates to all skiing scenarios would require an invasive sensor system similar to [34, 48, 12] where pressure sensors and load cells are installed into the ski. The inclusion of pressure

sensors and or load cells with the current sensor system would solve most of the shortcomings of both displacement and force estimates, but would fundamentally change the structure of the ski (either by changing the binding ski interaction or by drilling into the ski for pressure sensors) and would require a larger DAQ; these changes completely mitigate the benefits of the sensor system presented in this study: relatively inexpensive, portable/lightweight, and noninvasive. I do think the inclusion of pressure sensors and or load cells in conjunction with IMUs could be used to create a general use in-situ loading scenario for FEA simulations, but I do not think it would be all that useful in ski performance analysis using FEA for a wide range of skis. Increasing the number and quality of IMUs with the current IMU system while also distributing them across the width of the ski, rather than just having them only on the center chord, could possibly increase the accuracy of estimates in more varied situations; this is possible by mitigating the impact of 1-2 bad pose estimates via spatial averaging.

4.2.2 Force Estimation Complications

Force estimation was not as accurate as displacement estimates in laboratory testing and by proxy are not accurate at estimating in-field scenarios. The standard second order approach was extremely reliant on the accuracy of displacement estimates and required the relationship between displacement and force applied to be linear. In the validation testing for force estimation, two possible conclusions can be made; one, the method for force collection only using peak load was not a suitable method for recording and comparing force estimates to ground-truth; two, there is a possibility that force and more specifically forces applied at varying load rates do not have a linear relationship with displacement. Both can be true without invalidating the other, but testing using a method that records a continuous load and the loading was not used so I can not make a concrete conclusion as to if either are accurate. I can say that across 60 perturbations using the testing method presented in this study, the trend of a nonlinear relationship did not change. When looking at the direct sensor mapping force estimation technique it did show that the measured acceleration associated with each displacement was nonlinearly related, again supporting the idea that varied

loading rates result in nonlinear behavior. The direct sensor mapping force estimation technique did produce the best results but fails to account for specific scenarios and even if it was the best of the three presented in this study, I do not believe it was accurate enough for use without addressing a few shortcomings. The first shortcoming is that this estimate is acceleration dominant and if there is no change in position the estimate will fail to capture that force, in [20, 17, 19, 18] they mitigate this by the inclusion of strain gauges, GPS, and flight data; all of which are fused in a large KF algorithm and produces multiple nondimensional force and moment coefficients. [20, 17, 19, 18] also had access to an accurate CAD/FEM model with accurate estimates for contact surface area, distributed pressure, and distributed mass; none of which did I have access to in this study. I do think a decent attempt at simplifying the framework presented in [20, 17, 19, 18] was made, but the inclusion of more sensor systems as mentioned in the previous section is a requirement for this estimation technique to be successful. The frequency domain second-order system estimation technique did not work consistently at all, unlike the other two techniques. I think the shortcoming of this technique is that it relies entirely on either fit or calculated values, all of which have varying errors that can propagate and ruin the estimate. This estimate technique was extremely reliant on all modal parameters being estimated accurately to begin with, two least-squares fits using those modal parameters (one set calculated form measured acceleration the other from estimated displacement), and a value that had to be derived from values found via those least-squares fits; all of which resulted in an extremely inconsistent estimate in its current implementation. As this fit technique is closely related to the direct sensor mapping technique [20, 17, 19, 18] I do think that the inclusion of two more sensor types (displacement- and velocity-focused) would vastly improve both estimates.

Chapter 5

Conclusion

5.1 Future Work

5.1.1 Improvements to Laboratory Modal Testing

The main suggestion for improving laboratory-based modal testing is increasing the resolution of both the acceleration- and displacement-based tests; test locations presented in this study were chosen to match that of the in-field sensor system for correlation purposes. That process can still be achieved with an increased number of measurement locations and would provide a more comprehensive modal dataset. This change would increase the accuracy of the fit via spatial averaging, possibly increasing the accuracy of the damping coefficients in the process. An addition I would make and not necessarily a change, would be the inclusion of various fixturing methods as [3] showed quite a variance in measured modal parameters when fixturing the ski in different ways; I would specifically try to replicate a real-world situation where the ski has a binding and boot with the center of the ski pressed against something (ideally something with material properties similar to snow), similar to the fixturing presented in[14]. In combination with the different fixturing methods I would also recommend trying varied excitation types and magnitudes; the same impact hammer/impulses within a tight range was used in this study. It would be worthwhile to try impacts with higher magnitudes to see if the measured modal characteristics remain consistent, if they do not then that would support the theory that skis have a nonlinear relationship to the force applied when it occurs at a high loading rate. The use of a shaker could replicate rapid repeated impulses

experienced during a skidding turn, it would be interesting to see if the inclusion of a phenomenon similar to an on-snow experience uncovers modal characteristics not found in this study. And the last couple suggestions are specific to the use of MOCAP, if modal testing is continued using MOCAP, I would highly recommend a more robust way of syncing the MOCAP with excitation signals. Exploration into the impact of both marker movement and mean ray error on the quality of modal focused measurements would be essential to completely validating MOCAP as a viable measurement system for displacement-based modal analysis.

5.1.2 Expanded In-field Modal Testing

Now that in-field modal testing has shown correlations to laboratory modal testing and has proven its relevance in quantitative evaluation of skis both in this study and multiple other studies [16, 14], I think the expansion of in-field modal testing is the next step. Expansion in directions relevant to subjects of interest, if it remains ski focused, the collection of in-field data on the same ski with the same skier in varied snow conditions to see how different conditions affect the measurable frequency content of a ski. If the focus shifts more towards ski comparison, the collection of data on a much larger set of skis in similar snow conditions to create a database for comparative analysis would be a great next step. All of the possible directions are viable and will lead into what will be discussed in the next section.

5.1.3 Correlation Between Qualitative and Quantitative

Even without making the changes/improvements mentioned in the sections above, I think the current framework could be used for correlations between measured characteristics of a ski and on-snow traits. [12] has already completed preliminary testing for correlating ski stiffness to performance characteristics felt by skiers. There is enough mechanically revenant data available to start making connections between what design decisions lead to what characteristics felt on-snow. If the changes suggested above are completed, it will only make the data more reliable and robust, but the bones are there to start performance characterization testing. This would require a varied set

of skis, ski testers, and varied snow conditions to make qualitative evaluations of each ski in each condition; then taking those evaluations and finding consistent trends in qualitative evaluations that align with measured traits in a ski similar to the process presented in [12]. Obviously, this would require a full modal/mechanical data profile for all skis tested before correlations can be made.

5.1.4 Changes to Displacement and Force Estimation

I think for both estimations to be viable the inclusion of at least one more sensor type and more IMUs would be required, ideally two types of sensors that measure a combination of any of these four measurement types directly: displacement, velocity, force, or pressure. I think IMUs are extremely versatile and can be used in a KF-like algorithm to provide a system of prediction and correction steps with the other sensor types, but IMUS cannot be used in isolation to make accurate estimates of measurements that would otherwise be made by a more purpose-built sensor. With the inclusion of more IMUs and new sensor types, I think revisiting the methods presented in this study would be worthwhile. Aside from the estimates themselves, I would highly recommend the use of a loading system similar to a Material Testing System (MTS), where load magnitude and loading rate can be precisely controlled and continuously measured for the capture of force-based ground truth data. This would provide a concrete and comprehensive set of ground-truth data to find out if a ski maintains linear or transitions into nonlinear behavior at various loading rates. This can be used to fine-tune the assumptions made prior to developing in-field load estimation techniques.

5.2 Concluding Thoughts

In conclusion, many of the testing methods and estimation techniques have either confirmed the validity or provided a novel approach to forming a comprehensive dataset for use in the quantitative analysis of alpine skis. Using laboratory modal analysis, in-field modal analysis, and stiffness profile measurements to capture natural frequencies, damping ratios, mode shapes, energy stor-

age and release, and stiffness distribution profiles can create a complete mechanical and dynamic property profile of an alpine ski. Providing ski manufacturers and ski review companies with an all-encompassing dataset that can allow them to begin correlating measured mechanical and dynamic properties to performance characteristics without the use of in-situ loading scenarios. As measured mechanical and dynamic properties can be used to improve the accuracy of CAD models, only streamlining the implementation of in-situ loading scenarios when they are available, but in the meantime can at least begin to provide relevant insight as to which design decisions (materials, stiffness, rocker profiles, length, shape, and weight) result in certain performance characteristics on-snow.

The displacement and force estimation techniques presented in this study show promise, but all require fundamental changes to the sensor system and by proxy, the framework that incorporates that modified sensor system. The testing behind these estimation techniques did bring up an interesting finding that was not reported in other studies; most studies only subjected skis to quasi-static loading scenarios where skis typically show a linear relationship between displacement and the force applied. My testing showed the possibility of a nonlinear relationship between displacement/acceleration and the force applied as soon as loads just outside of the quasi-static range were applied. Further exploration into a skis relationship with varying loading rates should be conducted before any further attempts are made at estimating relevant in-situ loading scenarios.

Bibliography

[1] Brett R Aiello, Kathryn E Stanchak, Alison I Weber, Tanvi Deora, Simon Sponberg, and Bingni W Brunton. Spatial distribution of campaniform sensilla mechanosensors on wings: form, function, and phylogeny. Current Opinion in Insect Science, 48:8–17, 2021. NeuroScience . Special Section on Insects as food and feed (December 2021).

[2] Peter Avitabile. Experimental modal analysis. Sound & Vibration Magazine, 1997.

[3] J.E. Jorgensen B. Glenne and J.D. Chalupnik. Ski vibrations and damping. Experimental Techniques, 18:19–22, 1994.

[4] Marco Bassetti, Francesco Braghin, Francesco Castelli-Dezza, Silvia Negrini, and P Pennacchi. Sensor nodes for the dynamic assessment of alpine skis. In Topics in Modal Analysis II, Volume 6: Proceedings of the 30th IMAC, A Conference on Structural Dynamics, 2012, pages 471–479. Springer, 2012.

[5] Leopold G. Beuken, Joshua L. Priest, Travis Hainsworth, and J. Sean Humbert. Distributed imu sensors for in-field dynamic measurements on an alpine ski. Sensors, 24(6), 2024.

[6] John Borenius, Henrik Edman, Albin Lindmark, Marcus Pålsson, Thomas Abrahamsson, and Martin Fagerström. Modelling bending stiffness and vibration characteristics to enable simulation-driven ski design. In Proceedings, volume 60. MDPI, 2020.

[7] Joint Research Centre, Institute for the Protection, Security of the Citizen, and D Tirelli. Modal analysis of small & medium structures by fast impact hammer testing method. Publications Office, 2011.

[8] C. Chandra. Experimental determination of mode shapes of beams by roving impact test. Materials Today: Proceedings, 46, 02 2020.

[9] Arie Elka and Izhak Bucher. Optimal electrode shaping for precise modal electromechanical filtering. Structural and Multidisciplinary Optimization, 38:627–641, 07 2009.

[10] Peter Federolf, Mirco Auer, Mathieu Fauve, Anton Lüthi, and Hansueli Rhyner. Subjective evaluation of the performance of alpine skis and correlations with mechanical ski properties. In The Engineering of Sport 6: Volume 1: Developments for Sports, pages 287–292. Springer, 2010.

[11] Peter Federolf, Markus Roos, Anton Lüthi, and Jürg Dual. Finite element simulation of the ski–snow interaction of an alpine ski in a carved turn. Sports Engineering, 12:123–133, 2010.

[12] Peter Andreas Federolf. Finite Element Simulation of a Carving Snow Ski. Doctoral thesis, ETH Zurich, 2005.

[13] International Organization for Standardization. Alpine skis – Determination of elastic properties . Standard, International Organization for Standardization, Geneva, CH, March 2013.

[14] Gary C Foss and Bard Glenne. Reducing on-snow vibrations of skis and snowboards. Sound and Vibration, 41(12):22–27, 2007.

[15] Richard J Gardiner. Dynamic Modeling for Ski Design. PhD thesis, Department of Civil Engineering, University of Utah., 1974.

[16] Philippe Gosselin, Jonas Truong, Charles Chapdelaine, Jean-Simon Guilbert, Étienne St-Pierre, Xavier Trahan, and Alexis Lussier Desbiens. Effect of edged snow contact on the vibration of alpine skis. Sports Engineering, 24:1–13, 2021.

[17] Jared Grauer. Method for real-time state estimation of structural modes for an aeroelastic wind tunnel model. In Parameter Identification and Aerodynamic Prediction Methods Conference, 01 2021.

[18] Jared A. Grauer and Matthew Boucher. Aeroelastic modeling of x-56a stiff-wing configuration flight test data. In AIAA Atmospheric Flight Mechanics Conference, 2017.

[19] Jared A Grauer and Matthew J Boucher. Output measurement equations for flexible aircraft flight dynamics. Technical report, NASA, 2018.

[20] Jared A. Grauer and Matthew J. Boucher. Real-time parameter estimation for flexible aircraft. In 2018 Atmospheric Flight Mechanics Conference, 2018.

[21] MEMS Industry Group. Open-source-sensor-fusion. `https://github.com/memsindustrygroup/Open-Source-Sensor-Fusion`, 2015.

[22] Dieter Heinrich, Martin Mössner, Peter Kaps, and Werner Nachbauer. Calculation of the contact pressure between ski and snow during a carved turn in alpine skiing. Scandinavian journal of medicine & science in sports, 20:485–92, 07 2009.

[23] IBISWorld. Ski & snowboard resorts in the us - market size (2003–2029). Graph, IBISWorld, New York, USA, Aug 2023.

[24] BRÜEL & KJÆR. STRUCTURAL TESTING PARTS ONE & TWO. BRÜEL & KJÆR, 1988.

[25] Manon Kok, Jeroen Hol, and Thomas Schön. Using inertial sensors for position and orientation estimation. Foundation and Trends of Signal Processing, 11, 04 2017.

[26] Teemu Lemmettylä, Teemu Heikkinen, Olli Ohtonen, Stefan Lindinger, and Vesa Linnamo. The development and precision of a custom-made skitester. Frontiers in Mechanical Engineering, 7:661947, 2021.

[27] Anton Lüthi, Peter Federolf, Mathieu Fauve, and Hansueli Rhyner. Effect of bindings and plates on ski mechanical properties and carving performance. In The Engineering of Sport 6: Volume 1: Developments for Sports, pages 299–304. Springer, 2006.

[28] Florian McLelland and Floris van Breugel. A method for classifying snow using ski-mounted strain sensors. arXiv preprint arXiv:2304.14307, 2023.

[29] Martin Mössner, Dieter Heinrich, Kurt Schindelwig, Peter Kaps, H. Schretter, and Werner Nachbauer. Modeling the ski-snow contact in skiing turns using a hypoplastic vs an elastic force-penetration relation. Scandinavian journal of medicine & science in sports, 24:577–585, 01 2013.

[30] Emerson NI LabVIEW. Sound and Vibration Toolkit. Austin, Texas, United States, 2024.

[31] Mechanics of Materials Notes Purdue Mechanical Engineering. 17. an introduction to the finite element method. Online PDF of notes for Purdue ME323.

[32] Blister Review and DPS Skis. The design & development of the new dps carbon pisteworks 79. website, 2024. Gear:30 Episode 326.

[33] Bob Rice, Rand Alan Decker, and Richard W. Shorthill. 606 modal analysis : A dynamic ski test. 2012.

[34] Nathan Scott, Takeshi Yoneyama, Hiroyuki Kagawa, and Kazutaka Osada. Measurement of ski snow-pressure profiles. Sports Engineering, 10:145–156, 2007.

[35] R.W. Shorthill, R.A. Decker, and B. Rice. Modal analysis of segmented, laminated, anisotropic, inhomogeneous beams. In 1996 IEEE Aerospace Applications Conference. Proceedings, volume 4, pages 231–240 vol.4, 1996.

[36] Matej Supej. Vibrations in recreational alpine skiing: a pilot study. In ISBS-Conference Proceedings Archive, 2013.

[37] A. Luthi H. Rhyner T. Theile, D. Szabo and M. Schneebeli. Mechanics of the ski–snow contact. In Tribology Letters, volume 36, page 223–231, 2009.

[38] Agilent Technologies. The Fundamentals of Modal Testing. Agilent Technologies, 1997.

[39] Inc. The MathWorks. Navigation Toolbox. Natick, Massachusetts, United States, 2023.

[40] Inc. The MathWorks. Modal Analysis of a Simulated System and a Wind Turbine Blade. Natick, Massachusetts, United States, 2024.

[41] Inc. The MathWorks. Signal Processing Toolbox. Natick, Massachusetts, United States, 2024.

[42] Inc. The MathWorks. System Identification Toolbox. Natick, Massachusetts, United States, 2024.

[43] Christoph Thorwartl, Josef Kröll, Andreas Tschepp, Helmut Holzer, Wolfgang Teufl, and Thomas Stöggl. Validation of a sensor-based dynamic ski deflection measurement in the lab and proof-of-concept field investigation. Sensors, 22(15):5768, 2022.

[44] Jonas Truong, Camille Brousseau, and Alexis Lussier Desbiens. A method for measuring the bending and torsional stiffness distributions of alpine skis. Procedia engineering, 147:394–400, 2016.

[45] Angella Volchko, Shane K. Mitchell, Tyler G. Scripps, Zoe Turin, and J. Sean Humbert. Robust control of electrohydraulic soft robots. Frontiers in Robotics and AI, 11, 2024.

[46] P. Welch. The use of fast fourier transform for the estimation of power spectra: A method based on time averaging over short, modified periodograms. IEEE Transactions on Audio and Electroacoustics, 15(2):70–73, 1967.

[47] Fabian Wolfsperger, Denes Szabo, and Hansueli Rhyner. Development of alpine skis using fe simulations. Procedia engineering, 147:366–371, 2016.

[48] Takeshi Yoneyama, Hiroyuki Kagawa, Daichi Tatsuno, Motoki Kitade, Kazutaka Osada, and Satoshi Shigehara. Effect of flexural stiffness distribution of a ski on the ski–snow contact pressure in a carved turn. Sports Engineering, 24, 12 2021.

Appendix A

Additional Figures and Equations

$$\begin{aligned} \eta_i &= a_i \sin(\omega_i t + \phi_i) \\ \dot{\eta}_i &= a_i \omega_i \cos(\omega_i t + \phi_i) \\ \ddot{\eta}_i &= -a_i \omega_i^2 \sin(\omega_i t + \phi_i) \end{aligned} \tag{A.1}$$

Figure A.1: Example of the slope fit function, showing it's piecewise boundary conditions. Slope vs. Position Relative to Boot Center (m)

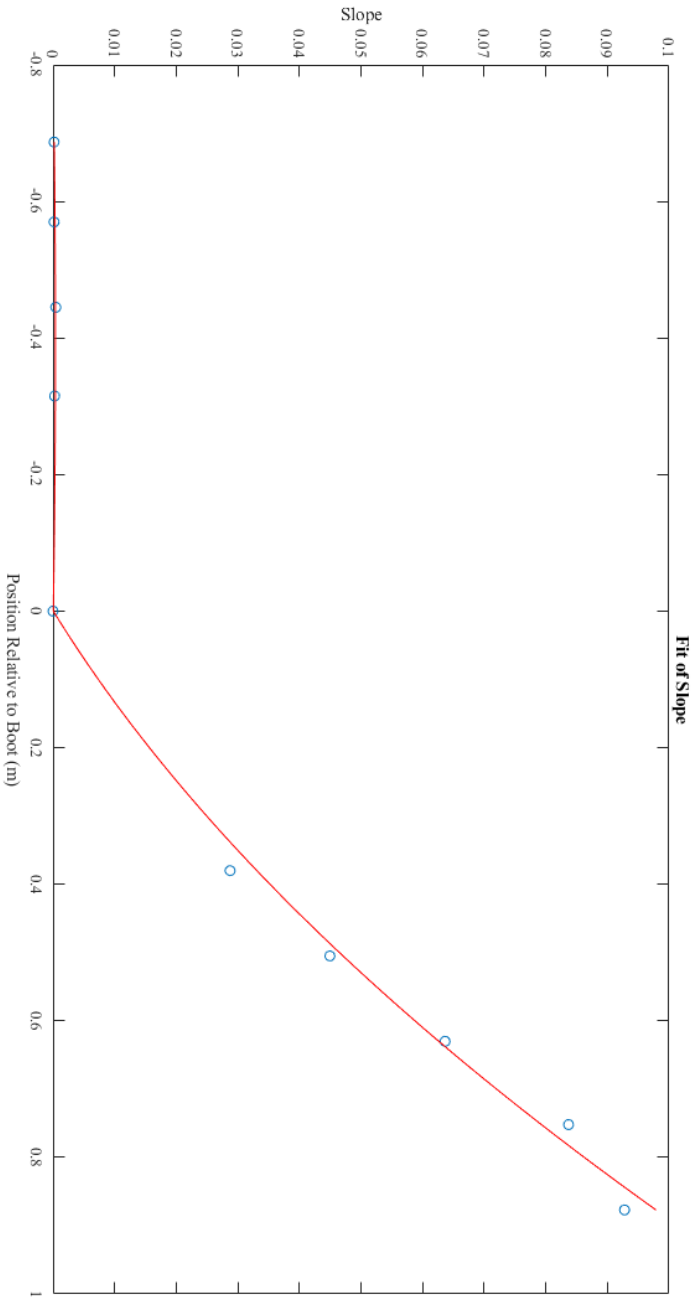

Figure A.2: Magnitude of OFRF

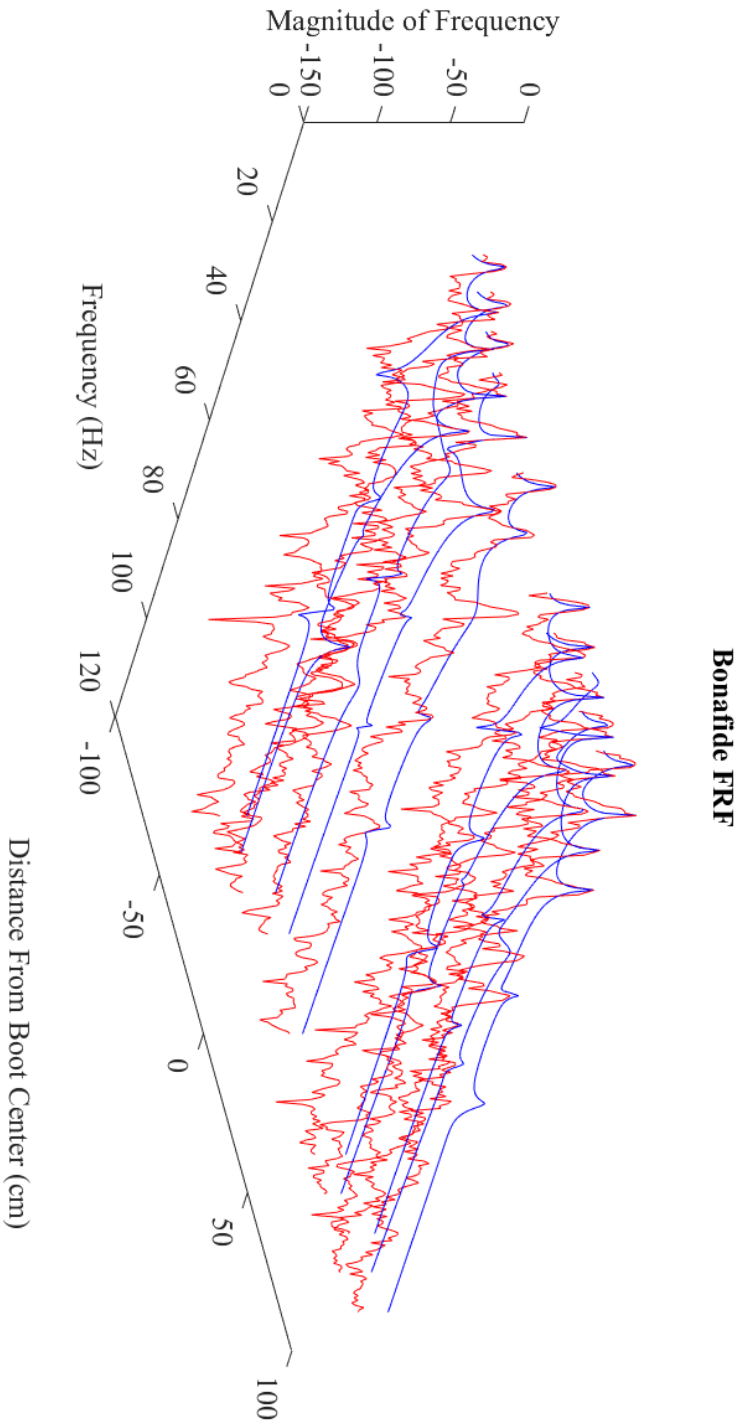

Figure A.3: Real Component of OFRF

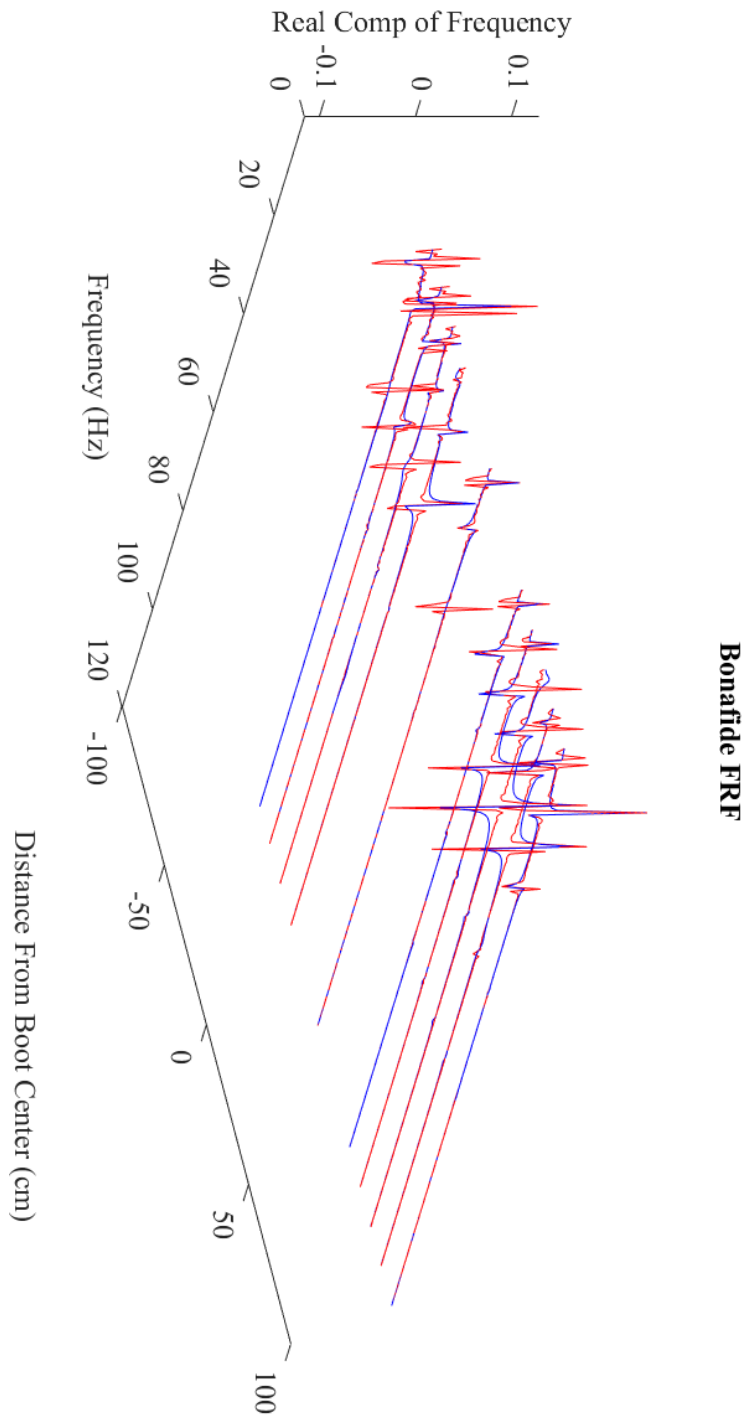

Figure A.4: Imaginary Component of OFRF

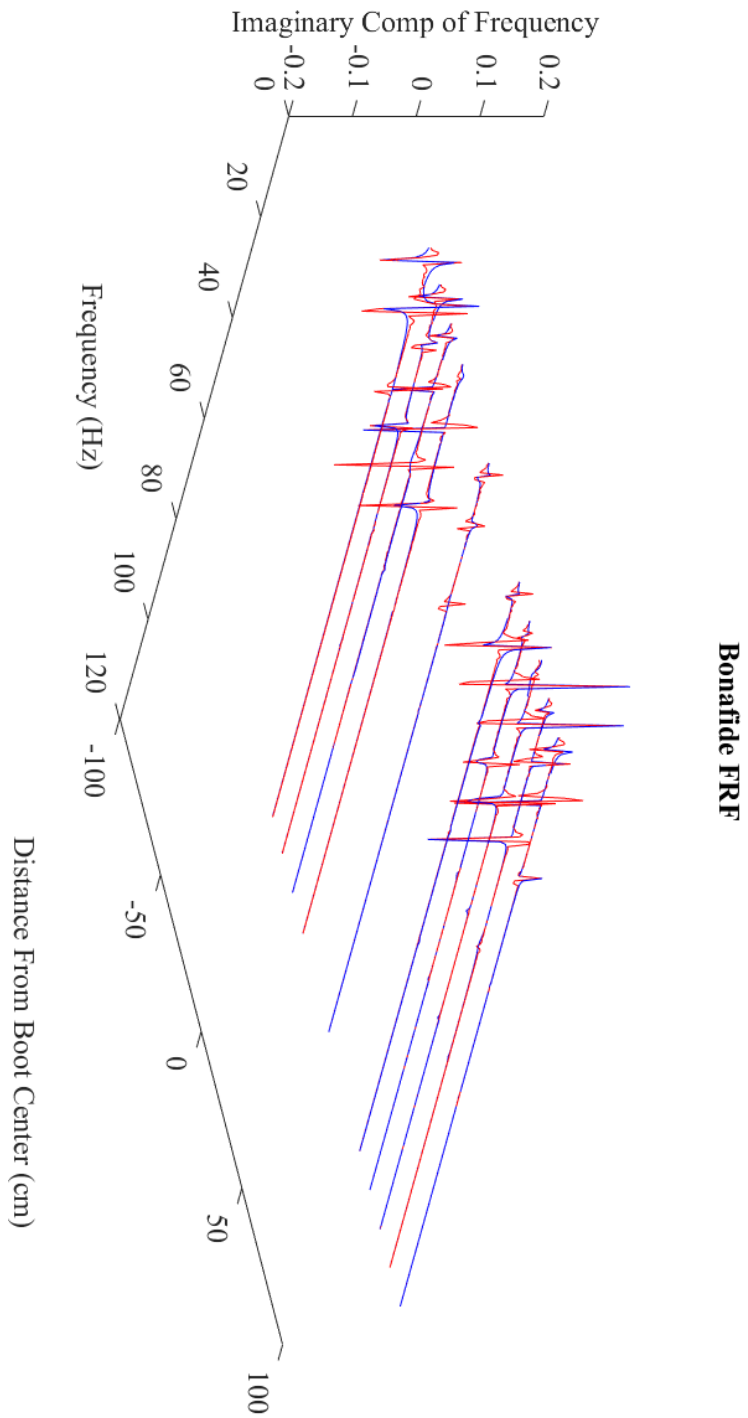

Figure A.5: Accelerometer-based stability diagrams from FRF analysis.

(a) Bonafide

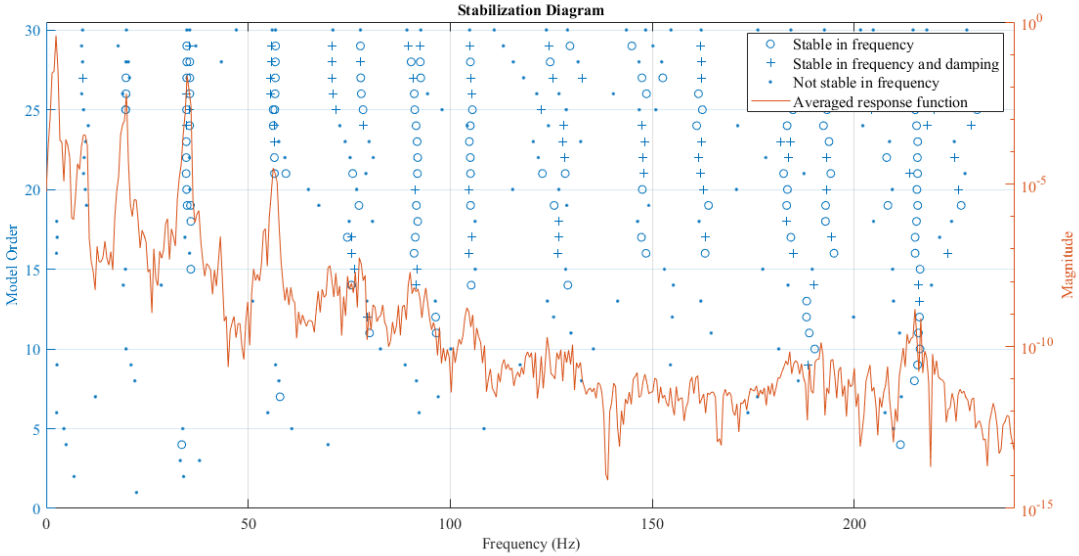

(b) Rustler

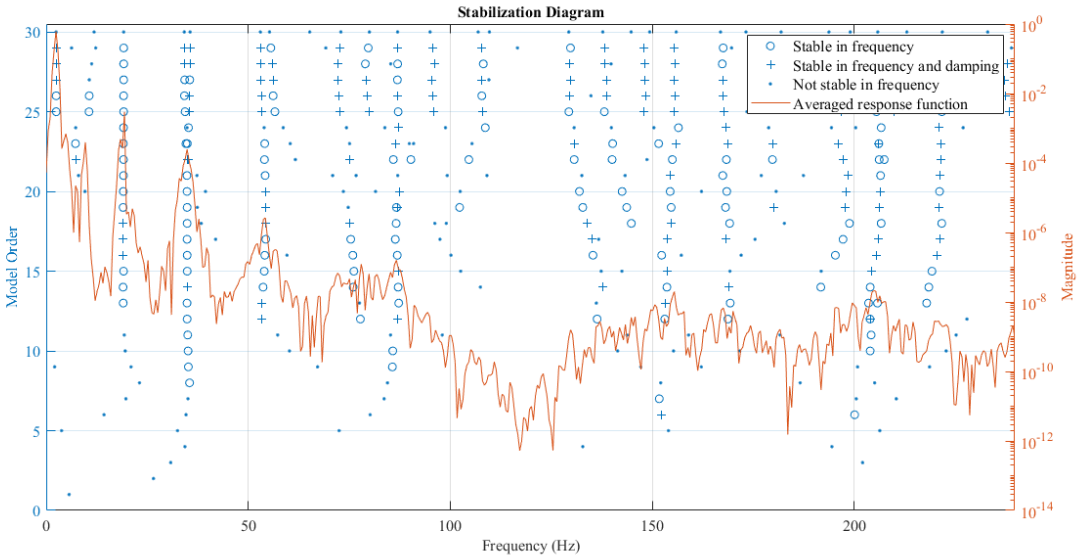

Figure A.6: MOCAP-based stability diagrams from FRF analysis.

(a) Bonafide

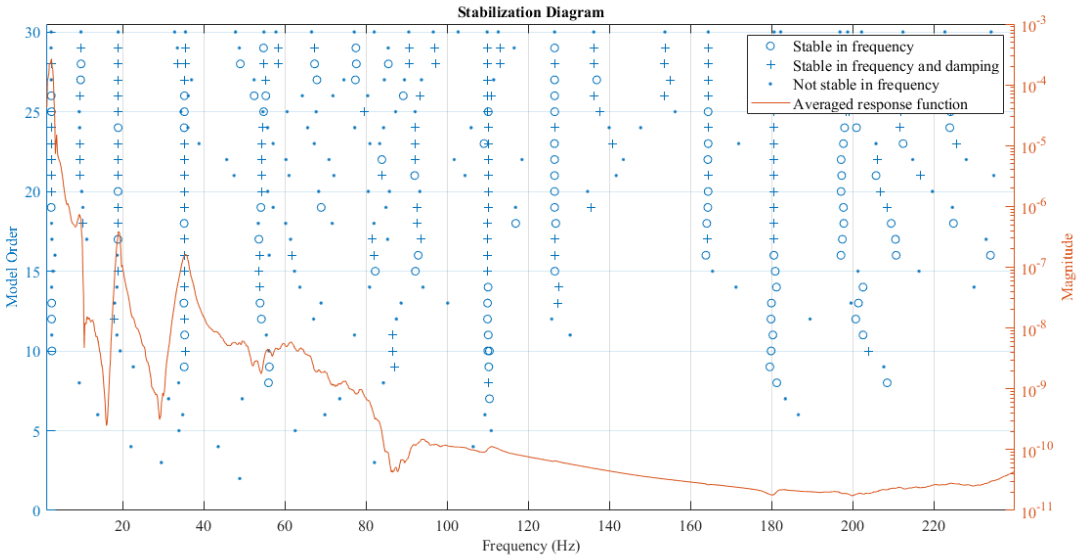

(b) Rustler

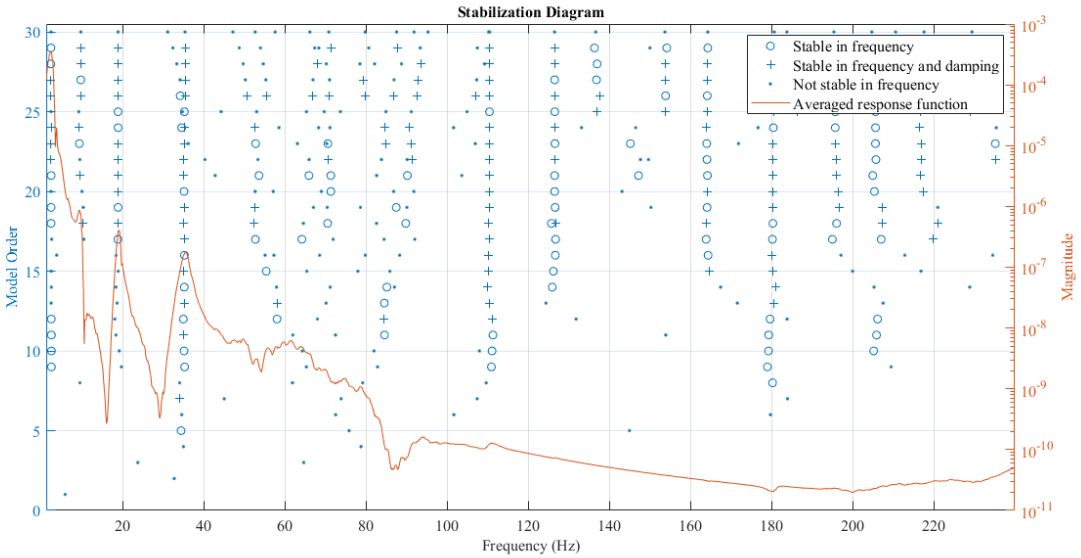

Figure A.7: MOCAP-based stability diagrams from torsional FRF analysis.

(a) Bonafide

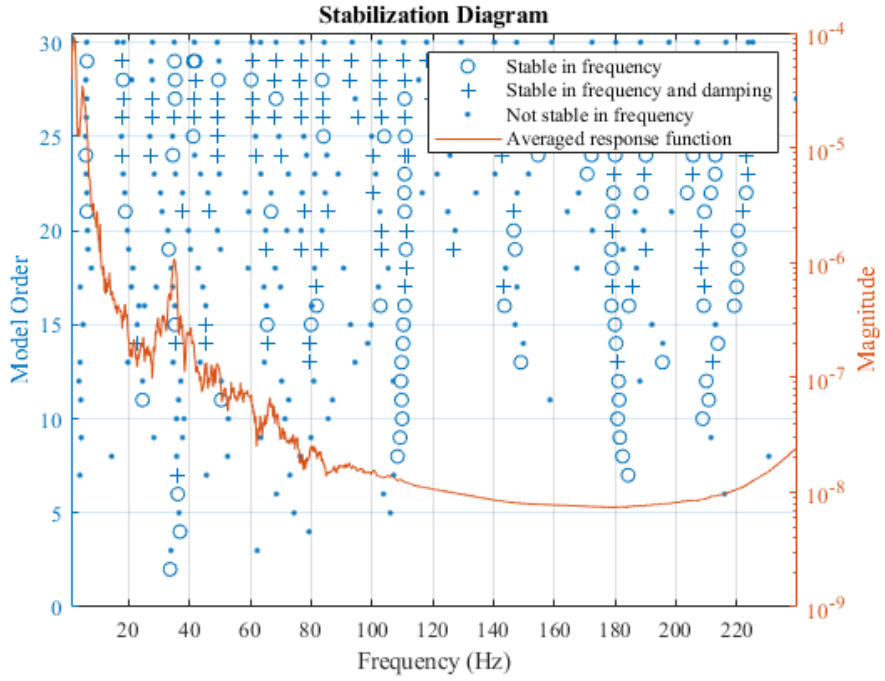

(b) Rustler

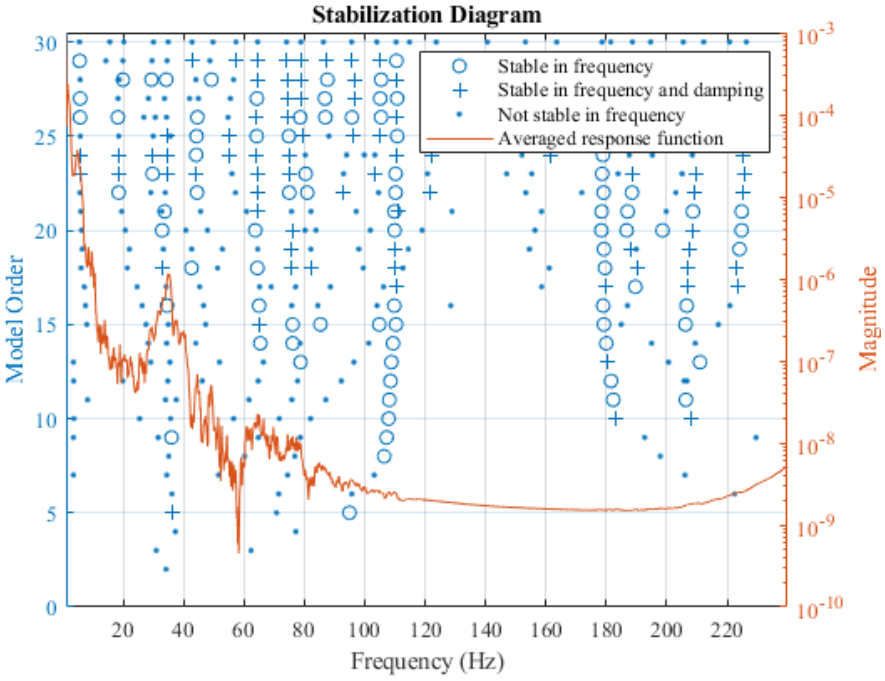

Figure A.8: Results from acceleration-based FRF analysis on the Bonafide, the plots show the real components of the FRFs. X: Frequency (Hz), Y: Distance Relative to Boot Center (cm), Z: Magnitude (dB)

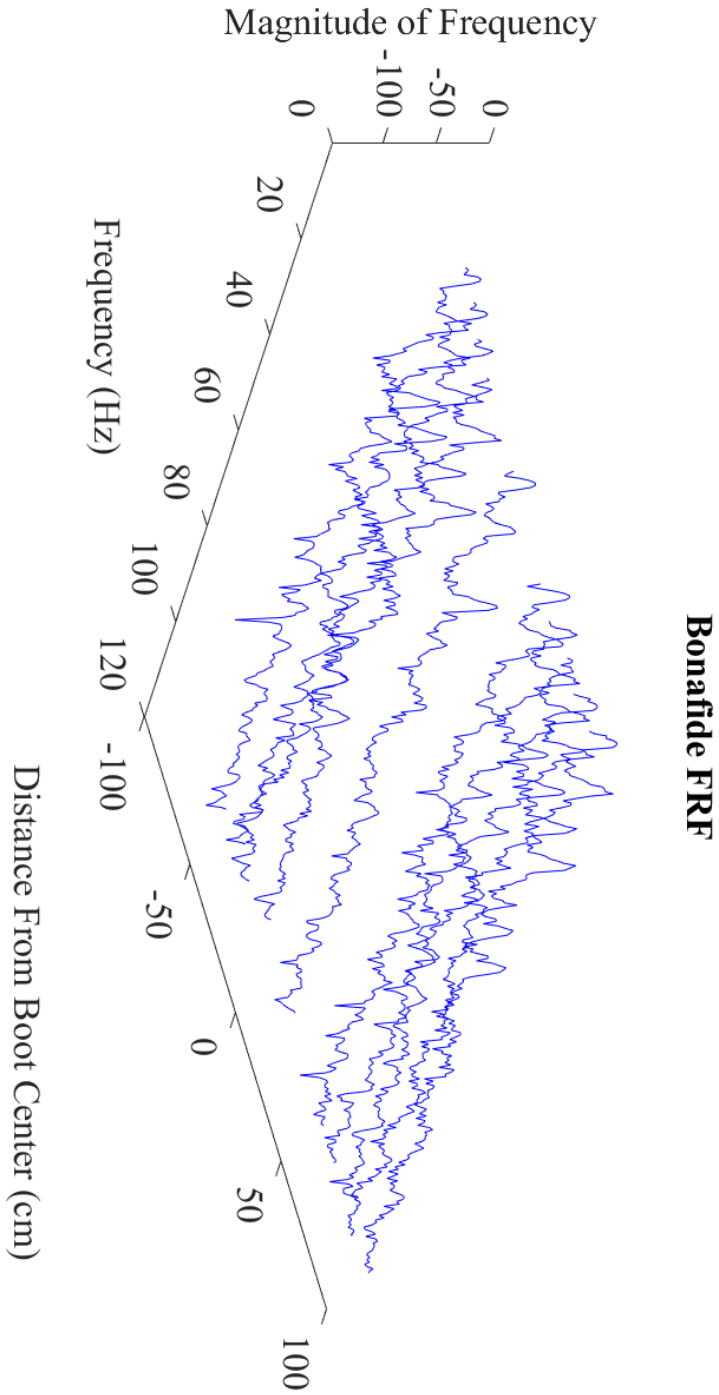

Figure A.9: Results from acceleration-based FRF analysis on the Rustler, the plots show the real components of the FRFs. X: Frequency (Hz), Y: Distance Relative to Boot Center (cm), Z: Magnitude (dB)

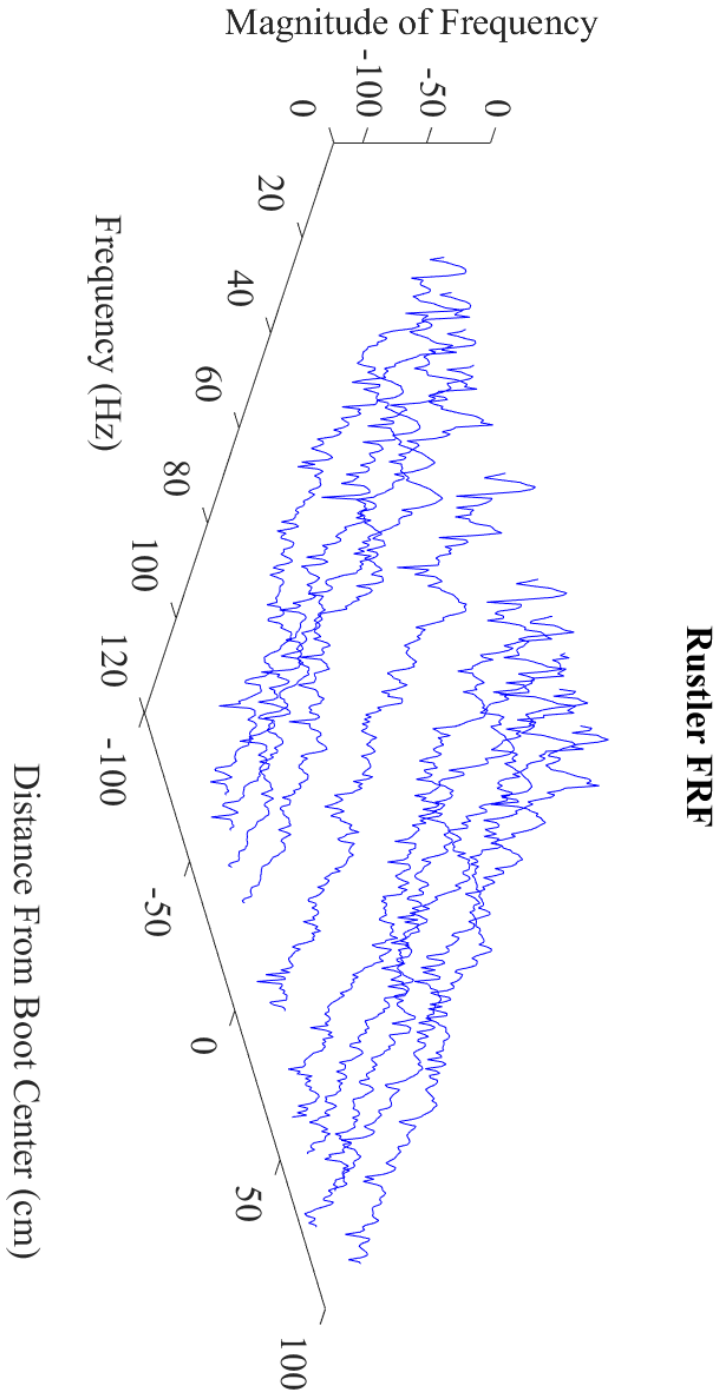

Figure A.10: Results from acceleration-based FRF analysis on the Bonafide, the plots show the real components of the FRFs. X: Frequency (Hz), Y: Distance Relative to Boot Center (cm), Z: Real

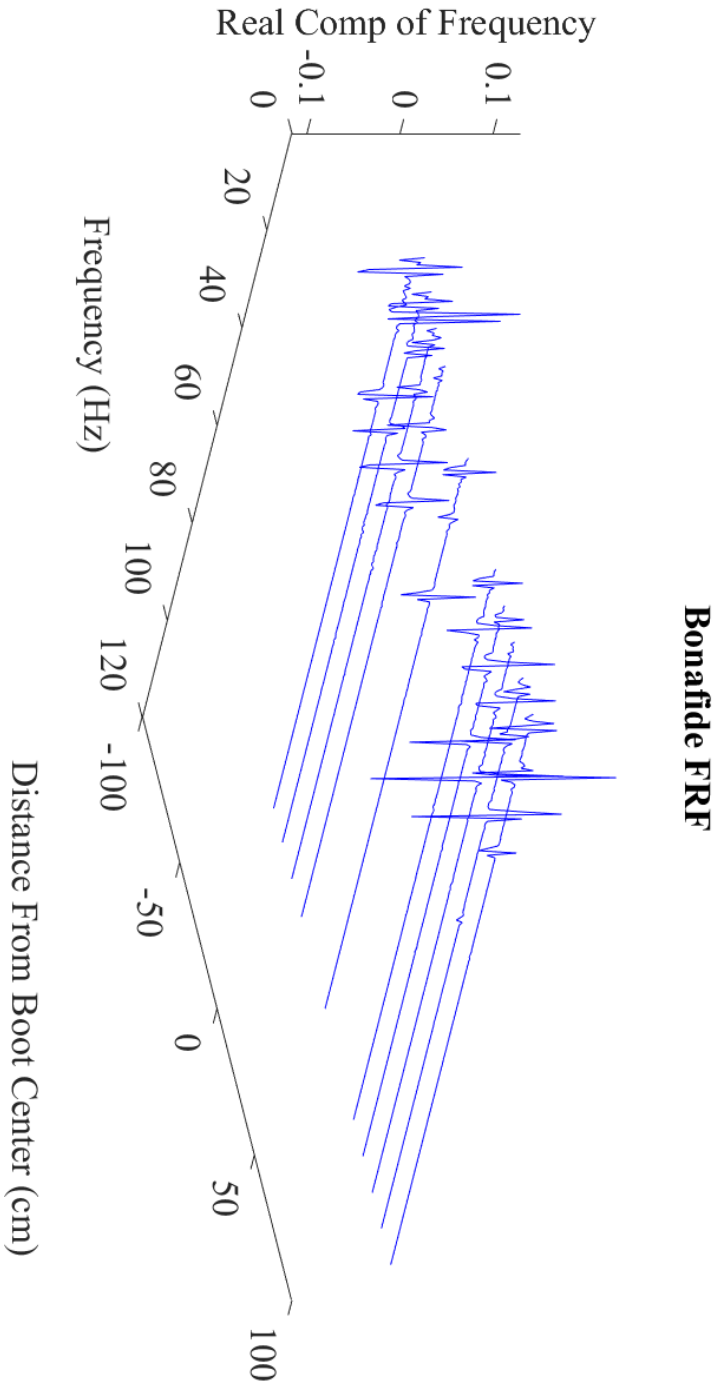

Figure A.11: Results from acceleration-based FRF analysis on the Rustler, the plots show the real components of the FRFs. X: Frequency (Hz), Y: Distance Relative to Boot Center (cm), Z: Real

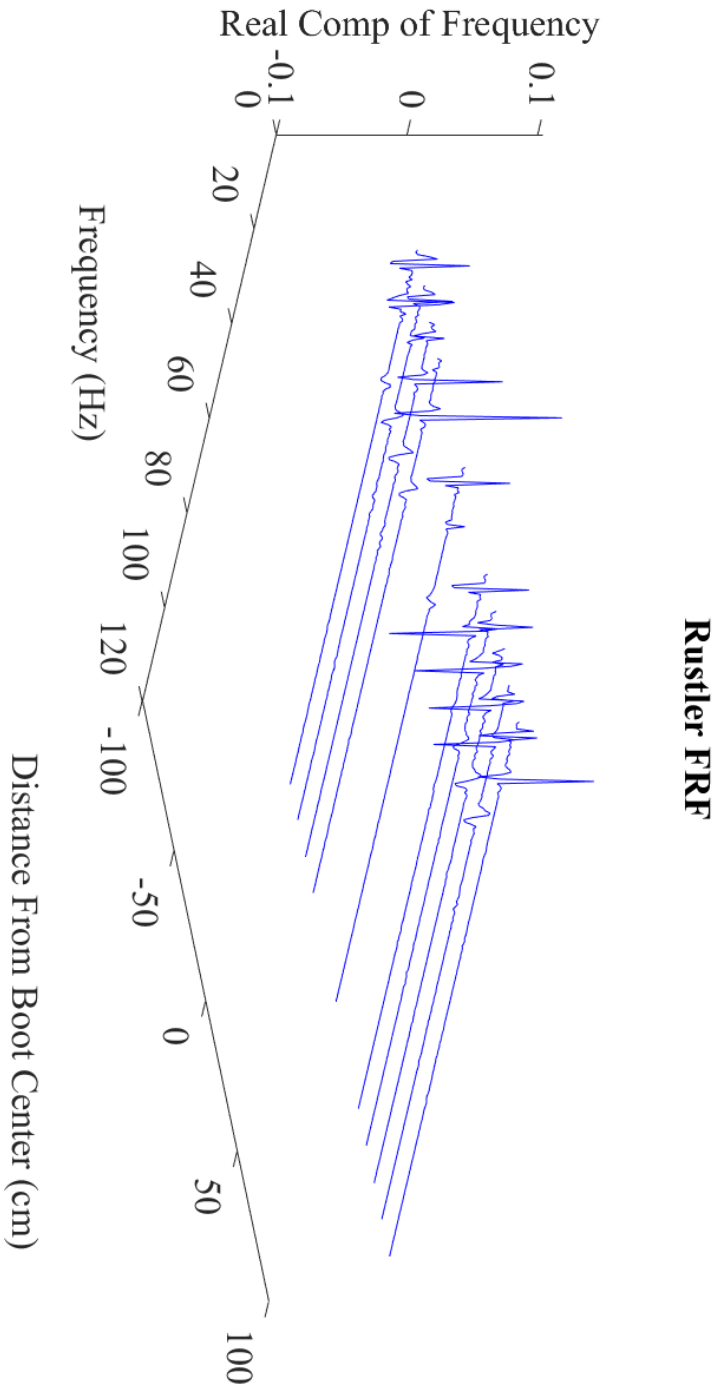

Figure A.12: Results from acceleration-based FRF analysis on the Bonafide, the plots show the real components of the FRFs. X: Frequency (Hz), Y: Distance Relative to Boot Center (cm), Z: Real

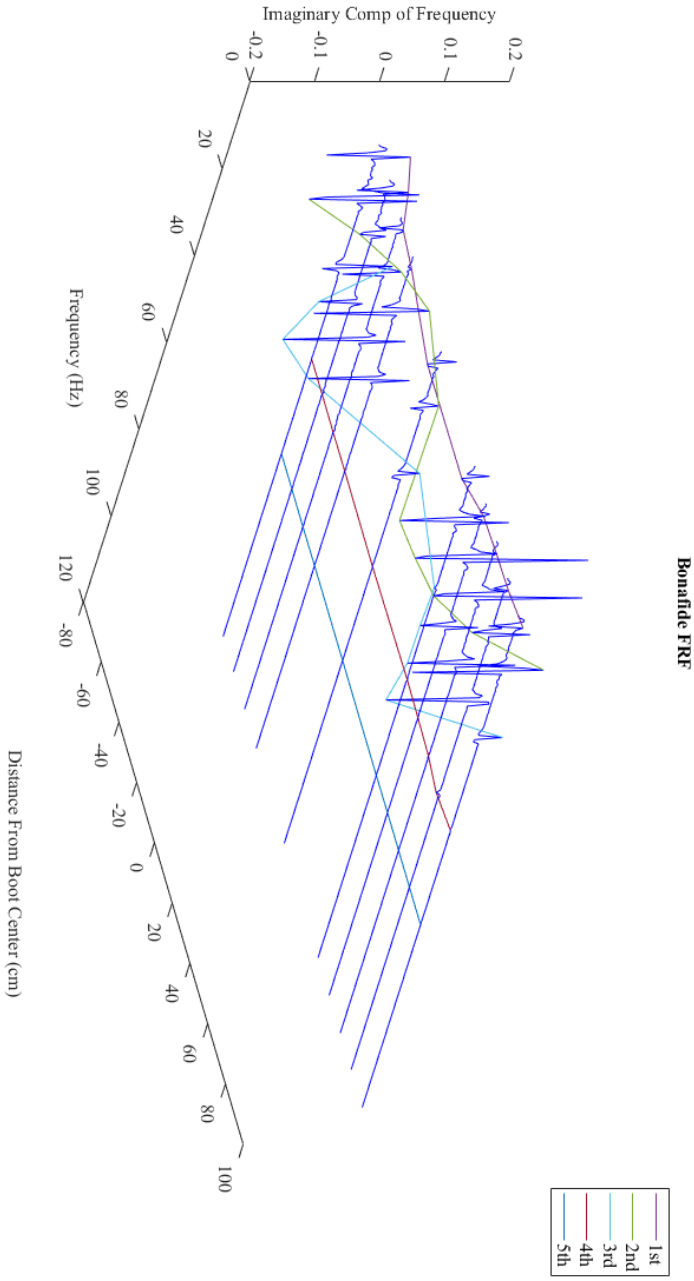

Figure A.13: Results from acceleration-based FRF analysis on the Rustler, the plots show the real components of the FRFs. X: Frequency (Hz), Y: Distance Relative to Boot Center (cm), Z: Real

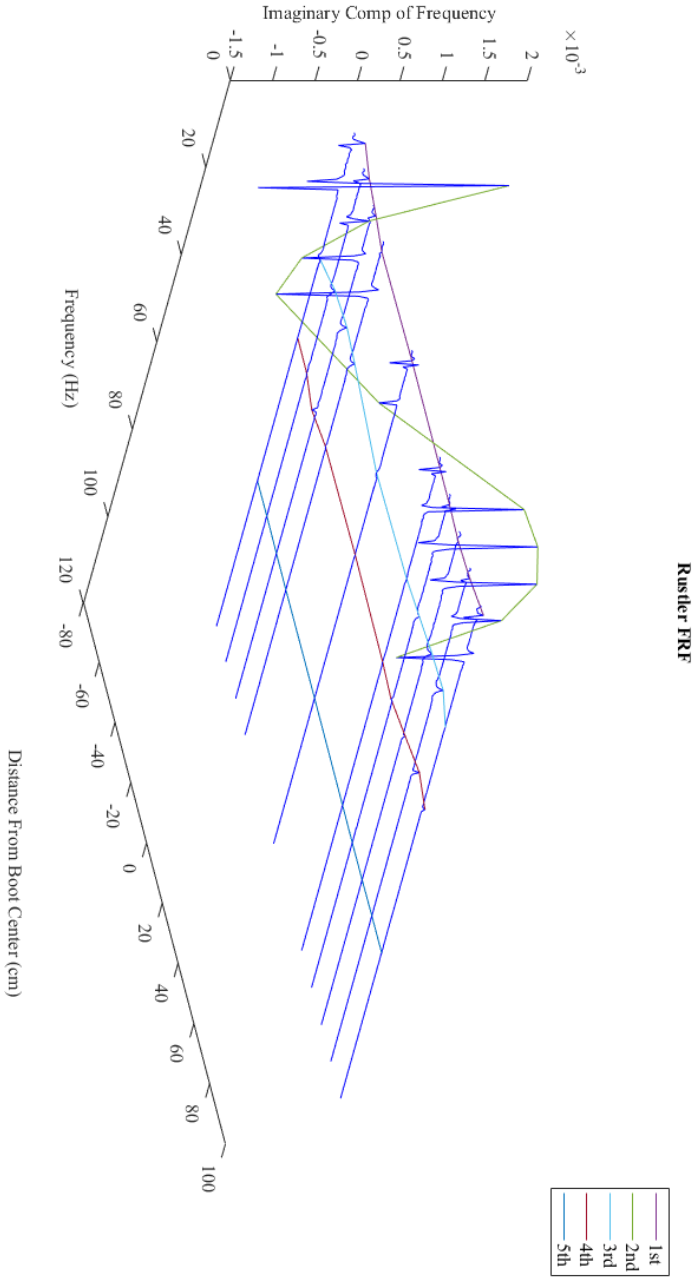

Figure A.14: Results from displacement-based FRF analysis on the Bonafide, the plots show the real components of the FRFs. X: Frequency (Hz), Y: Distance Relative to Boot Center (cm), Z: Real

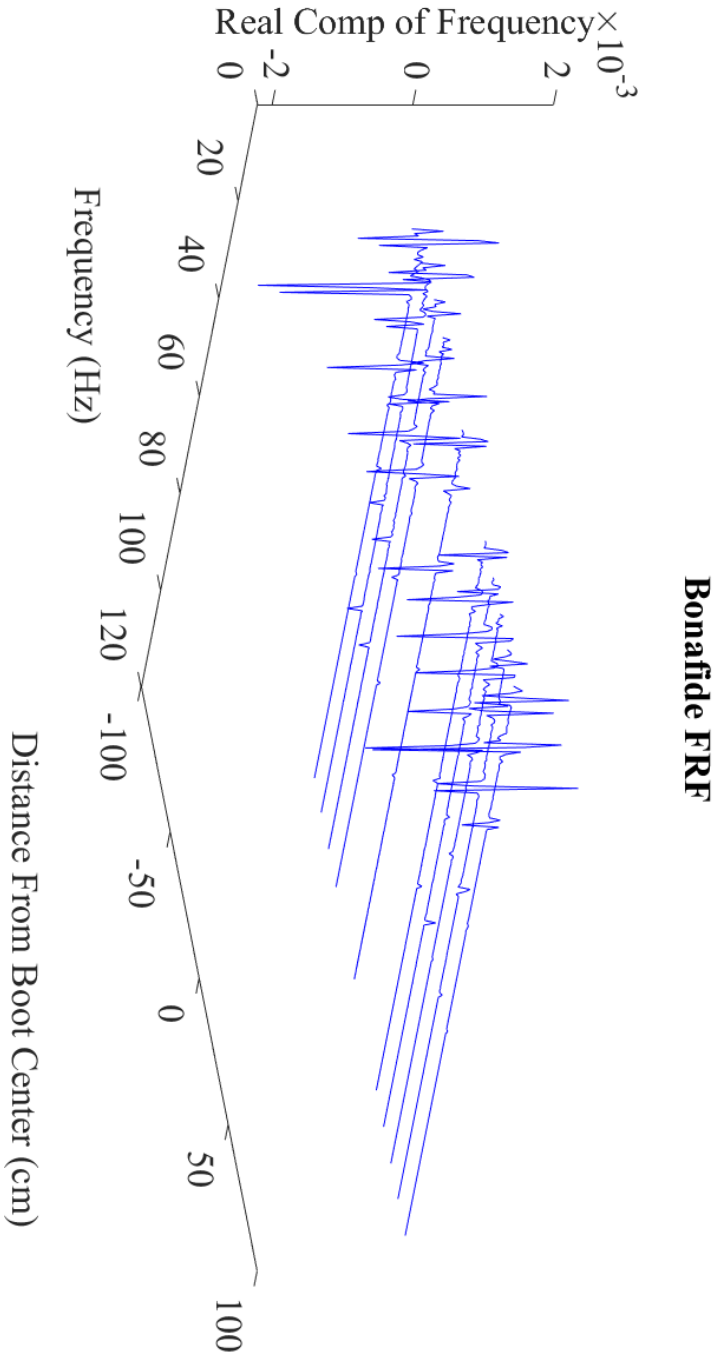

Figure A.15: Results from displacement-based FRF analysis on the Rustler, the plots show the real components of the FRFs. X: Frequency (Hz), Y: Distance Relative to Boot Center (cm), Z: Real

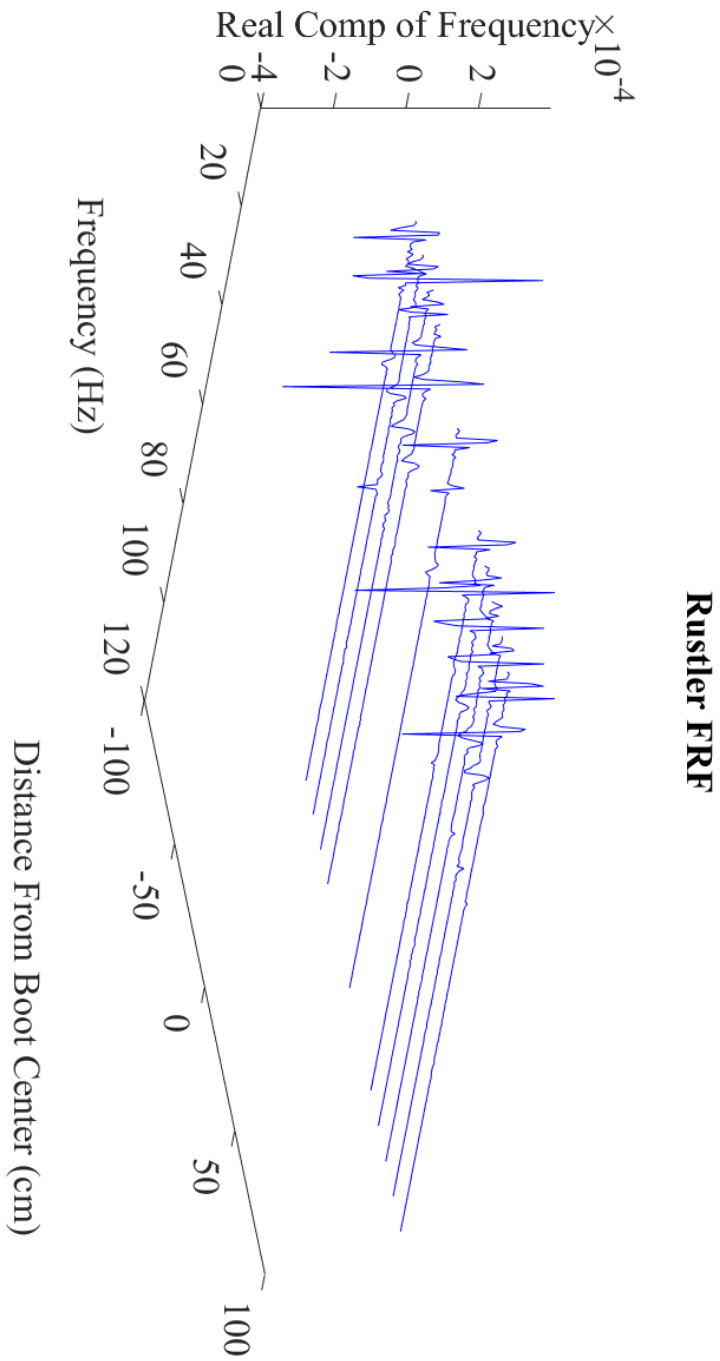

Figure A.16: Results from displacement-based FRF analysis on the Bonafide, the plots show the real components of the FRFs. X: Frequency (Hz), Y: Distance Relative to Boot Center (cm), Z: Magnitude (dB)

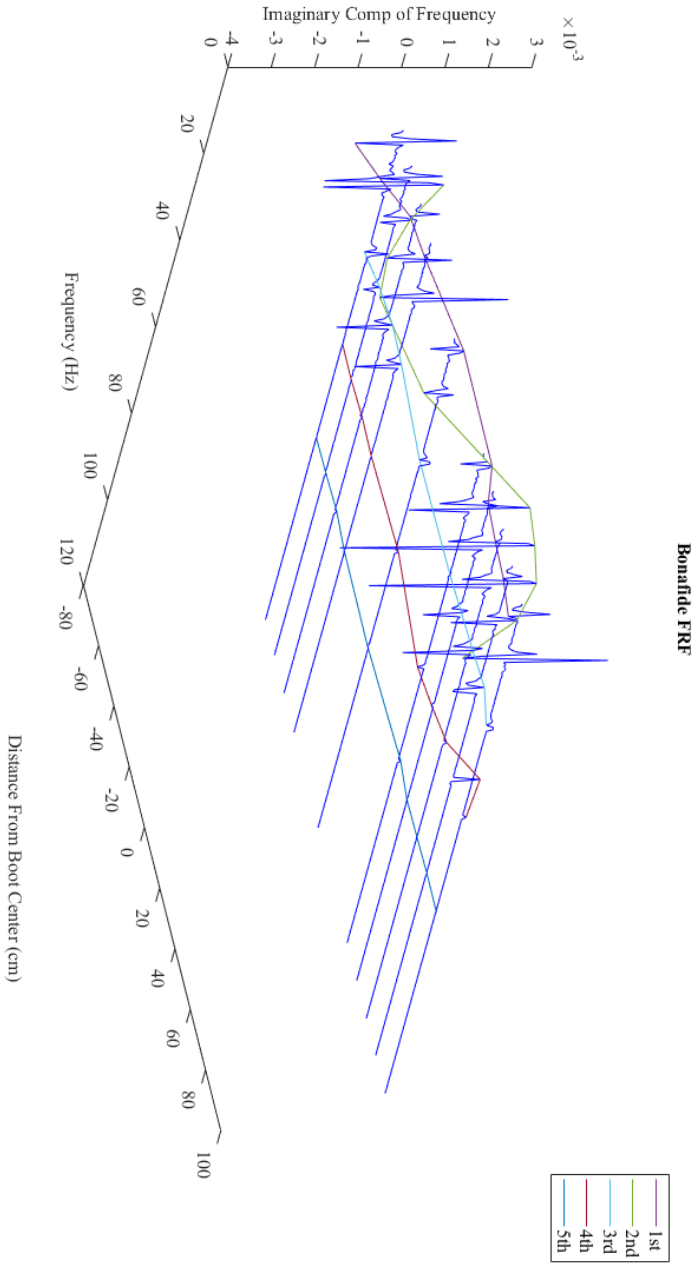

Figure A.17: Results from displacement-based FRF analysis on the Rustler, the plots show the real components of the FRFs. X: Frequency (Hz), Y: Distance Relative to Boot Center (cm), Z: Magnitude (dB)

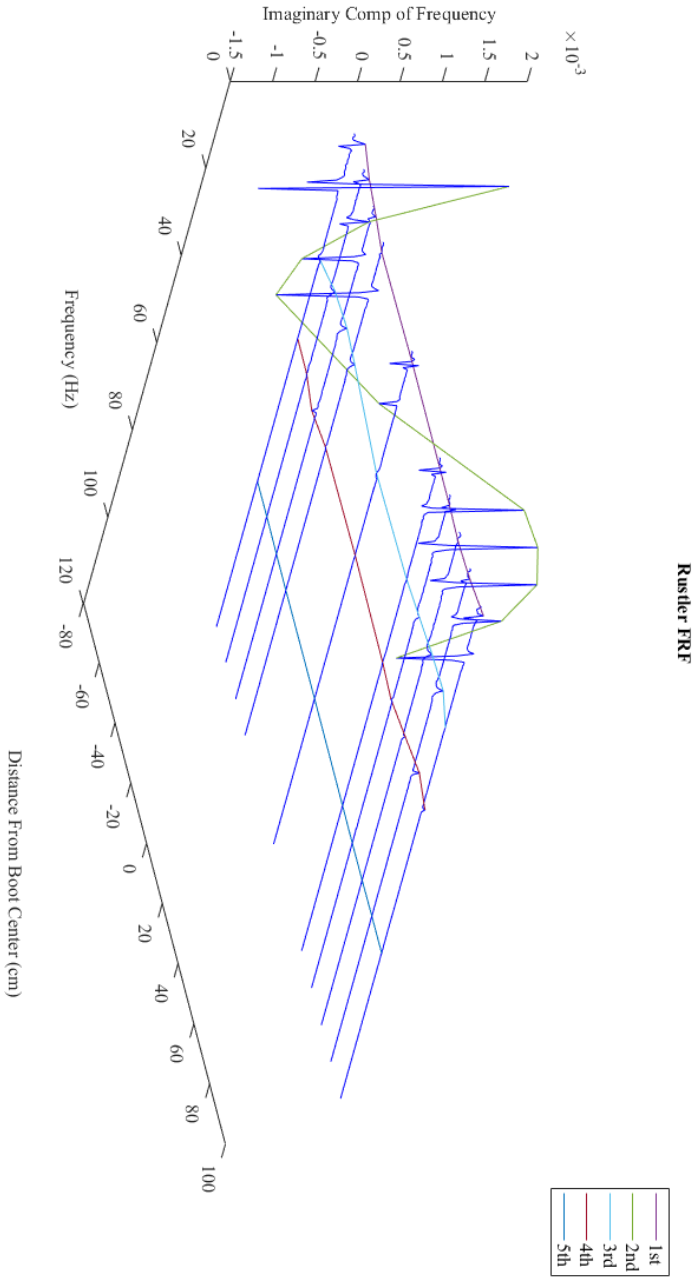

Figure A.18: Normalized imaginary components for easier visual analysis. X: Distance Relative to Boot Center (cm), Y: Distance Relative to Center Cord (cm), Z: Unity Modal Mass

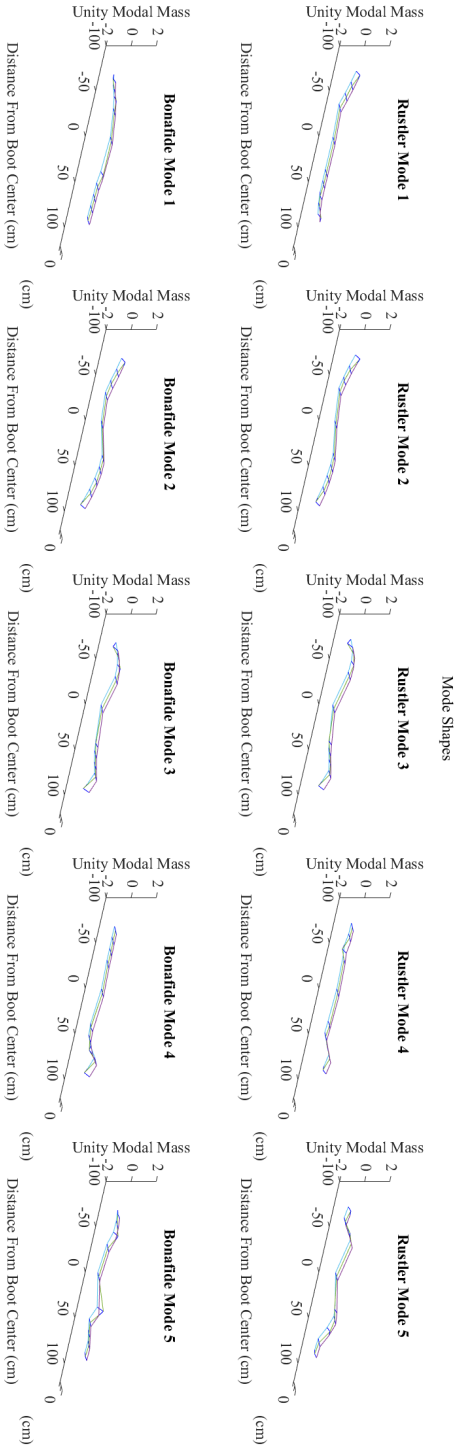

Figure A.19: Bending mode shape derived from the imaginary components of accelerometer-based FRF analysis. Contains a polynomial fit for visual correlation against Figure.3.7. Imaginary Component vs. Distance Relative to Boot Center (cm)

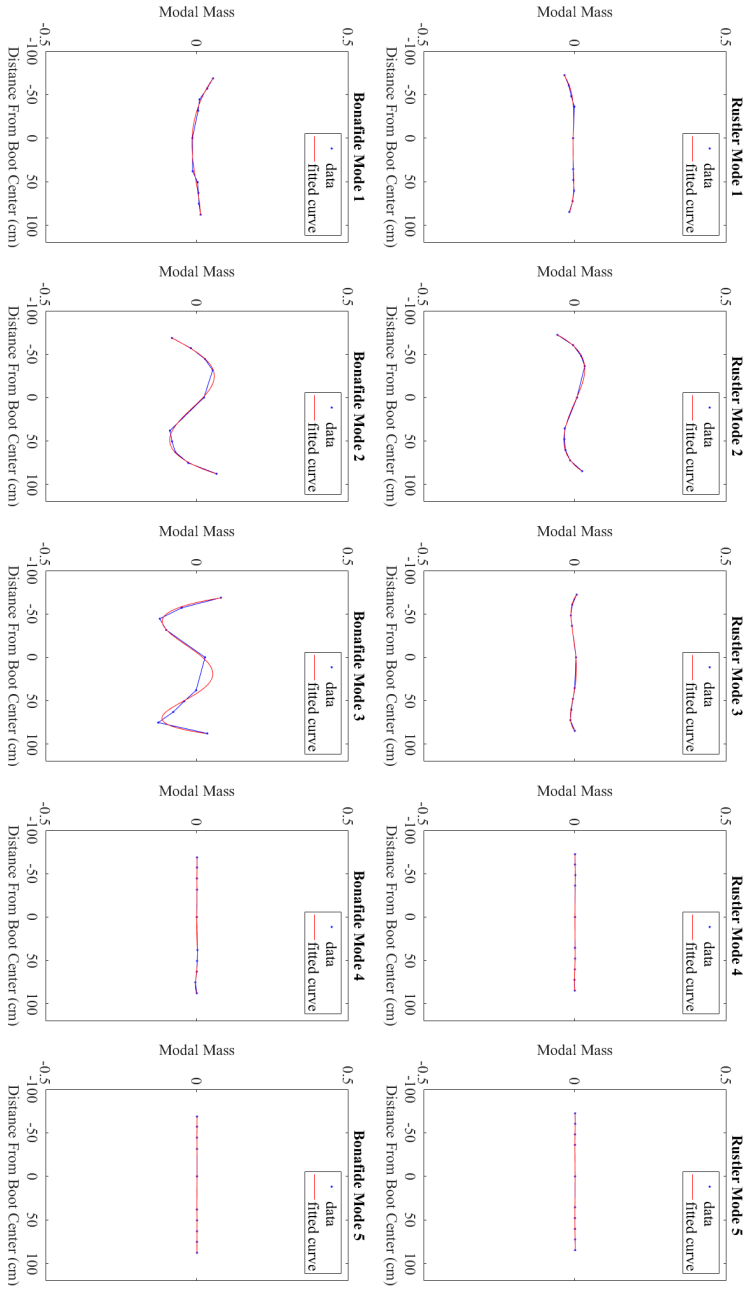

Figure A.20: Bending mode shape derived from the imaginary components of displacement-based FRF analysis. Imaginary Component vs. Distance Relative to Boot Center (cm)

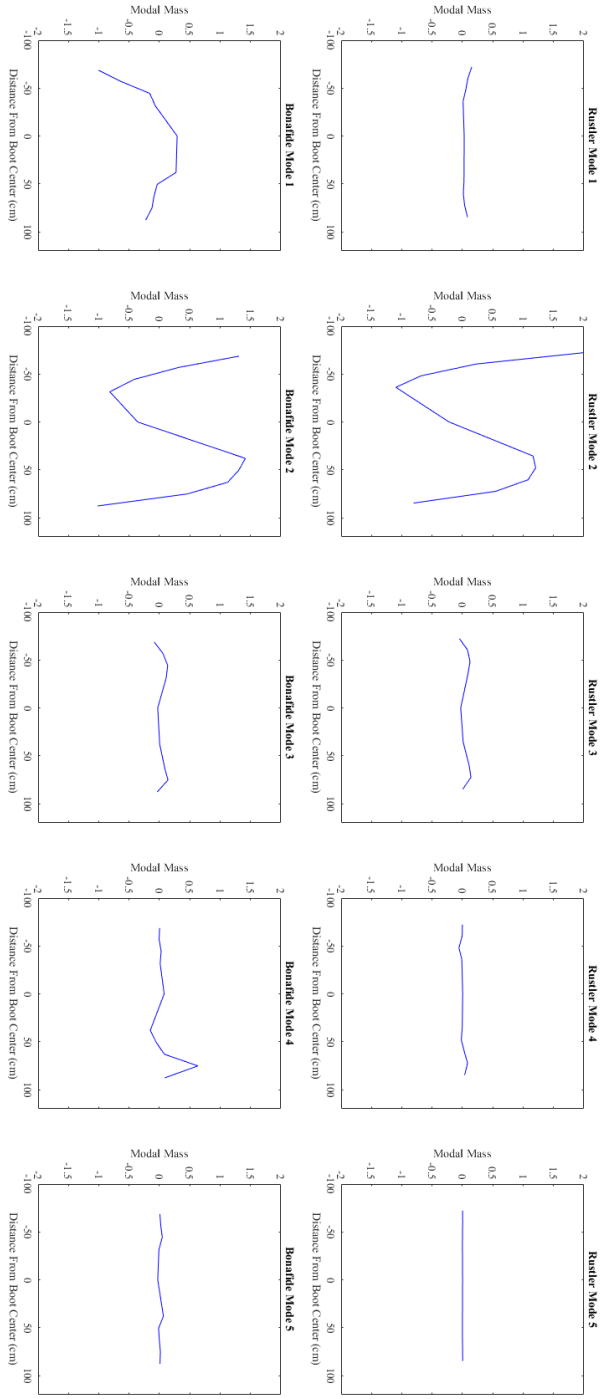

Figure A.21: Bending stiffness profiles; Red: Bonafide, Blue: Rustler. Stiffness (Nm^2) vs. Position Relative to Boot Center (m)

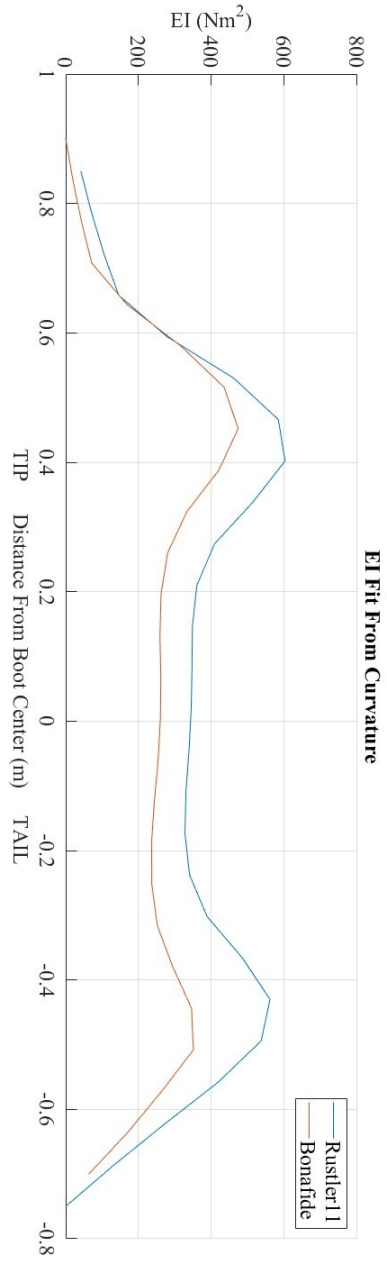

Figure A.22: Torsional stiffness profiles; Red: Bonafide, Blue: Rustler. Stiffness (Nm^2) vs. Position Relative to Boot Center (m)